Wireless and Untethered Electrochemical Oxygen Sensor for Respiratory Gas Exchange Analysis

A THESIS

SUBMITTED TO THE FACULTY OF THE GRADUATE SCHOOL

OF THE UNIVERSITY OF MINNESOTA

BY

Matthew Stephen Hildebrand

IN PARTIAL FULFILLMENT OF THE REQUIREMENTS

FOR THE DEGREE OF

MASTER OF SCIENCE

Adviser: Dr. Rajesh Rajamani

November 2011

Acknowledgements

First, I want to thank Professor Rajamani for making this work possible. From the onset I found myself inspired by his generosity, knowledge and faith. But ultimately, it was his patience, guidance and support that made this work possible. ‘Patience’ should really be in bold, capital letters. I feel very fortunate to have been a member of Rajamani’s research lab. I could not choose someone I would rather work for.

I was fortunate to find wonderful friends and colleagues in all of my lab-mates. In particular, I want to thank Shyam Sivaramakrishnan for his support during the early stages of the project. While our work overlapped only for a short time, his help and guidance got me started on the right foot.

I am also very grateful for the invaluable support and ingenuity provided by Lee Alexander. His manufacturing, design and wireless programming skills were second to none and essential to our success.

I have made so many wonderful friends since moving to the twin cities, but a few from back home deserve extra thanks. I am not sure what I would have done without Kent Thomson’s generosity and friendship. I also want to thank Andrew Sander and his wife Leslie for their amazing friendship and support. Besides being flawlessly practical and bighearted, Andrew has been on my side of post-secondary education since day one.

Finally, I want to thank my family. To my parents and my brothers for their unwavering support, thank you so much.

Dedication

To my parents, Anne and Jerry

Abstract

The objective of this work is to create a novel medical sensor for monitoring the concentration of oxygen in exhaled human breath. The ultimate goal is to combine this work with a contiguous research project to deliver a sensor that measures several breath constituents, including CO_2, and end-tidal volume. Current respiratory monitoring systems suffer from limitations including high cost and power consumption, large size and usually require breath to be drawn through sampling tubes. These factors lead to a lack of portability in current monitoring systems. Further motivation for a portable oxygen sensor is the importance of oxygen as a breath marker for prognostics and ambulatory monitoring.

Electrochemical sensing techniques are chosen for the oxygen sensor due to their relatively low cost, small size and high selectivity. The design process combines several other disciplines including nanofabrication, electrical engineering and mechanical engineering. Nafion 117 membrane is chosen from the onset as the solid polymer electrolyte (SPE) for the sensor. Early work explored a variety of platinum electrodes including the use of carbon nanotubes (CNT) to increase surface area. Apart from the challenges of fabricating with carbon nanotubes, no significant advantages could be obtained with the CNT-based electrodes.

Instead, a SPE-based oxygen sensor is developed using the membrane electrode assemblies commonly found in proton exchange membrane (PEM) fuel cells. A Teflon coating allows the sensor to function under the influence of varying humidity. The sensor implements two porous electrodes rather than the typical 3-electrode sensor cell and therefore does not require a potentiostat circuit to operate.

Early embodiments are replaced with a small, open channel sensor design. The small, portable sensor is powered by two 3-volt lithium coin batteries and transmits the signal wirelessly to a USB receiver on a laptop. Unlike similarly sized commercial sensors, the developed sensor does not require a pneumatic sampling system. It is thus a compact untethered sensor very suitable for ambulatory applications. The raw signal is post-

processed using special signal processing algorithms. The total material cost of the sensor (including wireless components) is roughly $200.

The sensor is tested at the University of Minnesota using a MedGraphics Cardiopulmonary Exercise System (CPX) and against a mass spectrometer (MS) at St. Mary's Hospital in Rochester MN. The final test is conducted on February 10th, 2011 during which 20 data sets are obtained for various breathing patterns. Post processing techniques include algorithms for breath-detection, slope-correction, baseline-correction, model inversion and calibration. The low frequency drift is removed and end tidal oxygen concentration is measured with an RMS error of 0.2 $\%O_2$ over steady, resting-rate respiration (max error less than ± 0.75 $\%O_2$). During faster respiration (such as exercise) or largely-varying respiration, the end tidal accuracy of the sensor deteriorates to an error of ± 1 $\%O_2$ (max error less than ± 4 $\%O_2$).

A new configuration of the sensor is developed with an on-board fan. The fan speeds up the sensor response and is also able to provide a rotational speed signal from which breath flow rate through the sensor can be computed. Even with the on-board fan, the sensor can continue to be wireless and untethered.

The data shows that the improved speed of the sensor provides more accurate O_2 concentration measurement and a closer match with the mass spectrometer. However, the calibration gains needed for the sensor vary with the breathing flow rate. An algorithm that calibrates sensor response using flow rate measurements is found to yield consistent performance over a variety of breathing patterns and varying flow rates. With the fan flow sensor in place, the sensor error decreased to ± 0.35 $\%O_2$ (± 1.2 $\%O_2$ maximum) for erratic breathing patterns, including widely-varying flow rates. The fan flow meter also enables the oxygen sensor to measure volume of flow which is useful for many clinical diagnostic applications.

Table of Contents

Acknowledgements i

Abstract iii

List of Tables viii

List of Figures ix

Chapter 1. Introduction 1

1.1 Review of Current Respiratory Gas Analysis 01

1.2 Limitations of Current Human Breath Monitoring Technology 03

1.3 Need for New Technology 05

Chapter 2. Electrochemical Oxygen Sensors 7

2.1 Background 07

2.2 Early Solid-Polymer Electrolyte Sensors 09

2.3 Overview of PEMFC Technology 11

2.3.1 Current Technology 11

2.3.2 The Reduction-Oxidation Reaction 12

2.3.3 New Technology and CNT-Based Electrodes 13

2.4 The Oxygen Sensing Mechanism 14

2.4.1 The Reverse Reduction-Oxidation Reaction 14

2.4.2 The Triple Phase Boundary 16

2.5 Electrochemical Oxygen Sensor Components 16

2.5.1 The Membrane Electrode Assembly 16

2.5.2 The Proton Exchange Membrane (Nafion) 17

2.5.3 The Catalyst and Gas Diffusion Layers 19

2.5.4 Hot-Pressing the MEA 20

Chapter 3. Early Embodiments 22

3.1 Introduction 22

3.2 Sensor Fabrication 24

3.2.1 Sputter Deposition Electrode Fabrication 24

3.2.2 CNT-Based Electrode Fabrication 27

3.3 Experimental Setup 28

3.3.1 Gas Handling Setup 28

3.3.2 Control and Measurement Circuits 29

3.4 Results and Discussion 31

3.4.1 CNT/Pt/Nafion Composite Sensor 31

3.4.2 Three-Electrode Sensor 33

3.4.3 Two-Electrode Sensor 35

3.4.4 Support Casing 38

3.4.5 Relative Humidity and the Response to Expired Oxygen 40

3.5 Conclusions 42

Chapter 4. PEMFC-Based Oxygen Sensor (1st Generation) 43

4.1 Sensor Fabrication 43

4.2 Results and Discussion 47

4.2.1 Sensitivity to Dry Gas and Changing Relative Humidity 47

4.2.2 Sensitivity to Respired Breath 49

4.3 Conclusions 53

Chapter 5. Digital Signal (Post) Processing 54

5.1 Introduction 54

5.2 Low Frequency Drift Correction 55

5.2.1 Constant Background Assumption 55

5.2.2 Attenuating High Frequency Noise 56

5.2.3 Breath Detection Algorithm 58

5.2.4 Slope Correction Algorithm 60

5.2.5 Drift Correction Example *64*
5.3 Measuring Sensor Performance (Response Time and Accuracy) 65
5.4 Improving Sensor Response Time 66
5.4.1 Baseline Correction *66*
5.4.2 Model Inversion *68*
5.5 Conclusions 71

Chapter 6. PEMFC-Based Oxygen Sensor (2nd Generation) 72

6.1 Motivation for a New Design 72
6.2 Wireless, Untethered, Open-Channel Sensor 73
6.2.1 Open-Channel Design *73*
6.2.2 Wireless Design *76*
6.3 Results and Discussion 79
6.4 Flow Sensitivity and Flow Sensing 84
6.4.1 Flow Rate Dependence *84*
6.4.2 Flow Correction Algorithm *87*
6.5 Conclusions 90

Chapter 7. Conclusions 91

7.1 Conclusions 91
7.2 Future Work 93

References 94

Appendix 100

List of Tables

Table 1.1. Breath markers in certain diseases or applications 03

List of Figures

Chapter 1. Introduction 1

Figure 1.1 Mass spectrometer in medical setting 04

Figure 1.2 Pneumatic sampling system 04

Figure 1.3 Early concepts and preferred embodiments 06

Chapter 2. Electrochemical Oxygen Sensors 7

Figure 2.1 Clarke-type electrode 07

Figure 2.2 Simplified circuit of electrochemical cell 08

Figure 2.3 Conventional potentiostatic system 08

Figure 2.4 Configuration of early SPE oxygen sensor 09

Figure 2.5 Exploded view of PEMFC stack 12

Figure 2.6 Block diagram of fuel cell 13

Figure 2.7 SPE-based electrochemical sensor 15

Figure 2.8 Triple phase boundary 16

Figure 2.9 The membrane electrode assembly 17

Figure 2.10 Nafion membrane example 18

Figure 2.11 The chemical structure of Nafion 18

Chapter 3. Early Embodiments 22

Figure 3.1 Fuel cell performance verses platinum thickness 23

Figure 3.2 Sputtering process 25

Figure 3.3 Schematic of sputtered MEA assemblies 26

Figure 3.4 Photographs of MEAs with sputtered Pt electrodes 26

Figure 3.5 Schematic for synthesis of Pt/CNT catalysts 27

Figure 3.6 Schematic of gas handling setup 28

Figure 3.7 Schematic of 3-electrode potentiostat measurement and control circuit 29

Figure 3.8 Two-electrode equivalent circuit 30

Figure 3.9 Two-electrode measurement circuit 30

Figure 3.10 Test result from composite sensor 32

Figure 3.11 Test result from 3-electrode sensor 34
Figure 3.12 Test result from 2-electrode sensor 36
Figure 3.13 Casing for sputter-fabricated sensor 39
Figure 3.14 Test result of sensitivity to humidity 40
Figure 3.15 Sensor response to expired breaths 41

Chapter 4. PEMFC-Based Oxygen Sensor (1st Generation) 43

Figure 4.1 Model of 1st-generation oxygen sensor 45
Figure 4.2 Photographs of 1st-generation oxygen sensor 46
Figure 4.3 Sensor response to oxygen 47
Figure 4.4 Sensor response to expired oxygen in human breath (data set 1) 50
Figure 4.5 Sensor response to expired oxygen in human breath (data set 2) 51

Chapter 5. Digital Signal (Post) Processing 54

Figure 5.1 Sinusoidal model of respiration 56
Figure 5.2 Example of typical signal noise 57
Figure 5.3 The measured sensor signal after lowpass filtering 58
Figure 5.4 Output from the breath detection algorithm 59
Figure 5.5 Illustration of slope correction algorithm 61
Figure 5.6 Sensor signal before and after drift correction 63
Figure 5.7 Drift corrected signal for sinusoidal respiration model. 64
Figure 5.8 Breath detection and slope correction algorithm results 65
Figure 5.9 Test data illustrating the baseline correction algorithm 67
Figure 5.10 Oxygen sensor modeled as a first order linear system 69
Figure 5.11 Test data implementing the model inversion technique 70

Chapter 6. PEMFC-Based Oxygen Sensor (2nd Generation) 72

Figure 6.1 Teledyne UFO-130 Ultra-Fast Oxygen Sensor 72
Figure 6.2 Open-channel sensor design 74
Figure 6.3 Second-generation sensing circuit 75
Figure 6.4 The eZ430-RF2500 wireless development tool kit 76
Figure 6.5 Electronic and wireless components 77

Figure 6.6 Second-generation oxygen sensor 78
Figure 6.7 Oxygen sensor versus mass spectrometer 80
Figure 6.8 Raw data and output from breath detection algorithm 81
Figure 6.9 Raw sensor data versus post-processed data 82
Figure 6.10 Test result with mass spectrometer 83
Figure 6.11 Sunon MagLev CPU cooling fan 84
Figure 6.12 Flow rate from fan-flow meter versus Mayo flow meter 86
Figure 6.13 Output from fan-flow meter and flow-correction algorithm 88
Figure 6.14 Test result with mass spectrometer and flow-correction algorithm 89

CHAPTER 1 INTRODUCTION

1.1 Review of Current Respiratory Gas Analysis

Respiratory gas analysis has become a critical part of clinical diagnostic testing and monitoring [1, 2, 3, 4]. It is used in intensive care settings, anesthesia, quantification of cardiac output, sleep diagnostic monitoring, clinical exercise testing, nutrition labs, and in many other important settings.

For intensive care settings and anesthesia, careful monitoring of respiratory gases is the current standard of care [5]. Once anesthetized, a patient's respiration can be depressed due to the anesthesetic agents or additional drugs (namely opioids) administered to control pain. A rise in CO_2 concentration (hypercapnia) and a corresponding drop in the arterial O_2 concentration (hypoxaemia) may result [6]. As a result, breath analyses which monitor the concentrations of exhaled carbon dioxide and oxygen are used in anesthesia [7, 8, 9]. Similarly, respiratory activity may be affected during diagnostic procedures such as MR imaging in which patients are sedated. Breath analysis is sometimes used during these examinations [10].

Respiratory gas analysis can also be integrated with measures of breathing pattern (e.g., tidal volume, respiratory rate) and ventilation to obtain amounts of oxygen consumption (VO_2) and carbon dioxide production (VCO_2). These consumption and production measures provide powerful prognostic information for a number of diseases [11].

For the quantification of cardiac output, the gold standard is the direct Fick method in which the cardiac output is calculated as the quotient of oxygen uptake (VO2) and the difference of the arterial and mixed venous oxygen content. While effective, the direct Fick technique is only rarely used in clinical practice because the bedside measurement of oxygen uptake is technically demanding [12].

In the cases of hypo ventilation and hyper ventilation, in order to monitor hypercapnia (excess carbon dioxide in blood) and hypoxaemia (deprivation of oxygen in blood)

breath analysis requires measurement of concentration of oxygen and/or carbon dioxide [13, 14].

Measuring exhaled carbon dioxide has also been used to confirm the correct placement of an endotracheal tube in the trachea, saving many lives as a result [13]. Several other applications such as monitoring patient breathing during treatment of cardiac arrest, asthma, dyspnea, pediatric trauma and others have also been reported [14].

Breath monitoring (the occurrence of regular breathing) plays a vital role in many applications including treatment of sleep apnea [15] and prevention of sudden infant death syndrome (SIDS). These are both diseases in which an interruption of breathing can be fatal or have severe consequences. Children who are born prematurely require continuous breathing surveillance for several weeks to decide if or when assisted mechanical ventilation is needed [16].

In the future, breath analysis may play a valuable role in identifying the presence of many other diseases or provide an ability to monitor therapeutic progress of the patient. Table 1.1 lists some major diseases and the corresponding breath markers that serve as disease indicators [17]. Techniques to measure these breath markers, however, remain to be developed.

Table 1.1: Breath markers in certain diseases or applications

	Disease/Application	Breath Marker
Oxidative stress	Lipid peroxidation	*Pentane, ethane*
	Asthma, COPD, bronchiectasis, ARDS	*H_2O_2, BMACa*
Lung diseases	Asthma	*NO, CO, H_2O_2, isoprostanes, nitrite/nitrate*
	COPD	*NO, H_2O_2, eicosanoids (leukotrienes, prostanoids, isoprostanes), isoprostanes*
	Cystic fibrosis	*NO,CO,H_2O_2,isoprostanes,nitrite/nitrate*
	Lung transplant recipient with acute rejection	*Exhaled carbonyl sulfide*
Metablic disorder	Diabetes	*Acetone*
Gastroentric diseases	Disorders of digestion and absorption (lactase deficiency, disorders of di-and monosaccharide malabsorption, starch malabsorption, and small-bowel bacterial overgrowth)	*H_2*
Other Applications	Respiratory monitoring, excretion of drugs	*CO_2/O_2 ratio*

1.2 Limitations of Current Human Breath Monitoring Technology

Current measurement systems for gas analysis include pulse oximeters, infra-red analyzers and mass spectrometers. Pulse oximeters are used for blood oxygen measurement while bedside infra-red analyzers are used for respiratory gas analysis (especially CO_2 measurement) in anesthesiology [18]. The mass spectrometer has always been considered the gold standard for respiratory gas analysis for a number of reasons, including fast response time, ability to measure dry gases, accuracy and stability of measures [11]. In addition, the mass spectrometer has the advantage of measuring multiple gases simultaneously. This system however has fallen out of favor due primarily to cost and size, as well as the need for ongoing preventive maintenance. When cost and space are not an issue, it remains the premier system for respiratory gas analysis.

Figure 1.1: Mass spectrometer in medical setting [19]**.**

Dr. Johnson's laboratory at Mayo Clinic has modified the mass spectrometer to further reduce gas delays and enhance response times. The system is integrated with a number of metabolic measurement systems, including a metabolic cart developed by the Medical Graphics Company (St. Paul, MN). It is calibrated with gravimetric quality gases and serves as an institutional standard to test gas tanks (e.g., respiratory therapy) that arrive without a certification of gas analysis.

Figure 1.2: Pneumatic sampling system.

A major limitation of both bedside infrared analyzers and mass spectrometers is the fact that they are very expensive to acquire and to maintain (mass spectrometers are no longer being manufactured as respired gas monitors [20]). They tend to be bulky units and may require significant amounts of space. They also require a physical connection to the patient for

respiratory gas analysis. This limits their use for respiratory gas analysis as they cannot be used for ambulatory applications or for remote dynamic applications. In addition, infrared analyzers and mass spectrometers require the steady draw of a sample gas over time. This constant sample draw, combined with temperature changes and water vapor pressure results in additional complications in these systems that need to be overcome. For example, special lines or chemicals are often needed to dry the gas prior to analysis. These additional systems can lead to a loss of gas volume (important if gas is being monitored from a closed system such as a rebreathe bag or reservoir) and often cause reduced response times and phase delays. During analysis, signal delays need to be accounted for in algorithms that may require integration of signals to quantify oxygen and carbon dioxide production.

1.3 Need for New Technology

There is a clear need for new technology that would overcome many of these current obstacles. In particular, there is a significant need for small portable sensor units that can be attached to the patient and used for ambulatory clinical applications [21, 22]. A small wireless respiratory gas analysis system would allow for continual ambulatory measures. Having the potential for continual or intermittent wireless feedback on respiratory gas measures could provide unique and important feedback for monitoring health status in several patient groups and has the potential to reduce emergency room visits and reduce health care costs [23, 24].

Early embodiments [25, 26] of respiratory monitors for non-intubated patients have been limited to measurement of respiratory rate alone. In general, current technology cannot provide the range of breath marker measurements that would be useful for many clinical diagnostic applications. For example, current infrared technology can only be used for measurement of CO_2 and O_2 in the breath. Volume of flow and other breath markers mentioned in Section 1.1 that would be useful for many clinical diagnostic applications cannot be measured.

Any sensor developed for the medical industry must be proven safe for clinical testing. To be competitive with existing technology, the developed sensor must be untethered, small, inexpensive and able to be used for ambulatory monitoring. It should also be applicable in home monitoring applications such as sleep apnea and sudden infant death syndrome where it would allow the monitored patient to have natural movements such as turning to the side, moving head, arms and legs. The developed sensor must also eliminate many of the limitations described above of current respiratory analysis technology. Finally, the developed sensors should be extendable to allow additional measurements of anesthetic agents and measurements of various new disease markers in the exhaled breath.

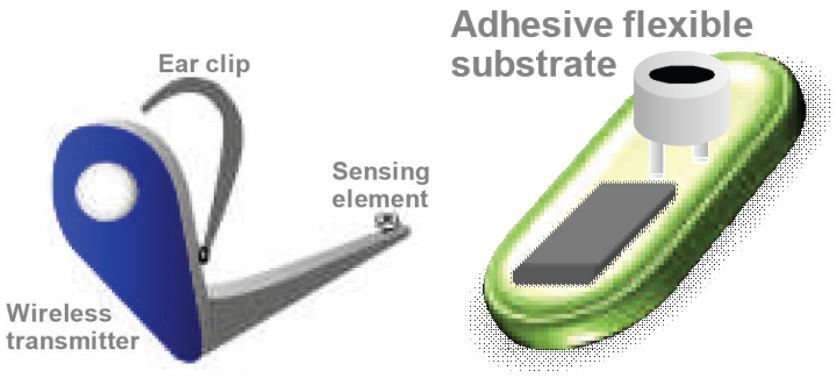

Figure 1.3: Early concepts and preferred embodiments. An ear clip (left) or adhesive strip (right) are two possible solutions for hands-free respired gas sensing.

CHAPTER 2 ELECTROCHEMICAL OXYGEN SENSORS

2.1 Background

Electrochemical sensors have been developed for their ability to measure oxygen concentration in a variety of ambient temperature gas sensing applications. The high selectivity and sensitivity of these sensors provides sufficiently accurate results while remaining relatively small, portable and low cost. To date however, these sensors have been too slow and too humidity sensitive to be used for respiratory gas analysis.

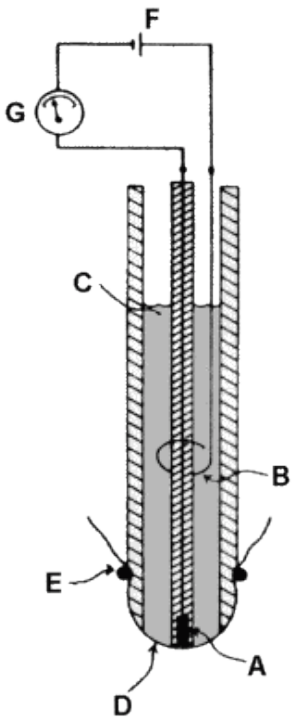

The most commonly used electrochemical oxygen sensors have evolved from the classic Clark cell design [27, 28, 29]. These amperometric gas sensors involve metallic electrodes immersed in an aqueous electrolyte, separated from the gas sample by a semi-permeable membrane. Oxygen is consumed electrochemically, resulting in a flow of electrical current that is directly proportional to the oxygen concentration as predicted by Faraday's law [30]. Disadvantages of the Clark cell design include a slow response time (due to diffusion through membrane), need for continuous stirring, fouling of the membrane, consumption of the electrode (anode) and the possibility of electrolyte leakage [31].

Figure 2.1: Clark-type electrode. (A) Pt-electrode, (B) Ag/AgCl electrode, (C) KCl electrolyte, (D) Teflon membrane, (E) rubber ring, (F) voltage supply, (G) galvanometer [27, 28].

Over the past 20 years, solid-polymer-electrolyte-(SPE) based electrochemical oxygen sensors have been investigated by researchers. The SPE electrochemical cell consists of a solid proton exchange membrane (typically Nafion by DuPont) pressed between three porous electrodes: the working (sensing) electrode, counter electrode and a reference electrode. The 3 electrode cell can be represented by a simple resistive circuit [32] as shown in Figure 2.2. Electrochemical sensors require control circuitry to operate [33]. Traditionally a potentiostat circuit is added to the cell to form a potentiostatic system [34, 35]. A standard potentiostatic system is shown in Figure 2.3.

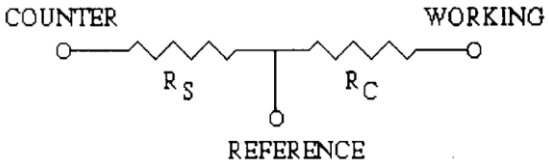

Figure 2.2: Simplified equivalent circuit of an electrochemical cell.

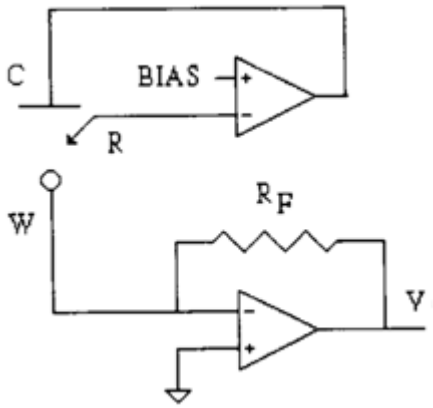

Figure 2.3: Conventional Potentiostatic System. (W= Working, C = Counter, R = Reference).

The standard potentiostat circuit consists of a differential input amplifier which compares the potential between the working and reference electrodes to a required working bias potential. The error signal is amplified and applied to the counter electrode in order to maintain a constant voltage between the working and reference electrodes. A higher resistance results in a decreased current, while a lower resistance results in an increased current, in order to keep the voltage constant as described by Ohm's law.

$$R = \frac{V}{I}$$

As a result, the variable system resistance (R_v) and the controlled current are inversely proportional. A current follower is connected to the working electrode and provides an output voltage that is proportional to the cell current. The output voltage is therefore proportional to the current through the cell.

$$V = \frac{I_{sensor}}{R_f}$$

2.2 Early Solid-Polymer Electrolyte Sensors

In 1989, Yan He-Qing and Lu Jan-Tao from Wuhan University in China reported on the first successful SPE-based oxygen gas sensor [36]. The sensor featured two hydrophobic Teflon-bonded Platinum black layers pressed onto one side of an acid-treated Nafion membrane to act as the sensing and reference electrodes. A chemically-deposited Platinum layer on the reverse side functioned as the counter electrode. A plastic capillary pore or diffusion barrier controlled the flow of oxygen reaching the working electrode. With the diffusion barrier, the diffusion rate limited the reaction at the sensing electrode so that the reaction rate and the output signal were proportional to the oxygen content of the gas outside the sensor. The sensing mechanism of SPE-based oxygen sensors is further described in section 2.4. The sensor cell was controlled by a simple potentiostatic system as shown above. The configuration of this first SPE oxygen sensor is shown below.

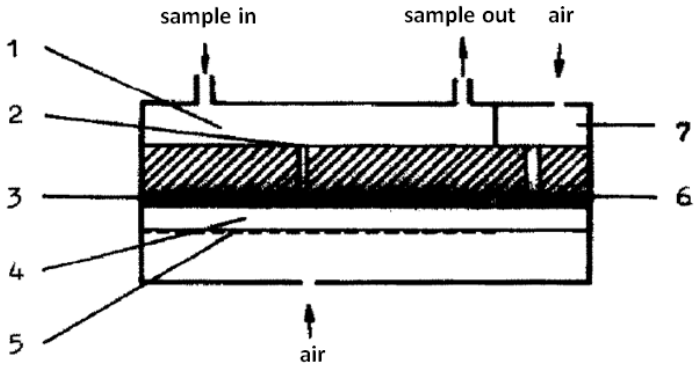

Figure 2.4: **Configuration of early SPE oxygen sensor.** 1). Sample gas chamber, 2). Capillary, 3). Working (sensing) electrode, 4). SPE membrane, 5). Counter electrode, 6). Reference electrode, 7). Air cavity [36].

The first SPE-based oxygen sensors demonstrated many advantages over the Clark-type sensors, including a faster response time (95% response time of 5 seconds versus a 95% response time of 10 seconds for Clark-type sensors), lower temperature coefficient, no electrolyte leakage, simplified electronics and operation, and improved long-term stability. The SPE-based O2 sensor does not consume electrodes or other materials when sensing oxygen, unlike Galvanic cell sensors that typically consume a lead electrode when detecting oxygen. However, the SPE sensor was sensitive to changes in humidity (the sensor output is 35% lower with dry gases than humidified gases) and its performance highly deteriorated at high and low humidity levels [37]. Additionally, the water-retention capacity of the Nafion membrane was shown to be affected by humidity in the environment, which further contributed to the instability of the sensor.

Very few improvements to this original SPE-based oxygen sensor have been published [38]. While membrane dehydration can be avoided by the incorporation of a water container or by passing the gas through a humidifying water bath, this makes the sensing system more complicated and maintenance free operation of the sensor is not achieved. However, a group at the Royal Melbourne Institute of Technology noted that internal humidification is possible based on the reduction principle and the back diffusion of water [39]. Evaporation of water produced at the counter electrode was reduced by using a Teflon bonded platinum counter electrode.

To date, the primary intended use for SPE-based oxygen sensors has been methane and oxygen meters for coal-mine shaft safety and similar applications. While medical applications such as integration into oxygen supply systems and breath physiology have been suggested [37], no results have been reported to our knowledge.

2.3 Overview of PEM Fuel Cell Technology

2.3.1 Current Technology

Fuel cells produce electricity from a spontaneous electrochemical reaction between reactants such as oxygen and hydrogen, although other fuels besides hydrogen can be used [40, 41].The most common type of fuel cell is the solid polymer electrolyte fuel cell (SPEFC). The SPE fuel cell contains the same proton conducting membrane as SPE-based O_2 sensors, which separates the anode and cathode sides of the cell. SPE fuel cells are more commonly referred to as proton exchange membrane fuel cells (PEMFC). Originally used for space missions and other special applications, PEM fuel cells were not developed for wider applications until the 1980's. As a result, much research was being done around the same time as the first SPE-based O_2 sensors were being investigated [42].

The main components of a fuel cell include the membrane electrode assembly and the flow field plates. The membrane electrode assembly (MEA) consists of an electrolyte or PEM pressed between two electrodes and two gas diffusion backing layers. The standard electrolyte material currently being used in PEM fuel cells is the Teflon-based polymer membrane, DuPont's Nafion 117 [43]. The complete MEA structure will be discussed in section 2.5.

The entire MEA is sandwiched between two flow field plates which separate the reactant gases of adjacent cells, connect the cells electrically, and act as a support structure. In addition, the flow field plates have flow channels on both sides with a specific geometry which is designed to optimize the flow velocities and mass transfer rates which directly relate to the fuel cell's performance. The complete PEM fuel cell structure is depicted in Figure 2.5.

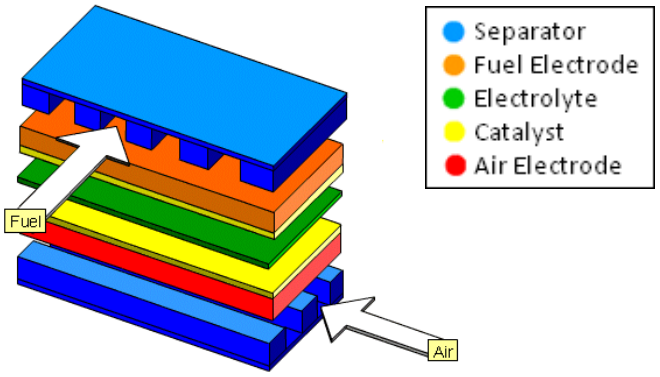

Figure 2.5: Exploded view of PEM fuel cell stack.

2.3.2 Reduction-Oxidation Reaction

In the PEMFC, hydrogen fuels a spontaneous reduction-oxidation (redox) reaction in the electrochemical cell, generating an electron transfer or electric energy. The catalyst at the anode oxidizes the hydrogen fuel creating a positively charged ion and a negatively charged electron. The anode catalyst is usually made up of a very fine platinum powder.

$$Anode \quad Oxidation \qquad 2H_2 \rightarrow 4e^- + 4H^+$$

The electrolyte allows ions to pass through it to the cathode, but insulates against the electrons. Instead, the freed electrons travel through an external circuit. At the cathode (often composed of nickel), the ions and electrons react with oxygen to create water.

$$Cathode \quad Reduction \qquad 4e^- + 4H^+ + O_2 \rightarrow 2H_2O$$

The overall reaction is the combination of hydrogen and oxygen to form water. A block diagram of the fuel cell is shown in Figure 2.6.

$$Overall\ Reaction \qquad 2H_2 + O_2 \rightarrow 2H_2O$$

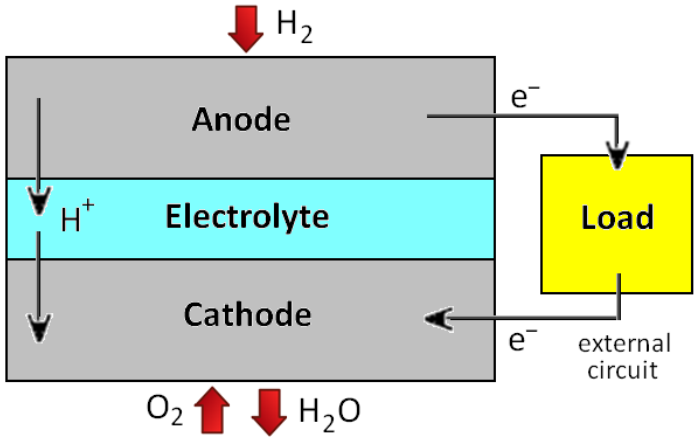

Figure 2.6: Block diagram of a fuel cell. Direction of chemical reaction and electron flow through the load cell.

A single fuel cell produces a voltage of 0.6V to 0.7V at full rated load, which isn't enough to power most devices. To resolve this issue, fuel cell manufacturers stack them together in series or parallel circuits. In a series circuit, the voltage increases with each fuel cell added to the stack. In a parallel circuit, a higher current is supplied with each additional fuel cell. A higher current can also be attained by increasing the area of the electrodes. Since power output is equal to voltage multiplied by current, the total power output of the fuel cell can be increased by stacking multiple cells or increasing their size.

2.3.3 New Technology & Carbon Nanotube-Based Electrodes

In order to reduce high production costs, many companies are working on techniques to reduce the amount of platinum needed in each individual cell. Ballard Power Systems have experiments with a catalyst enhanced with carbon silk which allows a 30% reduction in platinum usage without a reduction in performance [44].

Due to their unique structural, mechanical, and electrical properties, carbon nanotubes (CNT) have been investigated as a replacement for traditional carbon powders in methanol and PEM fuel cells [45, 46, 47, 48]. In theory, multiwalled carbon nanotubes used as a platinum support would reduce the cost of fuel cells through an increased utilization of platinum. Published methods for incorporating carbon nanotubes include

precipitation in a NaOH or KOH base, using CNT powder through a conventional ink process, growing CNT arrays directly onto carbon paper, and a colloidal method using Ethylene Glycol. A study published in 2011 documented the first ever metal free electrocatalyst using relatively inexpensive doped carbon nanotubes that were less than 1% the cost of platinum and were of equal or superior performance [49].

2.4 The Oxygen Gas Sensing Mechanism

2.4.1 Reverse Reduction-Oxidation Reaction

Electrochemical sensors utilize the reverse of the redox reaction that occurs in PEM fuel cells. As described in section 2.3, fuel cells spontaneously react with a fuel source to produce electricity. In the electrochemical sensor, the fuel source and the load are removed. Instead, an external circuit maintains a negative voltage differential applied across the cell (called overpotential). A sufficient overpotential is required in order for the non-spontaneous redox reaction to occur. Driven by the overpotential rather than a fuel source, the sensor cell reacts with a monitored gas. The result is an electrical current through an external circuit which is proportional to the concentration of the reactant gas. In addition to maintaining the desired overpotential, the external circuit is used for measuring, amplifying and performing other signal processing functions on the current.

In the electrochemical oxygen sensors, the oxygen gas diffuses through the electrode structure to the interface between the electrode and the electrolyte. Oxygen gas is reduced to water at the sensing electrode (cathode) by the half reaction

$$Cathode \quad Reduction \qquad O_2 + 4H^+ + 4e^- \rightarrow 2H_2O$$

This reaction requires protons which are supplied by the catalyst. The resultant water migrates through the Nafion to the counter electrode, where it is oxidized to form protons. Thus, the opposing half reaction is

$$Anode \quad Oxidation \qquad 2H_2O \rightarrow O_2 + 4H^+ + 4e^-$$

The oxidized hydrogen protons migrate back through the Nafion to the cathode. The net result is oxygen transfer through the sensor from the working electrode to the counting electrode.

$$Overall \qquad O_2 \ working\ side \ \rightarrow O_2 \ counter\ side$$

The movement of H^+ ions through the electrolyte and the flow of electrons in the electrochemical sensor are shown below. All of the oxygen arriving at the electrode/electrolyte interface is readily reacted and the rate of diffusion is proportional to the gas concentration. Thus, the rate of the reaction (and consequently the current through the external circuit) is linearly proportional to the concentration of oxygen at the sensing electrode.

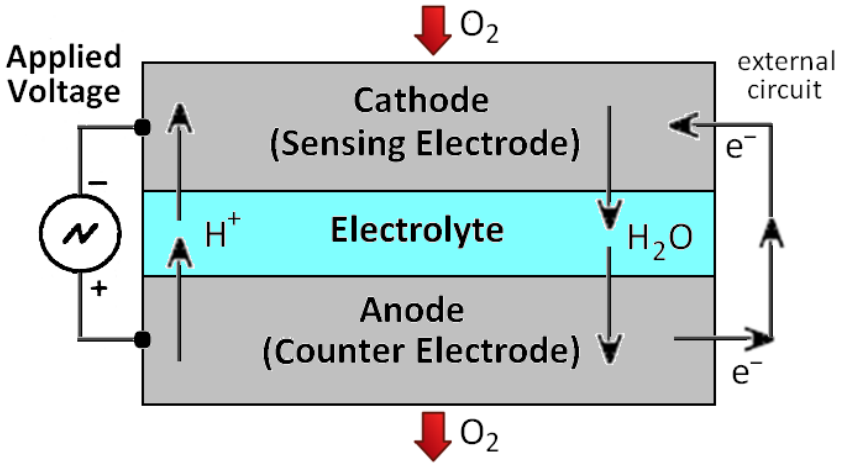

Figure 2.7: SPE-based electrochemical sensor. Block diagram of SPE-based electrochemical sensor.

2.4.2 Triple Phase Boundary

The hydrogen oxidation reaction and the oxygen reduction reaction in SPE-based electrochemical sensors can only occur at confined, spatial sites called “triple phase boundaries” (TPB) [50]. This is where the oxygen gas, electrolyte membrane, and electrically connected catalyst regions are all in contact. For fuel cells, these TPB sites are extensively employed in fuel cell literature because the reaction kinetics often presents significant limitations on the fuel cell’s performance [51].

Therefore understanding, characterizing and optimizing the triple phase boundary content in electrochemical cell provides enhanced sensing performance. The triple phase boundary reaction zones where the catalytically active electrode particles, electrolyte phase and the gas pores all intersect are illustrated in Figure 2.8 below.

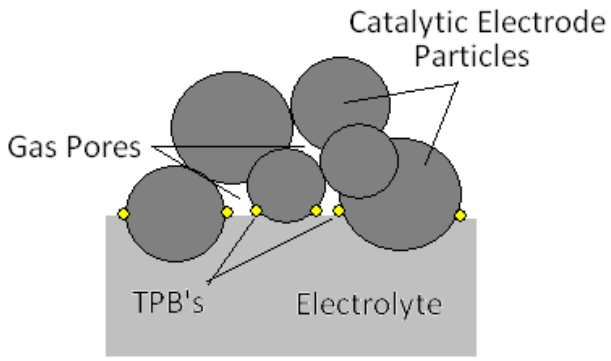

Figure 2.8: Triple phase boundary. Simplified diagram of the triple phase boundary interface in the sensor.

2.5 Electrochemical Oxygen Sensor Components

2.5.1 The Membrane Electrode Assembly

At the heart of the oxygen sensor is the membrane electrode assembly, which was developed for use in fuel cells. The membrane electrode assembly (MEA) consists of 5 essential layers: a proton exchange membrane (PEM or SPE), two platinum catalyst

layers and two gas diffusion layers. The electrodes are a combination of the catalyst and gas diffusion layers. The electrodes are adhered to the electrolyte layer using heat and pressure [40]. A schematic and an image of the MEA are shown below (Figure 2.9).

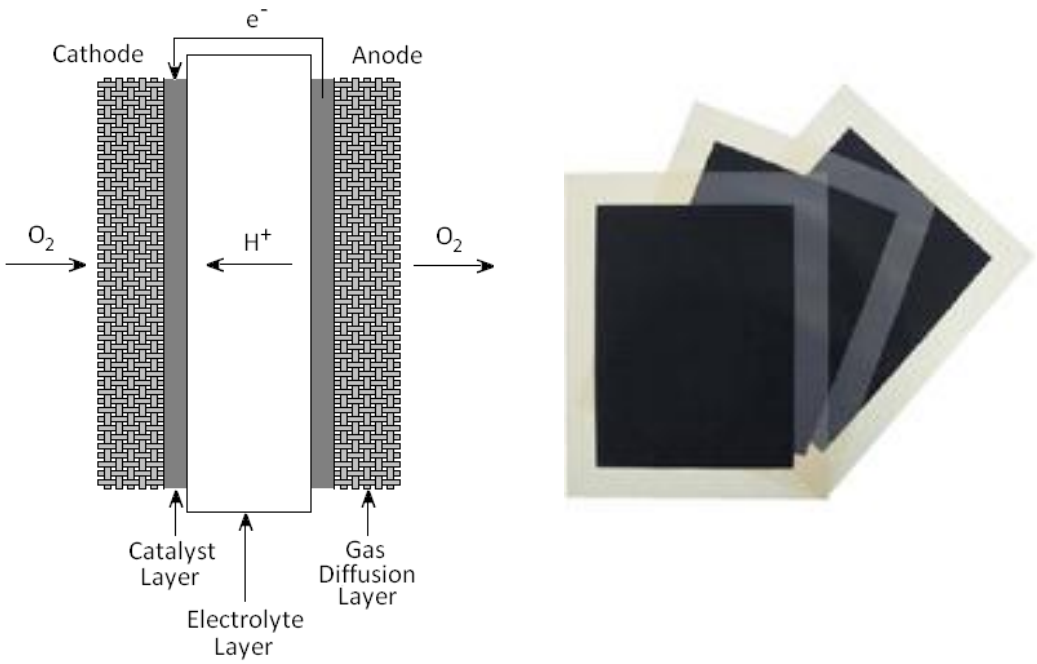

Figure 2.9: The Membrane Electrode Assembly [40]

2.5.2 The Proton Exchange Membrane (Nafion)

The term proton exchange membrane (PEM) is preferred by the fuel cell community but is used interchangeably with solid polymer electrolyte (SPE) in this paper. The electrolyte is a thin membrane pressed between the two catalyst layers in the membrane electrode assembly. The solid electrolyte is ionically permeable while acting as electrical insulation for the two electrode layers. In the sensing application, positively charged hydrogen ions pass through the membrane from one electrode to the other. The membrane must remain hydrated in order to retain proton conductivity. This dependency limits the operating temperature to below the boiling point of water.

Developed by DuPont in the 1960's, Nafion is a sulfonated tetrafulroroethylene based fluoro-polymer-copolymer commonly used as the proton exchange membrane in fuel cells and more recently, in SPE electrochemical sensors [52]. Nafion can be produced as both a powder resin and a copolymer. It is drawn into membranes by heating in aqueous alcohol at 250°C in an autoclave. Nafion membranes consist of a Teflon (PTFE)-based polymer backbone to which sulfonic acid groups are attached. It is these negatively charged sulfonic acid groups that "carry" the hydrogen protons through the membrane and lead to many of Nafion's unique properties. Sulfonic acid has a very high water-of-hydration, absorbing 13 molecules of water for every sulfonic acid group in the polymer. Consequently, Nafion absorbs 22% by weight of water [53]. Nafion is stable in both oxidative and reductive environments and has a high protonic conductivity (0.2 S/cm) at typical operating temperatures.

Figure 2.10: **Nafion membrane example** [54].

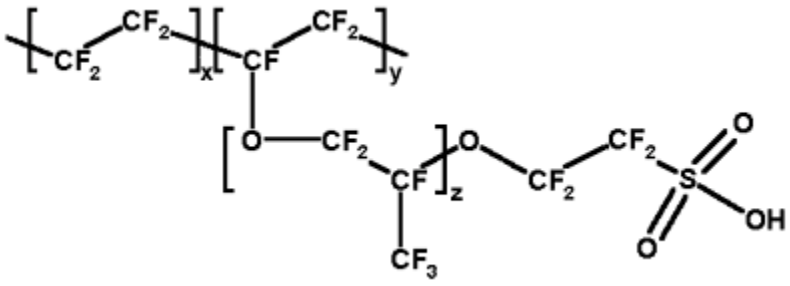

Figure 2.11 [55]: The chemical structure of Nafion [$C_7HF_{13}O_5S \cdot C_2F_4$]. In the sensing application, the H^+ ions jump from SO_3 site to SO_3 site as they move from one electrode to the other through the membrane.

The molecular weight of Nafion is uncertain due to differences in processing and solution morphology. The structure of a Nafion unit (Figure 2.11) illustrates the variability of the material. Instead, the equivalent weight (EW) and material thickness are used to describe the most commercially available membranes. The EW is defined as the weight of Nafion (in grams) per mole of sulfonic acid group [56]. For example, Nafion 117 represents 1100g EW and a thickness of 0.007 inches.

Prior to fabrication of the MEA, the Nafion membrane is typically treated with an acid such as sulfuric acid (H_2SO_4), which removes metal ion contaminants from the surface, improves the moisture retention characteristics and improves the conductivity of ions through the membrane. Additional pre-treatments may be performed before application of the catalyst to remove impurities and improve adhesion of the electrodes. These treatments include polishing with light sand paper, rinsing in temperature controlled deionized water baths to hydrate and dissolve surface contaminants, temperature controlled hydrogen peroxide baths to remove organic contaminants and vacuum drying.

Nafion membranes exhibit exceptionally high chemical and thermal stability. Nafion is stable against chemical attack in strong bases, strong oxidizing and reducing acids, chlorine, hydrogen and oxygen at temperatures up to 125˚C. However, the membrane must remain hydrated in order to retain proton conductivity. This dependency limits the operating temperature to below the boiling point of water. Other issues also arise at higher temperatures such as membrane dehydration, reduction of ionic conductivity, decreased affinity for water, loss of mechanical strength via softening of the polymer backbone, and increased parasitic losses through high hydrogen permeation [57].

2.5.3 The Catalyst and Gas Diffusion Layers

Each MEA requires two pieces of catalyst/electrode material. The catalyst electrode layers are typically made from a mixture of platinum and carbon powder bonded to a gas diffusion layer (GDL). Platinum is used as a catalyst to break up the hydrogen atoms into protons and electrons. The catalyst can be applied to the GDL by any one of several

methods, such as painting, screen-painting, sputter diffusion, electrochemical deposition, electroless deposition, vacuum deposition or mechanical deposition.

The gas diffusion layers are made of a carbon fiber cloth or carbon paper (Toray paper) which is electrically conductive and porous. The GDL is the substrate for the catalyst and promotes the effective diffusion of oxygen to the membrane. Its porous structure allows oxygen molecules to spread out as they diffuse to maximize the contact surface area with the catalyst layer and membrane. The thickness of various gas diffusion materials vary between 0.0017cm and 0.04cm, density varies between 0.21g/cm^2 and 0.73 g/cm^2, and the overall porosity varies between 70% and 80%.

Before the catalyst is applied, the carbon cloth may be treated with a fluoropolymer (Teflon) and carbon black mixture to improve its water management and electrical properties respectively. These Teflon treatments make the diffusion layer hydrophobic. This helps to keep the membrane humidified by allowing only an appropriate amount of water to contact the membrane and promoting back diffusion at the anode (counter electrode) [39]. Wet proofing with Teflon also prevents flooding at the cathode (sensing electrode) by ensuring that the pores in the carbon cloth do not become clogged with water [58]. Untreated carbon cloth pore sizes range from 4-50 microns, whereas Teflon treated pore sizes are much smaller, ranging between 0.1 and 0.5 microns.

For the wet-proofing (Teflon) treatments, the diffusion material is dipped into a 5% to 30% PTFE solution, followed by drying and sintering [40]. The interface with the catalyst layer can be fitted with a coating or microporous layer to ensure better electrical contacts and efficient water transport in and out of the diffusion layer. This layer consists of carbon or graphite particles mixed with a PTFE binder.

2.5.4 Hot-Pressing the MEA

The two catalyst layers and polymer electrolyte need to be fused together for proper mass transfer [40]. Good adhesion is necessary to reduce ohmic losses and to support

the high mechanical stresses produced during operation. Such stresses arise due to dimensional changes in the membrane during hydration and dehydration [59].

The most common method for adhering the two electrodes to the PEM layer is by using heat and pressure. In the heat-press method, the active sides of the catalyst pieces that are to be bonded to the polymer membrane are first coated with liquid Nafion solution. (The coating can be applied with a brush and then dried at room temperature). The three layers (catalyst-PEM-catalyst) are then sandwiched between a set of heating plates under heat and pressure to evaporate the solvents from the liquid Nafion coating. Once the solvents have evaporated, additional temperature and pressure is added before the MEA is allowed to cool to room temperature.

Advantages of the membrane electrode assembly over alternative sensor cell design include extensive testing and publications, high reproducibility and relatively low cost due to the large number of vendors. Some alternate sensor cell designs include catalyst layers which are applied directly to the membrane and alternate catalyst mixtures such as carbon nanotubes combined with powdered platinum.

CHAPTER 3 EARLY EMBODIMENTS

3.1 Introduction

A solid polymer electrolyte-based electrochemical sensing method was chosen for oxygen measurement in respiratory gas exchange analysis due to its low cost, fast response, and small size. Nafion 117 has been documented as the preferred electrolyte in electrochemical applications [59, 60] based on its performance, high selectivity and strong chemical and thermal stability. Platinum-based electrodes are also favored, and a variety of techniques for applying these electrodes have been reported. The two most commonly used techniques for applying the electrodes to the electrolyte are the conventional ink heat-pressing method and the physical vapor deposition method.

In the conventional ink heat-pressing method, the MEA incorporates a carbon supported platinum catalyst powder mixed with Nafion solution and other solvents (such as Teflon) to form an ink. This ink is then coated onto the electrolyte and pressed and heated with porous carbon cloth or paper electrodes.

Sputtering is the preferred method of physical deposition for achieving ultra-low levels of catalyst loading [61] in fuel cell fabrication. For example, a 5nm sputtered platinum film corresponds to a catalyst loading level of 0.014mg/cm^2 (roughly one-tenth the catalyst loading in the inking method). To attain good performance, a sputter-deposited catalyst layer must satisfy the following requirements. First, it should maximize the triple-phase zone where reactant, catalyst and electrolyte are all present together. Second, it should be thin so as to minimize gas diffusion losses, aid in water removal and keep fabrication costs low. Third, the catalyst layer should adhere strongly to the membrane in order to reduce ohmic losses and support the high mechanical stresses produced during operation. Optimal film thicknesses for PEM fuel cells were reported in [61], and are depicted in Figure 3.1. Contrastingly, [60] reported successful Nafion oxygen sensor based on much thicker sputtered platinum films, ranging from 80-150nm.

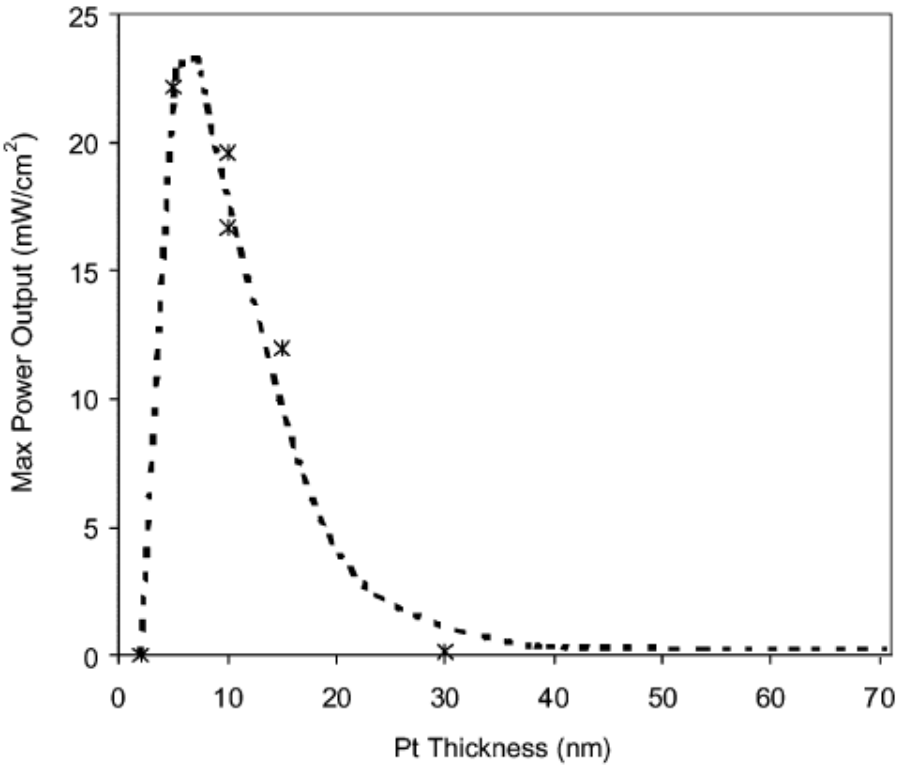

Figure 3.1: Fuel cell performance verses platinum thickness. Published test results for smooth Nafion 117 sputter-coated membrane. In addition to platinum deposits, carbon cloth electrodes were needed to attain sufficient electrical conductivity in the PEMFC [61].

Nafion-based oxygen sensor 95% response times on the order of 2 – 5 seconds were reported [38]. This response time is still too slow however to monitor breath-by-breath oxygen content in respiration. Unfavorable issues with extreme humidity levels were originally reported in [36]. Since then, an improved tolerance to extreme relative humidities has been reported [37, 38, 39]. Regardless, the effects of relative humidity on the sensor must be carefully observed.

3.2 Sensor Fabrication

3.2.1 Sputter Deposition Electrode Fabrication

The electrode/electrolyte films were first fabricated in this project using Nafion 117 membranes and sputter deposition to apply platinum electrodes. The Nafion membranes were purchased in large sheets (30in x 30in) from the DuPont vendors Clean Fuel Cell Energy and Fuel Cell Store. To promote proton transfer and strong catalyst adherence, the membrane was activated by dipping it in six different solutions heated in glass beakers. The membrane sheets were cut into smaller pieces (roughly 5inx5in) with scissors to fit into the beakers without bending. The solutions were each held at 80^{o}C using heating plates. Each beaker held the proton exchange membrane film for one hour in sequence, as follows:

1) 100 mL of distilled (DI) water, to hydrate the membrane and dissolve surface contaminants.
2) 100 mL of 3% hydrogen peroxide solution (USP), to remove organic surface contaminants.
3) 100 mL of sulfuric acid, to remove metal ion contaminants from the PEM surface and sulfonate the PEM surface.
4) 100 mL DI water, to rinse sulfuric acid from the surface and hydrate the PEM.
5) 100 mL DI water, to rise and hydrate the PEM again.
6) 100 mL DI water, for the final rise.

The film remained submerged while in the beakers at all times, and a thermometer was used to ensure the temperature remained constant at 80^{o}C. After the PEM was dipped in each of the beakers for one hour, it was dried for 24 hours in a clean place.

After activation and drying, the Nafion samples were sputtered in Argon gas with a pure Platinum target. Shadow masks were adhered with double sided tape to the membrane to define the active regions. The samples were removed from the vacuum chamber and exposed to ambient atmosphere (clean room) before being flipped over and returned to

vacuum to sputter on the second side. Once the sputtering was completed, the masks and any residual tape were carefully removed. A simple schematic illustrating the sputtering process is shown in Figure 3.2.

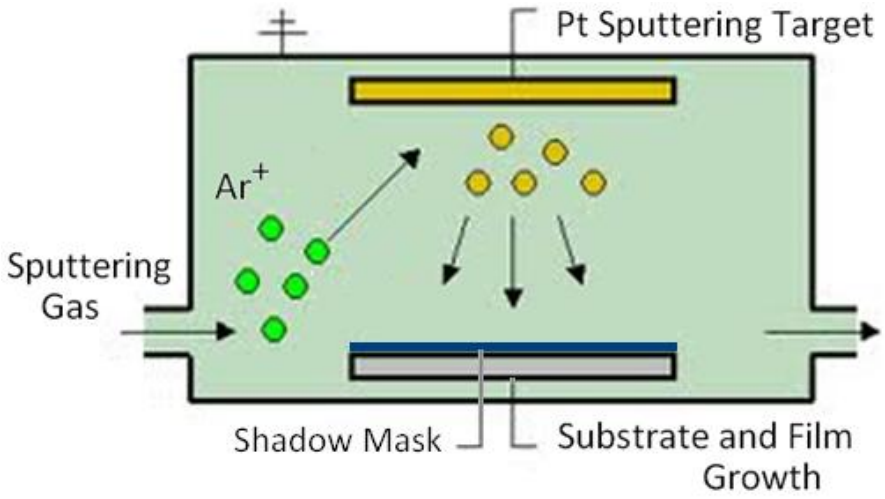

Figure 3.2: Sputter deposition process.

Active regions were sputtered on one or both sides of the membranes, in a variety of thicknesses, shapes, sizes and configurations. The deposited platinum thickness was controlled by the sputtering time. In contrast to the optimal film thicknesses suggested by [OHayre02], thicker films (visible to the naked eye) were fabricated. Sputter conditions were 100W at 0.15Pa, resulting in a sputter deposition rate of approximately 234Å/min (0.4nm/s). Sputter times ranged from 2min - 6min, which corresponds to a nominal platinum thickness of 50nm - 150nm, respectively.

Two different configurations of MEAs were fabricated for oxygen sensing. The first MEA configuration was based on previously reported SPE-based oxygen sensors: a reference and working electrode opposing a third, counter electrode. In the second configuration, the reference electrode was excluded with the working electrode symmetrically opposing the counter electrode in the MEA (similar to PEM fuel cells). The two configurations are depicted in Figure 3.3 and Figure 3.4.

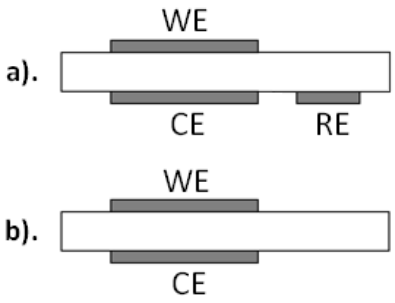

Figure 3.3: Schematic of sputtered MEA assemblies. (Figures are not drawn to scale). Electrodes were sputtered for 4 minutes at 234 Å/min, for a thickness of roughly 100nm, **a).** Three-electrode sensor with 2x3cm counter (CE) and sensing electrodes (WE), and 2x1cm reference electrode (RE). The spacing distance between the counter and reference electrodes was 2cm, **b).** Two-electrode sensor cell with 2.5x2.5cm electrodes.

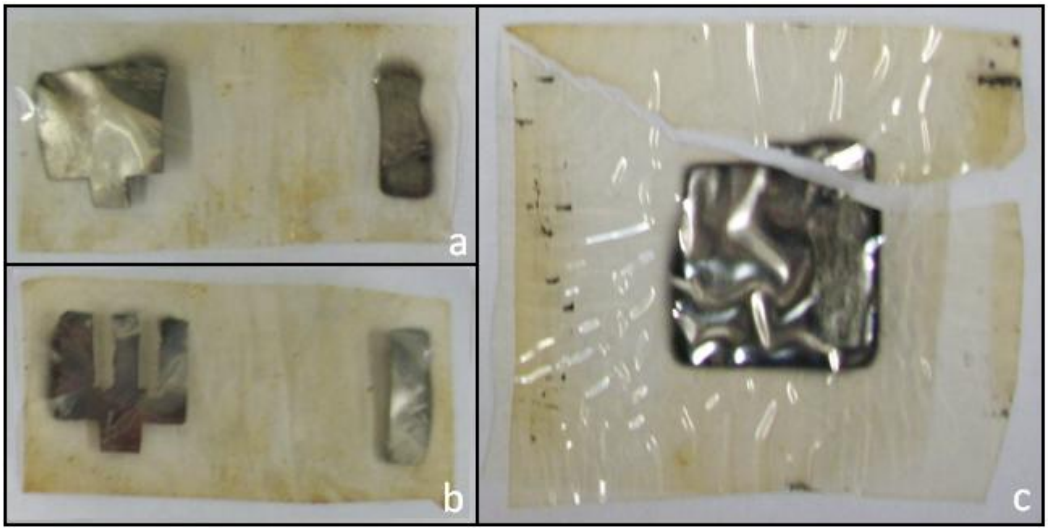

Figure 3.4: Photographs of (used) MEAs with sputtered Pt electrodes. **a).** Counting and reference electrode of standard 3-electrode sensor cell with a sensing electrode (symmetrical opposed to counter electrode) on the reverse side, **b).** Alternate sensing/counter electrode shapes to optimize length of electrode edges, **c).** Two-electrode sensor cell with symmetrically opposing electrodes.

3.2.2 CNT-Based Electrode Fabrication

In an alternative approach to the MEA design, carbon nanotube-based electrodes were attempted. The platinum electrodes were dispersed onto carbon support using the colloidal fabrication method described in [48]. An outline of the general approach is shown in Figure 3.5.

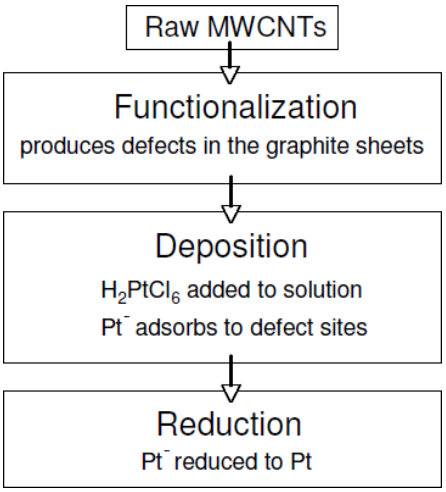

Figure 3.5: Schematic for synthesis of Pt/CNT catalysts [48].

The carbon nanotubes were first functionalized in an acid mixture to introduce surface functional groups for platinum deposition to occur. The fuctionalized CNTs were then sonicated in Ethylene Glycol. A chloroplatinic powder (H_2PtCl_6) was diluted with distilled water and added to the ethylene glycol solution before it was heated in a silicone oil bath. The CNTs were then filtered from the solution, rinsed with de-ionized water and dried. This produced a platinum and CNT composite powder.

The composite powder was then suspended in a solution of iso-propanol, water and Nafion solution. Finally, the catalyst suspension (ink) was ultrasoncated and deposited in droplets directly onto the Nafion membrane or onto the sputtered electrodes.

3.3 Experimental Setup

3.3.1 Gas Handling Setup

The MEAs were placed inside a closed chamber with a gas inlet. A small hole acted as the gas outlet. While gas flowed into the chamber through the inlet, mass balance prevented external atmosphere from entering through the outlet. A humidity sensor placed inside the chamber showed that the humidity decreased as the chamber was purged with dry gas, verifying the complete isolation of the gas flow from the atmosphere.

A two-input fluid mixer was used to mix pure nitrogen and oxygen gas (dry gases). The supply from the mixer was controlled by flow control valves and on/off valves. The desired oxygen concentrations (ranging from 0%-100% O_2) were obtained by controlling the flow rate of each input gas. The relative humidity of the gas mixture was kept constant by bubble humidification in a liquid salt solution (NaCl). A schematic of the gas sensing test setup is shown in Figure 3.6.

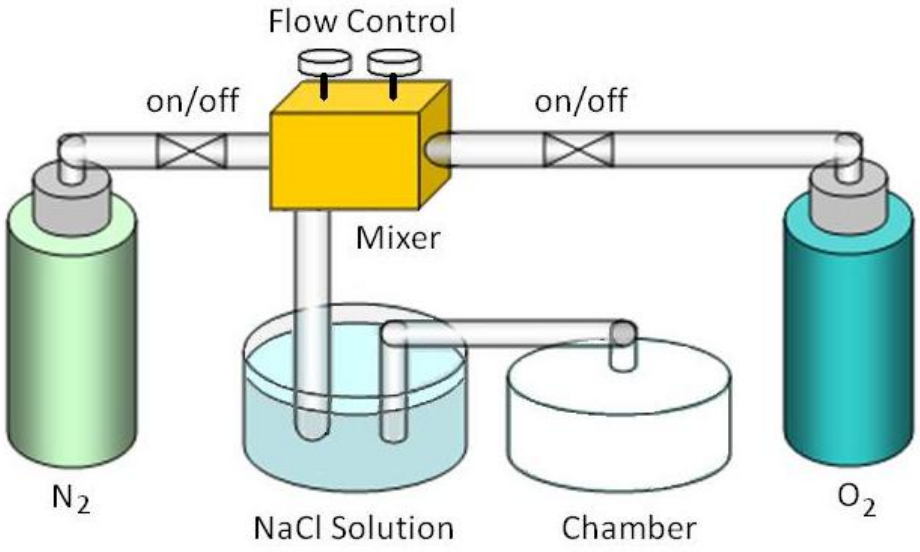

Figure 3.6: Schematic of gas handling test setup.

3.3.2 Control and Measurement Circuits

Two different measurement circuits were initially used to determine changes in the rate of oxygen reduction at the sensing electrode. The platinum electrodes were carefully connected to the measurement circuit using conductive copper tape.

For the 3-electrode sensor, a potentiostat circuit was used. The potentiostat controlled the potential across the cell by sensing changes in its resistance and varying the current supplied to the system accordingly. It also functioned as a measurement circuit, converting a small current signal into a measureable voltage signal. A schematic of the potentiostatic control and measurement circuit is shown in Figure 3.7.

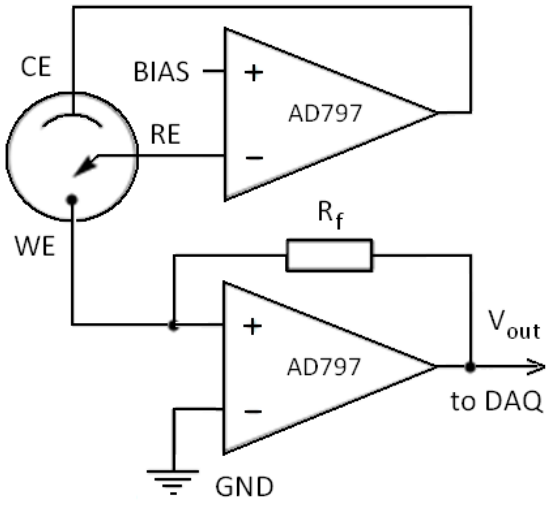

Figure 3.7: Schematic of three-electrode potentiostat measurement and control circuit. Two AD797 low noise, low distortion operational amplifiers, a constant DC power supply and a 10kΩ resistor were used to form the circuit. The control amplifiers amplify the potential difference between the positive and negative inputs. Various bias input voltages ranging from 2V to 3V were used, depending on the minimum overpotential required by the sensor cell.

For the 2-electrode sensor, a control circuit was not required. The measurement circuit was further simplified by reading the voltage across a fixed series resistor rather than using a current to voltage converter. This circuit removed the need for a ±5 volt DC input required by the op amplifiers. A negative input voltage (V_{in}) of 2.5V was applied across the sensor. The output voltage measured across the resistor was proportional to the current through the sensor cell. The 2-electrode sensor can be approximated as a simple resistor, as shown in Figure 3.8. The 2-electrode sensor measurement circuit is shown in Figure 3.9.

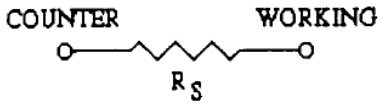

Figure 3.8: Two-electrode equivalent circuit. Equivalent circuit of the 2-electrode electrochemical sensor cell.

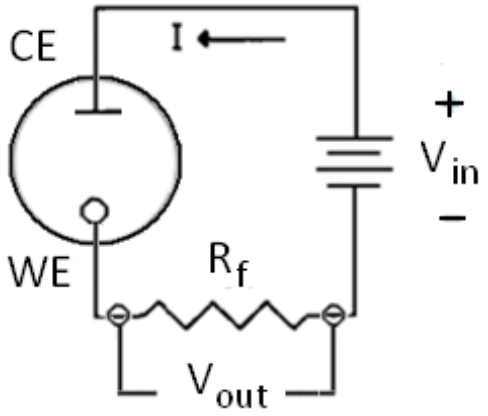

Figure 3.9: Two-electrode measurement circuit. A resistor (2MΩ -7 MΩ) and a constant DC power supply (2V-3V) were used to form the circuit.

The raw analog voltage signal from each of the sensors was analyzed using a National Instruments USB-6211 Multifunction Data Acquisition (DAQ) device. The sampling rate was 100Hz. The DAQ utilized a 16-bit analog input and was controlled by a PC running National Instruments LabVIEW software. LabVIEW software was used to acquire, store and display the real time signal. Data was exported to Matlab for signal post-processing and analysis.

Humidity measurements were made in real time using a 5V, 3-pin TDK humidity sensor. The humidity sensor had a response time of 60 seconds with an accuracy of ±3%RH and a range of 5-95%RH. Reference oxygen measurements were made using a MedGraphics Cardiopulmonary Exercise System (CPX).

3.4 Results and Discussion

The current flowing through the MEA cell was used to analyze the response of the sensor towards oxygen gas. Changes in the current were measured using the measurement circuit. All results were obtained using the experimental test chamber described in Section 3.3.1 and the appropriate measurement circuit depending on the number of electrodes. The data presented is the raw signal from the sensor; the signal was not filtered or post-processed.

3.4.1 CNT/Pt/Nafion Composite Sensor

The first sensor tested was comprised of two-electrodes. The sensing electrode was a circular CNT, Pt and Nafion solution composite with a radius of approximately 3cm. The composite was synthesized using the technique described in Section 3.2.2 and deposited directly onto the Nafion membrane. A square counter electrode was sputtered onto the reverse side of the membrane with an apparent active area of 6.25cm^2. The counter electrode was fabricated using the technique described in Section 3.2.1.

The test chamber was opened to the room to create the background conditions (Atm=20.8%O_2) at the beginning and end of the experiment. The 0% and 25% oxygen conditions were created using the gas handling setup.

The response of the composite sensor to various oxygen concentrations (Figure 3.10***a***) was observed. The developed sensor displayed a clear response to the changing O_2 gas. A slow downward drift was observed in the sensor over multiple results. The sensor also responded slowly to the dryer background gas after being exposed to the humid mixed gas. This suggested that relative humidity was indeed playing a role in the response of the developed sensor membrane.

The true oxygen concentration and humidity in the chamber were captured by a MedGraphics and a TDK humidity sensor respectively (Figure 3.10***b*** and 3.10***c***). The

relative humidity of the gas from the mixer remains relatively constant at around 87%, while the background humidity was much lower. A control circuit is implemented in the next section.

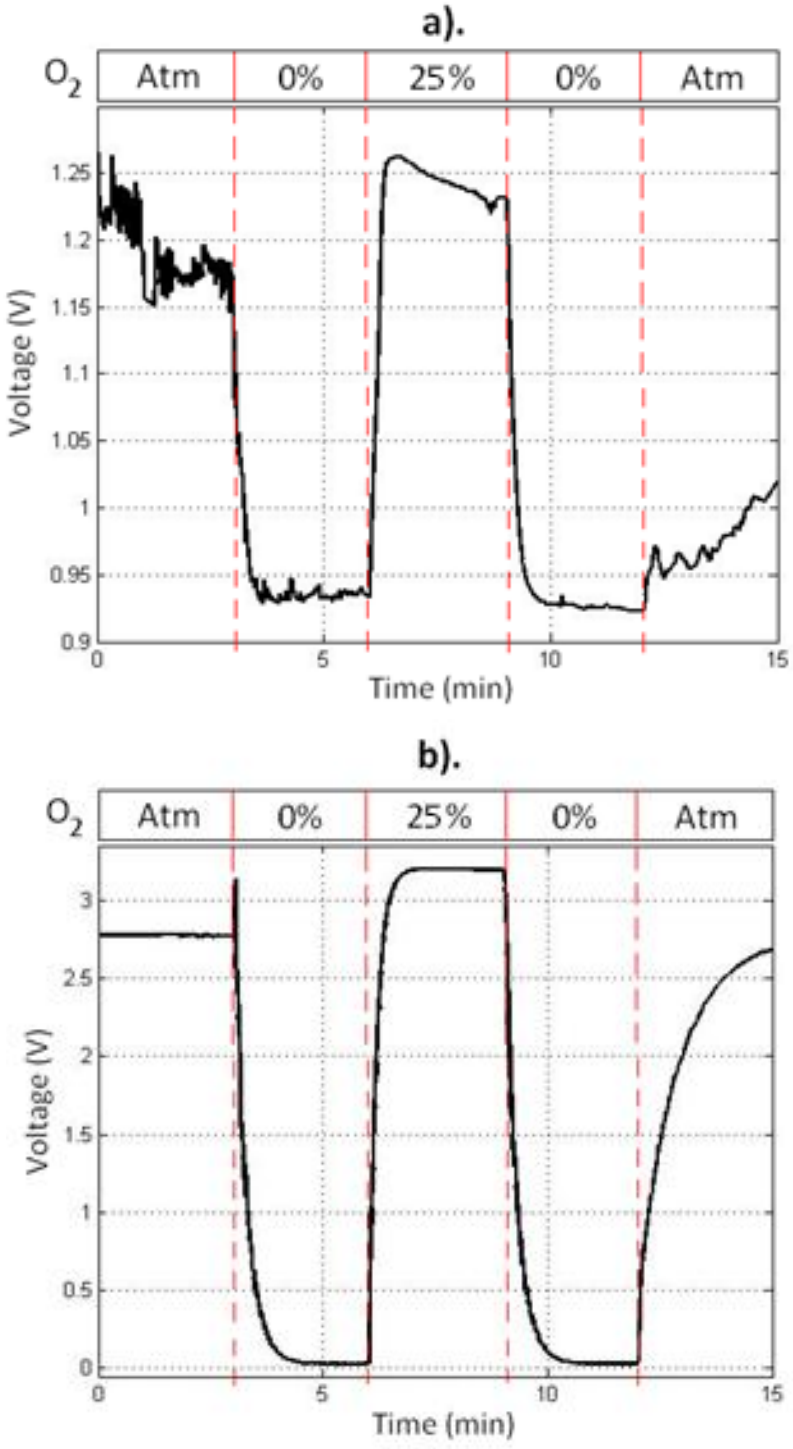

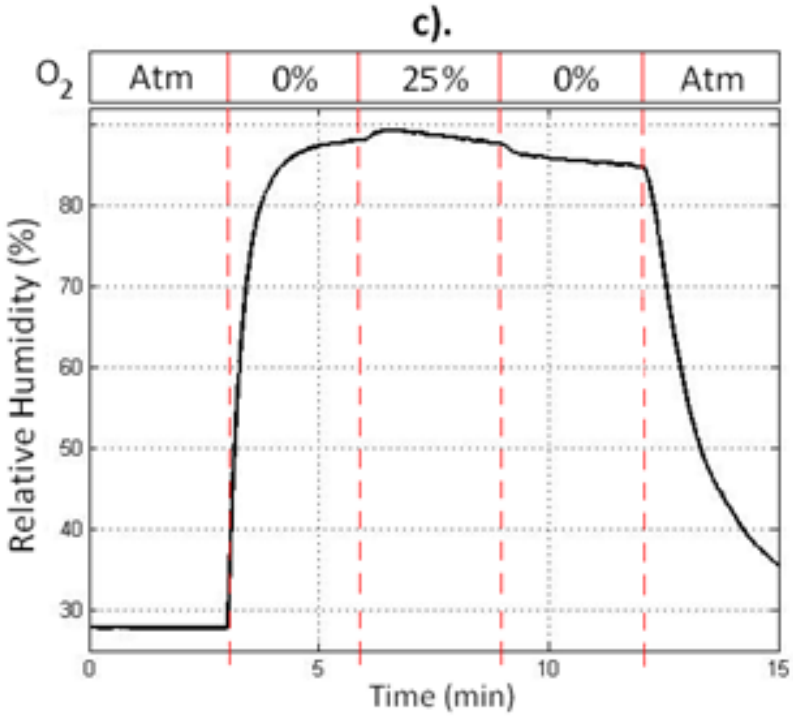

Figure 3.10: Test result from composite sensor. Measured oxygen concentration and humidity levels inside test chamber using background atmosphere and the gas handling set up, **a).** CNT/Pt/Nafion composite sensor response. Voltage measured across a 5MΩ series resistor, input voltage of 2.50V, **b).** MedGraphics oxygen sensor, **c).** Relative humidity measured by the TDK humidity sensor.

3.4.2 Three-Electrode Sensor

The second sensor tested was comprised of three platinum sputtered electrodes. The sensor was fabricated using the technique described in Section 3.2.1. The sensing and counter electrodes were on opposing sides of the membrane. The reference electrode was on the same side as the counter electrode. The sensor membrane electrode assembly is depicted in Figure 3.3 and Figure 3.4. The measurement circuit was the potentiostat described in Section 3.3.2.

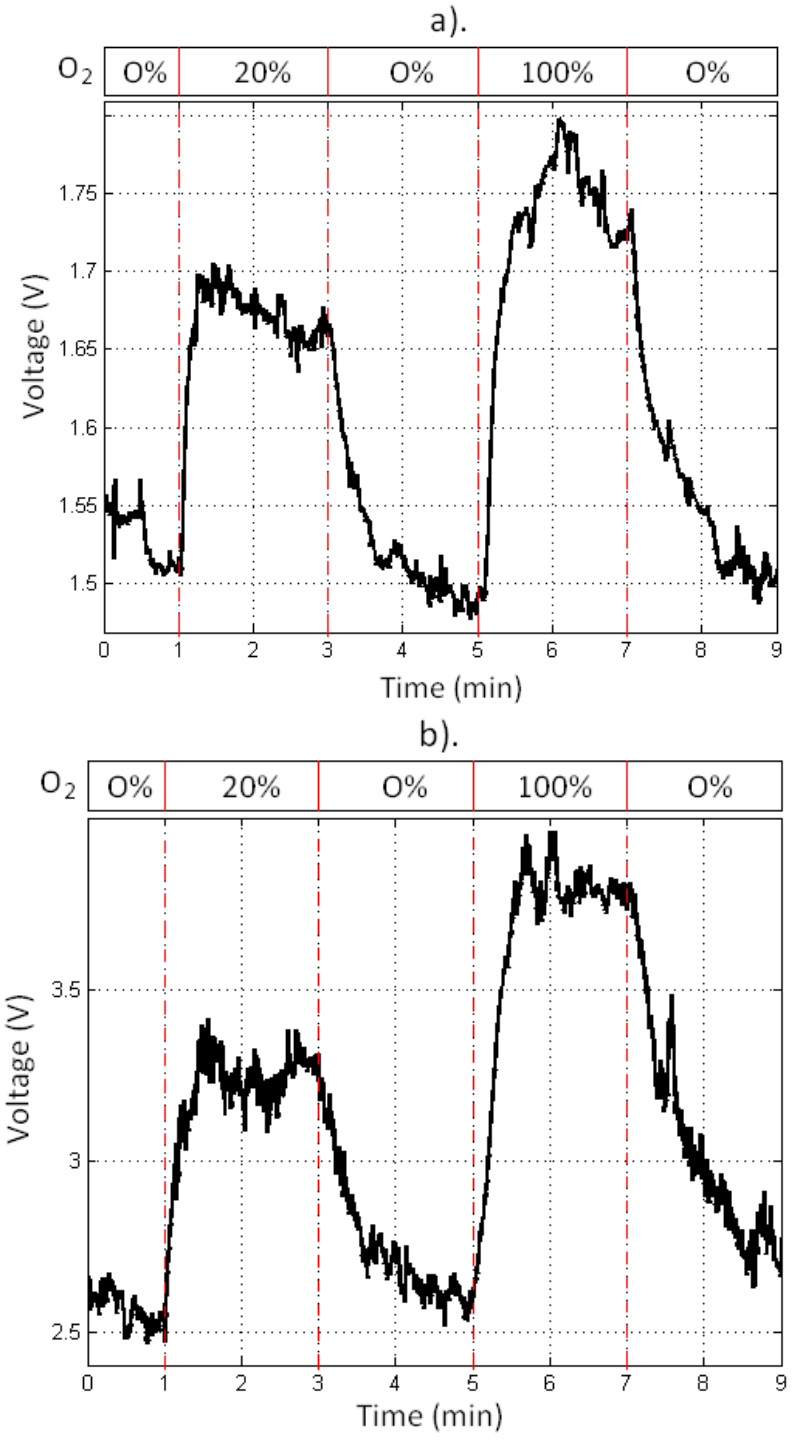

Figure 3.11: Test result from 3-electrode sensor. Oxygen response of 3-electrode sensor using potentiostat control circuit with Rf = 7MΩ, **a).** Voltage input of 0.45V, **b).** Voltage input of 0.82V.

The response of the 3-electrode sensor to various oxygen concentrations was observed (Figure 3.11). The relative humidity of the mixed gas was kept constant at 87.5±2%. The sensor again displayed a clear response to the changing O_2 gas. A slow downward drift was again observed in the sensor output over multiple results. The signal response was improved by increasing the bias voltage supplied to the potentiostat circuit.

The 3-electrode platinum sensor displayed improved sensitivity to the 2-electrode, CNT-based sensor. However, the signal noise was also significantly increased. Both the MEA structure and the addition of the potentiostat control circuit may have attributed to this result. A two-electrode sensor is discussed in the next section.

3.4.3 Two-Electrode Sensor

Next, a simple two platinum sputtered electrode sensor was tested. Again, the sensor was fabricated using the technique described in Section 3.2.1. The sensing and counter electrodes were on opposing sides of the membrane. The sensor membrane electrode assembly is depicted in Figure 3.3 and Figure 3.4. The measurement circuit was the simple series circuit described in Section 3.3.2. For this set of tests, data from the MedGraphics analyzer was collected separately to ensure that the pneumatic sampling was not interfering with the results from the developed sensor.

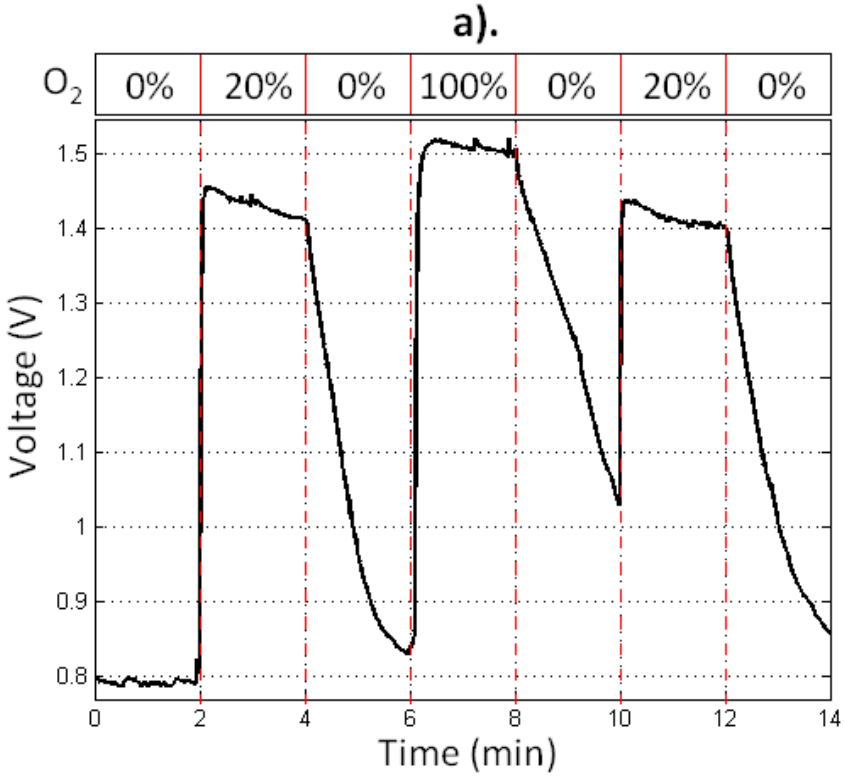
a).
O_2
0%
20%
0%
100%
0%
20%
0%
Voltage (V)
Time (min)

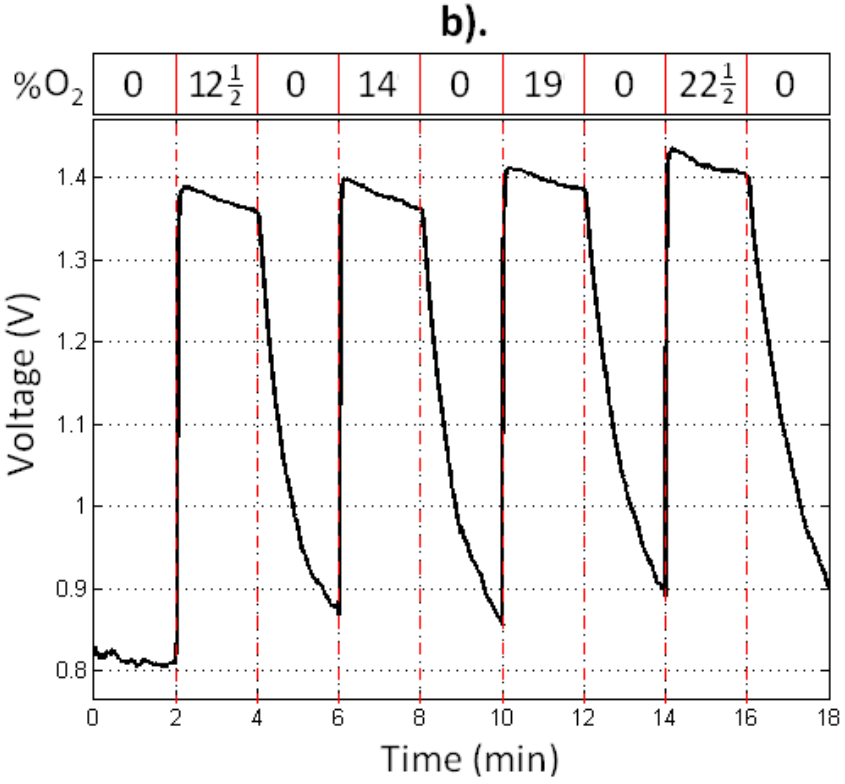
b).
$\%O_2$
0
$12\frac{1}{2}$
0
14
0
19
0
$22\frac{1}{2}$
0
Voltage (V)
Time (min)

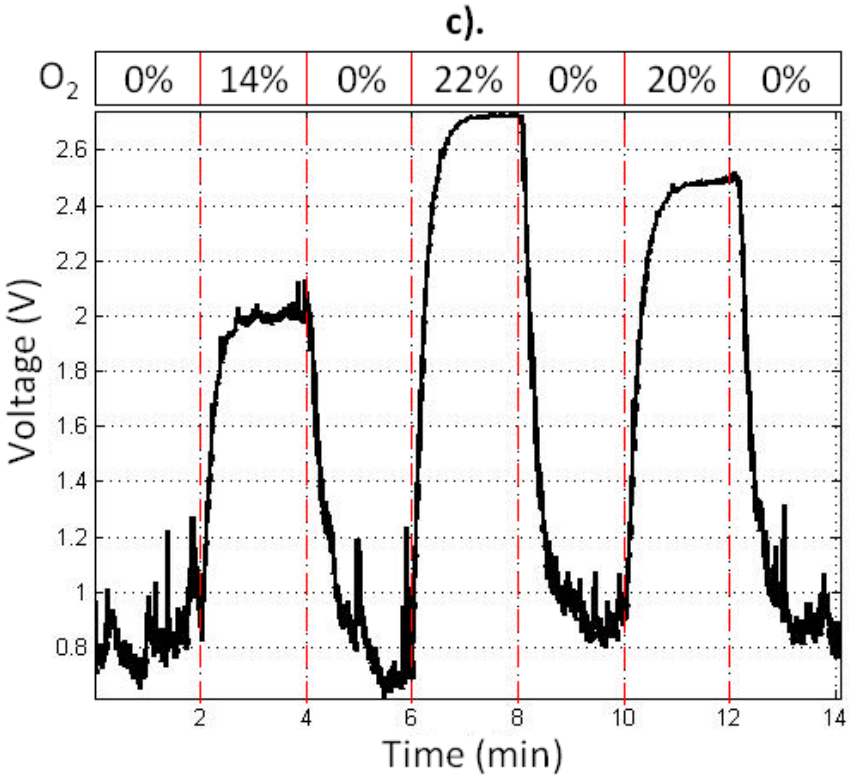

Figure 3.12: Test result from two-electrode sensor. a). Two-electrode Nafion sensor inside test chamber at constant humidity with input voltage of 2.5V, **b).** Incrementing O_2 concentration at constant humidity with input voltage of 2.5V, **c).** MedGraphics sensor placed inside test chamber for separate test under identical conditions.

The response of the 2-electrode sensor to various oxygen concentrations (Figure 3.12***a*** and Figure 3.12***b***) was observed. The relative humidity of the mixed gas was kept as constant at a lower humidity of 53±2%. The sensor again displayed a clear response to the changing O_2 gas. A slow downward drift was again observed in the sensor output over multiple results.

The 2-electrode showed a very fast response to the addition of any oxygen concentration into the test chamber. This result appeared to be artificial when compared to the actual oxygen concentration measured by the MedGraphics analyzer (Figure 3.12 ***c***). However, the MedGraphics analyzer used a pneumatic sampling system which allows for more gas to be sampled and therefore resulted in a more averaged measurement of the oxygen concentration within the chamber.

3.4.4 Support Casing

To improve upon the initial design, a simple casing was developed for the two-electrode sensor. The main function of the casing was to add rigidity to the senor and to protect the exposed Nafion membrane (the areas surrounding the electrodes). When exposed Nafion membrane comes in direct contact with water vapor, it's physical, chemical and electrical properties change. As a result, direct moisture contact with the exposed Nafion should be avoided wherever possible. The casing also provided a means of handling the sensor without adding to the regular wear-and-tear or leaving fingerprints which could degrade its performance.

The casing involved two thin plates which covered the top and bottom surface of the MEA. In one embodiment, the top surface exposed just the edges of the sensing electrode. This is the area in which the triple phase boundary was optimized. In another embodiment, the top casing layer exposed the entire sensing electrode. The bottom layer of the casing was perforated to allow for exposure of the counter electrode to the background atmosphere. The simple casing is depicted in Figure 3.13.

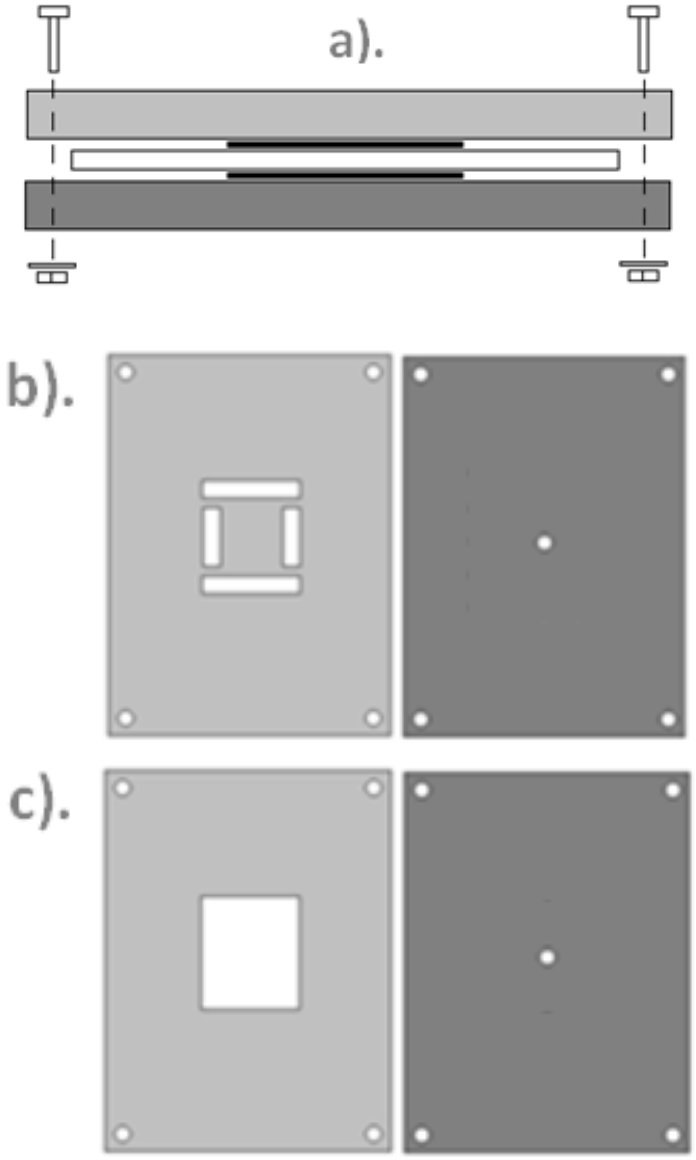

Figure 3.13: Casing for sputter-fabricated sensor. a). Overall support structure designed to add rigidity to the sensor, **b).** First variation, designed to enhance the gas diffusion to the triple phase boundary, **c).** Second variation, designed to expose the entire sensing electrode.

3.4.5 Relative Humidity and the Response to Expired Oxygen

The effect of relative humidity on the sensor was studied using the 2-electrode sensor enclosed in the casing shown above. The humidifying bath was removed from the test set up and the oxygen concentration was varied from 0% to 20% at roughly 0% relative humidity. The humidifying bath was then quickly added to establish a relative humidity of approximately 55%. The measurement was resumed with oxygen concentration varying from 0%-20%. The results in Figure 3.14*a* and Figure 3.14*b* clearly show the sensitivity of the gas sensor to the relative humidity level.

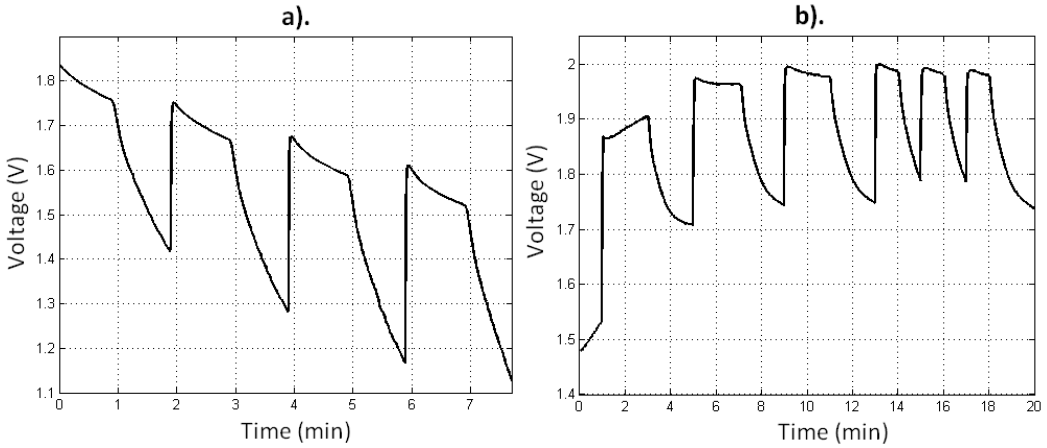

Figure 3.14: Test result of sensitivity to humidity. a). Sensor response drifts when exposed to dry gas, **b).** Sensor response balances out when 55% relative humidity is restored to the gas.

Finally, the sensor was tested using expired breath. The MEA was removed from the test chamber and placed into the support casing. The sensor was laid flat with the sensing electrode facing up. Breaths were administered directly onto the sensor from a distance of 5cm.

The expired breath sequence and the sensor response are shown in Figure 3.15. For individual breaths, the sensor shows the expected response. However, the return to the

initial concentration once the breath has stopped was very slow (5-30 seconds). Furthermore, a sequence of breaths spanning several seconds resulted in an inverse response. This result was likely due to the moisture level increasing at the sensor with repeated breaths. Finally, the result shows that the response to expired O2 was larger than the response to dry N2. This indicates that the selectivity of the sensor is not very high. Humidity and perhaps flow rate both appeared to be factors.

Time (min)	Duration (sec)	Gas
0	60	Background Air
1	3	Expired Breath
2	3	Expired Breath
3	30	O% oxygen (low flow rate)
5	3	Expired Breath
6	3	Expired Breath
7	20	10 Consecutive Exhaled Breaths

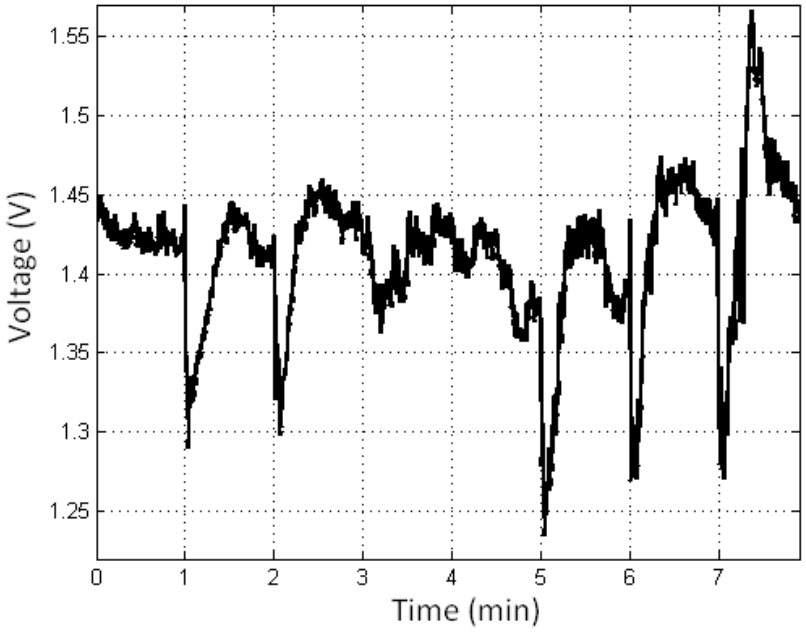

Figure 3.15: Sensor response to expired breaths. First successful test of 2-electrode sensor reaction to expired breath.

3.5 Conclusions

Three different configurations of MEA were developed for oxygen gas sensing using both sputtered platinum electrodes and platinum electrode composites mixed with CNTs and Nafion solution. Control and measurement circuits were used to detect changes in the rate of the redox reaction caused by varying oxygen gas concentration.

The responses of each of sensors to varying oxygen concentration were compared. The magnitude and response time of the three sensors were very similar under parallel test conditions. The potentiostat circuit was able to produce the largest response, due to its inherent ability to amplify the signal. However, the potentiostat also increased the signal noise and required a larger power supply. Meanwhile, the addition of CNTs via the composite ink solution showed no improvement over the pure platinum electrodes.

Over multiple testing, the 2-electrode sensor displayed the most consistent and repeatable results. In addition, the simplicity of fabricating, controlling, and measuring the 2-electrode sensor made it the preferred design choice for further development. In this embodiment however, the sensor did not perform well enough to be used for breath-by-breath respiratory analysis. Further development was required to improve the magnitude, response time, and selectivity of the sensor.

CHAPTER 4 PEMFC-BASED OXYGEN SENSOR (1st Generation)

The 2-Pt-electrode sensor was chosen as the preferred membrane electrode assembly in the previous chapter. The sensor showed some initial response to expired breath but its performance deteriorated quickly and it was cross-sensitive to humidity and flow rate. In addition, the sputter deposition of pure platinum electrodes onto the Nafion electrolyte proved both costly and time consuming.

In response to the recent demand for alternative energy sources, the manufacturing and development of fuel cells and fuel cell technology has become a well-recognized industry in the global market. As of 2010, hundreds of fuel cell developers were established worldwide [62]. As a result, relatively inexpensive PEMFC MEAs could be readily purchased with highly customized specifications. For example, state-of-the-art MEAs with similar sized electrodes could be purchased in the United States for roughly half the cost of the sputtering techniques described in the previous chapter.

Several fuel cell vendors were selected based on customer reviews to fabricate new membrane electrode assemblies. The orders were fabricated to specification and safely delivered where they were tested for their response to gases, humidity and other factors associated with breath. They were then incorporated into a unique sensor design for breath-by-breath oxygen measurement.

4.1 Sensor Fabrication

New MEAs were made-to-order from the fuel cell vendor Clean Fuel Cell Energy. The PEM used in the sensor MEA was a 5x5cm piece of 175µm thick Nafion 117 membrane from DuPont. The Nafion membrane used was brand new and therefore did not require any pretreatment. Platinum particles were mixed at 20% weight with Vulcan XC72 carbon black to improve the electrical conductivity of the catalyst. Carbon cloth gas

diffusion layers (GDL) were used to support the catalyst and improve the electrical conductivity of the electrodes. Each carbon cloth GDL was cut to 2.5x2.5cm, had a thickness of 350µm, a density of 0.4g/cm^3 and an overall porosity of 70%-80%. Select carbon cloth electrodes were chosen to be treated with a fluoropolymer (Teflon) to improve their water management properties. The untreated carbon cloth pore sizes ranged from 4-50 microns, whereas the Teflon treated pore sizes ranged from 0.1 to 0.5 microns.

The electrode fabrication process was as follows:

1) Pretreatment of the Nafion (was not required for brand new Nafion membranes).
2) Platinum and carbon particles were placed into a beaker with water and sonified.
3) Teflon solution was added to the beaker to create a platinum ink solution.
4) Platinum ink solution was poured onto filter paper and vacuum dried to form an even layer on the filter paper.
5) The GDL was placed on top of the dried layer.
6) The MEA was top-pressed and then baked in an oven.
7) Nafion treatment was applied before the MEA was again baked in the oven.

MEAs were fabricated with 0.5mg/cm^2 or 1.0mg/cm^2 catalyst loading for comparison.

Hydrophobic Toray carbon paper was later used as an alternative backing layer for comparison. The active areas of the electrodes were chosen to be the same for the paper as the cloth electrodes, with catalyst loading was 1.0mg Pt/cm2. Ultimately, both the performance and durability of the carbon cloth electrodes were favored for the oxygen sensing application.

New casing was designed to facilitate respiratory gas analysis. The sensor casing protected the MEA and optimized air flow over the sensing electrode. This first generation casing included a 2.5cm diameter plastic tube which provided a useful interface for respiratory analysis. For example, a mouthpiece could be easily added

(Figure 4.x). The plastic casing consisted of three separate layers which supported the breathing tube and the MEA. The unique layer design also provided a cross flow channel which removed stagnant air from the sensing surface. The layers bolted tightly together to prevent unwanted gas or moisture leakage. The original model of the sensor is shown in Figure 4.1.

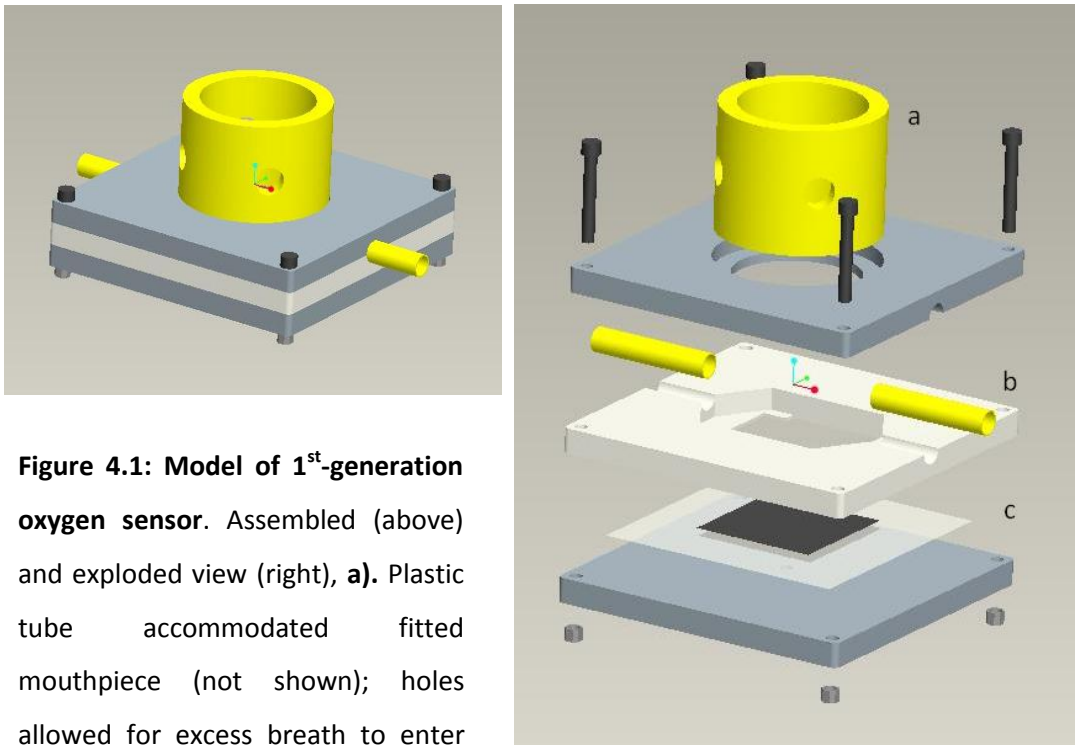

Figure 4.1: Model of 1st-generation oxygen sensor. Assembled (above) and exploded view (right), **a).** Plastic tube accommodated fitted mouthpiece (not shown); holes allowed for excess breath to enter and escape through the tube, **b).** Cross flow channel fitted between top and middle channel and connected to a pump, **c).** MEA pressed between middle and bottom plate.

Copper threads were used to connect the electrodes to the measurement circuit within the sensor casing. A 2.5LPM free flow diaphragm pump from Hargraves Fluidics (CTS Series) was used to generate the cross flow. The prototype sensor that was used for testing is shown in Figure 4.2.

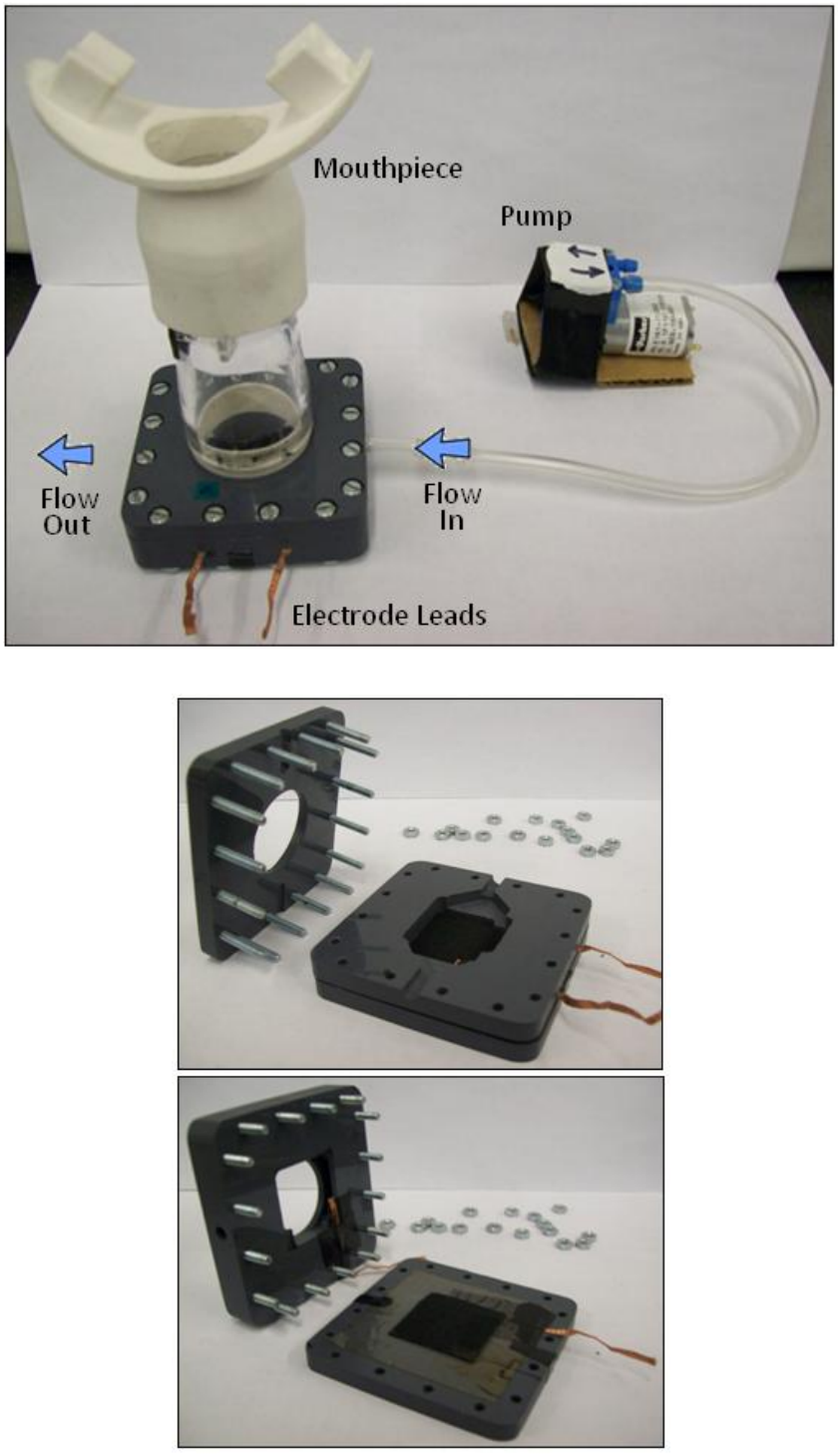

Figure 4.2: Photographs of 1st generation oxygen sensor. Prototype oxygen sensor and assembly, including mouthpiece and pneumatic sampling system.

4.2 Results and Discussion

4.2.1 Sensitivity to Dry Gas and Changing Relative Humidity

The response of the PEMFC-based sensor to changes in oxygen concentration was observed using the series resistor measurement circuit described in Section 3.3.2. The MEA was first tested in the test chamber described in Section 3.3.1 to analyze the effects of varying humidity conditions on the sensor. Relative humidity was controlled by bubbling the dry test gas through a saline solution. The performance of the oxygen sensor under two different humidity conditions is shown in Figure 4.3.

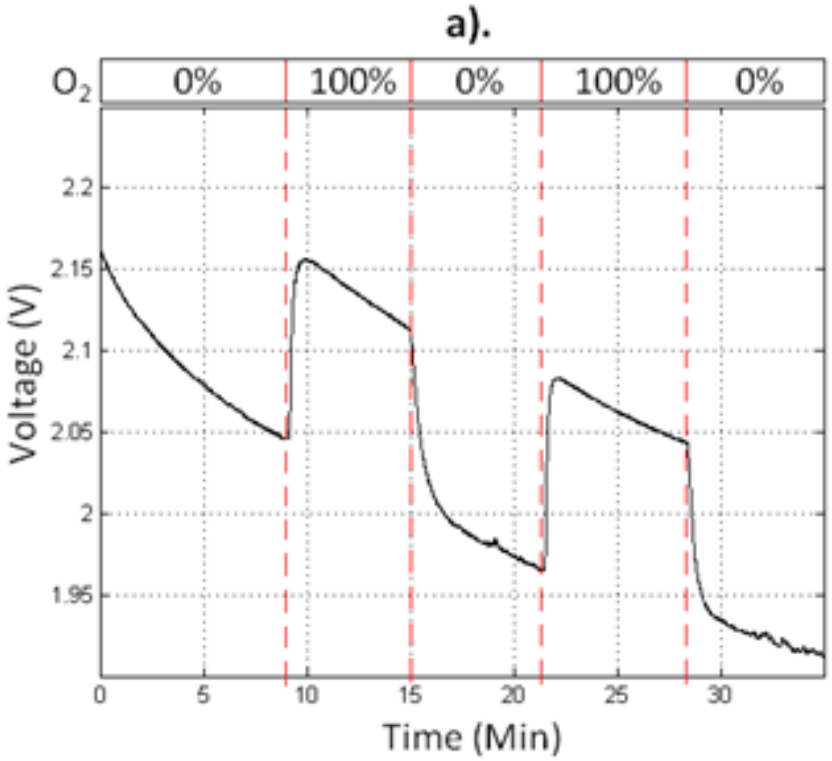

Figure 4.3: Sensor response to oxygen. Gas varied from 0% (100% N_2) to 100% O_2. **a).** Dry test gas, approximately 0% relative humidity, **b).** Humidified test gas (55-60% relative humidity) after being passed through humidifying bath, **c).** Relative humidity of the background room atmosphere and test gas monitored under similar test conditions.

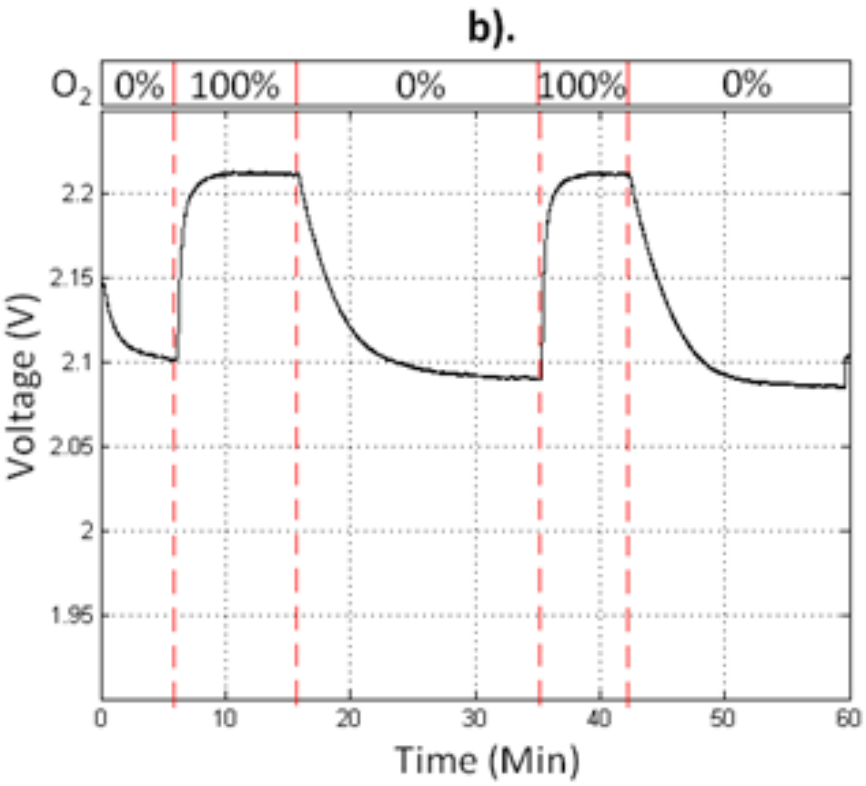
b).
O2
0%
100%
0%
100%
0%
Voltage (V)
2.2
2.15
2.1
2.05
2
1.95
0
10
20
30
40
50
60
Time (Min)

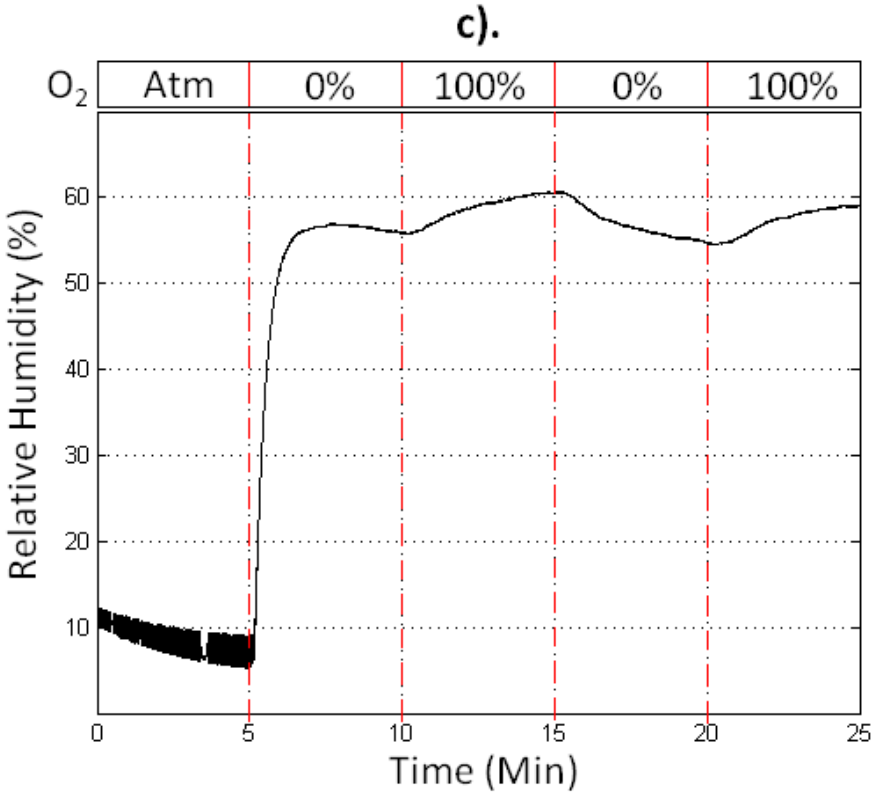
c).
O2
Atm
0%
100%
0%
100%
Relative Humidity (%)
60
50
40
30
20
10
0
5
10
15
20
25
Time (Min)

In addition to the expected oxygen response, a slow drift in the sensor output was observed unless a constant humidity threshold was obtained. The rate of the downward drift increased as humidity was removed from the test chamber. Under completely dry conditions, the sensor response drifted significantly at rates of up to 0.1V (or 10% of total O_2 response) per minute. When the relative humidity was kept in the range of 55-60% RH, the drift was greatly reduced. At relative humidity levels above 60%, no downward drift was observed.

Similar to the sputtered MEA results discussed in the previous chapter, the new MEA showed a strong response to oxygen as well as a cross-sensitivity to humidity. However, unlike the sputtered MEA results, the magnitude of the response of the new MEA did not deteriorate at lower relative humidity levels. The fact that the response did not deteriorate indicated that the new MEA had improved water retention characteristics. This was attributed to the addition of the Teflon coated gas diffusion layer in the MEA.

4.2.2 Sensitivity to Respired Breath

The response of the PEMFC-based sensor to respired breath was observed using the PEMFC MEA and the sensor casing described in Section 4.1. The voltage input to the sensor was 2.65V and the series resistor in the measurement circuit was 2MΩ. The raw data was post processed using Matlab. The signal was digitally filtered using a 2^{nd} order high pass butterworth filter with a normalized cutoff frequency of $0.2/f_s$, where f_s = 10Hz was the sampling frequency. The *filtfilt* command in Matlab was used to attain zero-phase distortion and to minimize start-up and ending transients. The actual oxygen concentration of the respired breath was measured using the MedGraphics Cardiopulmonary Exercise System. The sensor response to expired oxygen is shown from two different data sets in Figure 4.4 and Figure 4.5.

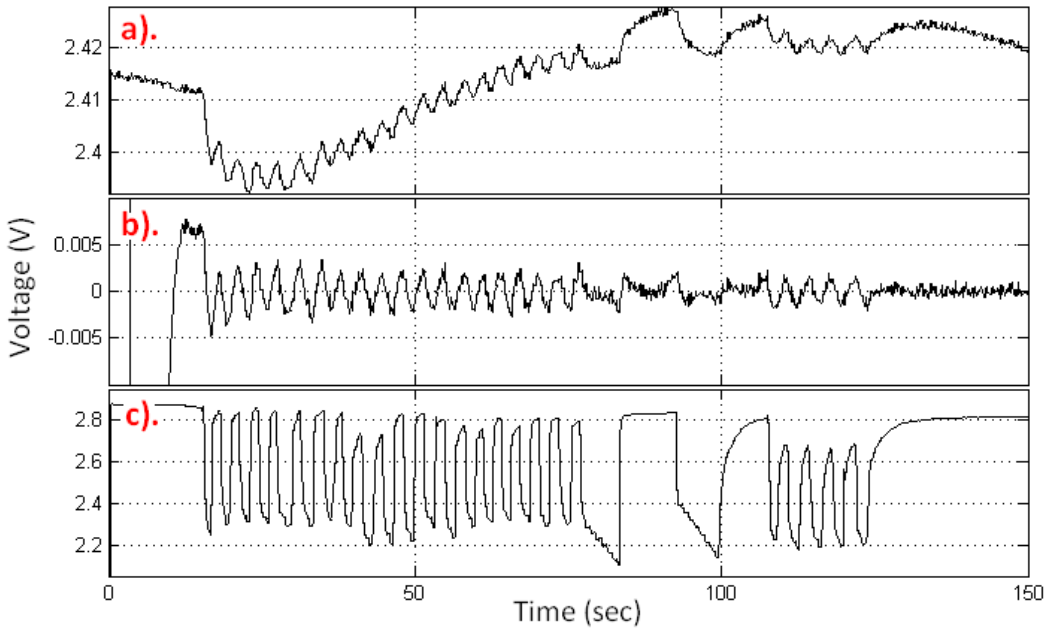

Figure 4.4: Sensor response to expired oxygen in human breath. Data set #1 **a).** Raw data from the developed sensor, input voltage of 2.65V, **b).** Filtered data from the developed sensor, **c).** Reference signal from the MedGraphics analyzer.

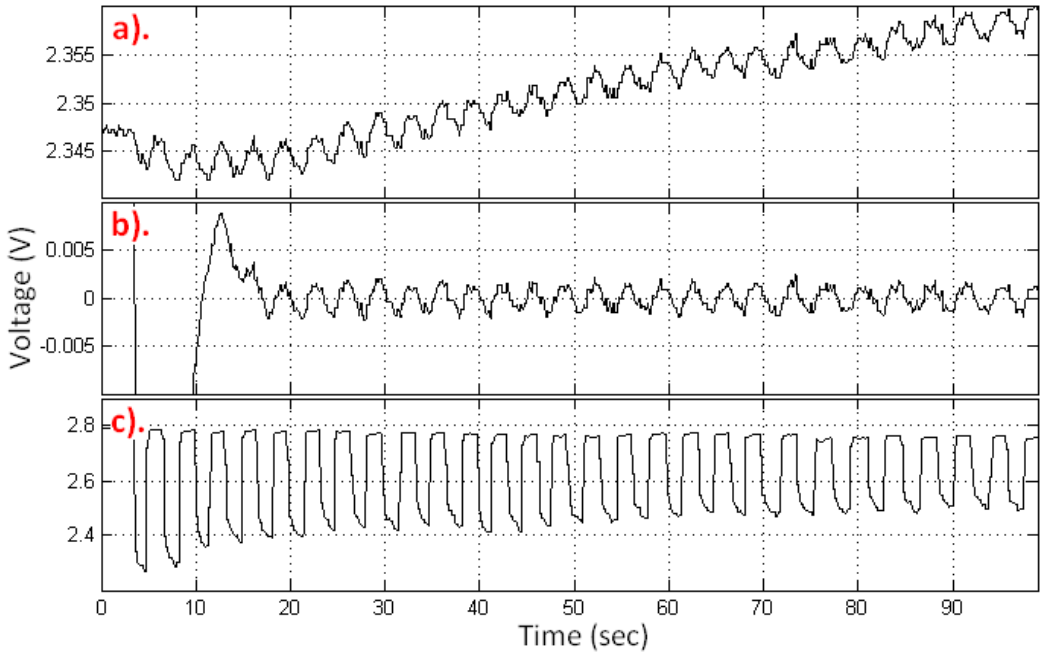

Figure 4.5: Sensor response to expired oxygen in human breath. Data set #2, **a).** Raw data from the developed sensor, input voltage of 2.65V, **b).** Filtered data from the developed sensor, **c).** Reference signal from the MedGraphics analyzer.

The PEMFC MEA-based oxygen sensor showed an improved response to breath over the sputtered platinum MEA-based sensor discussed in Chapter 3. The response did not deteriorate over continuous run time or multiple tests. For example, the sensor showed no decrease in performance over half an hour of continuous breathing. The 95% response time of the sensor was approximately 1-3 seconds in the presence of expired breath and 3-5 seconds to return in the absence of breath. The return response was improved by inhaling air through the sensor or by increasing the cross flow rate provided by the pump. The response time was sufficient for tracking breathing rates up to 20 breaths per minute. Faster breathing rates resulted in a deteriorated performance due to the slow response time of the sensor.

The sensor exhibited a slow frequency drift that was attributed to changing moisture levels and occasional charge build up across the MEA. Commercially available humidity sensors were found to be too slow to monitor the real-time humidity in the sensor at the desired breathing rates. As a means of passive control, the addition of a desiccant was attempted to reduce or eliminate the effects of respiratory humidity. The molecular sieve 3A was selected as a humidity filter since its pore size allows the selective sorption of humidity while permitting flow of O_2 [63]. The volume of the filter was chosen to be approximately $10cm^3$. A higher volume provides a longer filter life-time but higher resistance to flow. The desiccant was shown to reduce much of the drift in the sensor. However, the humidity filter deteriorated quickly and lost efficiency after all the molecular sieve cavities had been filed. Since 100% efficiency loss occurred within 100 breath cycles, the addition of a molecular sieve desiccant was determined not to be a viable solution to the humidity issue.

As seen from the data sets shown in Figure 4.4 and Figure 4.5, signal processing was required in order to match the true oxygen concentration as measured by the MedGraphics gas analyzer. A high pass filter was shown to effectively remove the low frequency drift caused by humidity. However, the use of a high pass filter created a considerable transient decay and averaging effect over the data set which distorted the shape of the signal. As discussed in Chapter 1, not only the end tidal O_2 levels are important for medical diagnostics and monitoring. In addition, the shape of the respiratory profile is considered to be very important information for medical prognostics. Thus, retaining the accuracy of the oxygen concentration over each breath profile was desired. An alternative signal processing method designed to retain the exhaled oxygen profile is discussed in Chapter 5.

4.3 Conclusions

The fabrication of the membrane electrode assemblies was outsourced to the Fuel Cell industry. This resulted in both cost savings and an improved and more consistent product. New casing was designed to facilitate respiratory gas exchange analysis.

The response of the PEMFC-based sensor to changes in oxygen concentration was observed. The effect of humidity was studied. The absence of humidity resulted in a slow drift in the sensor output. In contrast, there was no drift under constant humidity conditions.

The response of the PEMFC-based sensor to expired breath was compared to test data taken with a MedGraphics Cardiopulmonary Exercise System. The response did not deteriorate over multiple tests as was seen with the sputtered MEAs in the previous chapter. The magnitude of oxygen response was on the order of 10-20mV per percent change in oxygen concentration. The 95% response time of the sensor was approximately 1-3 seconds. It was shown that signal processing techniques were required to measure respiratory exchange oxygen with the new sensor.

CHAPTER 5 DIGITAL SIGNAL (POST) PROCESSING

5.1 Introduction

As concluded in the previous chapter, the developed oxygen sensor exhibited several unwanted characteristics which accompanied the desired oxygen response. These unwanted characteristics include signal drift, variable or slow response times and signal noise. Once the sensor response was stabilized, only then could the signal be calibrated to represent the actual oxygen concentration.

The unwanted low frequency drift in the sensor was shown to be the result of fluctuating humidity levels at the sensing electrode. For breath-by-breath respiratory gas analysis, controlling the relative humidity at the sensor proved to be very difficult. In addition, commercially available humidity sensors could not measure the rapid and highly variable humidity levels within in the sensor. This drift needed to be removed or accounted for before the sensor could be calibrated.

A second unwanted characteristic in the sensor signal was the variable response time. Several factors were suspected to influence the response time. The limiting factor was the diffusion of oxygen through the carbon cloth gas diffusion layer. The gas diffusion rate was in turn a function of the relative humidity, pressure and flow rate of gas at the sensing electrode. Furthermore, stagnant gas remaining at the sensing electrode continued to react as it mixed with incoming gas. The cross flow channel and inspired breath from the patient helped to reduce (but not eliminate) this effect. The 95% response time of the sensor was shown to be 1-3 seconds for expired breath and typically 3-5 seconds to return in the absence of breath. This response time resulted in attenuated oxygen concentration measurements at higher respiratory rates which commonly occur during exercise or hyperventilation.

Low level signal noise was observed in the sensor. Since the typical response to expired breath was on the order of 0.01V-0.1V, the signal noise needed to be kept comparatively minute. Sources of signal noise included the power supply, measurement

circuit and data acquisition system. Fortunately, the signal noise was measured to be at higher frequencies than typical breathing rates.

The filters and algorithms discussed in this chapter were designed and implemented using Mathworks Matrix Laboratory (Matlab) numerical computing software.

5.2 Low Frequency Drift Correction

5.2.1 Constant Background Assumption

In order to filter out unwanted signal drift without removing the desired response, one must be able to differentiate between the desired and undesired changes in the sensor output. A high pass filter was shown to remove unwanted low frequency content but also introduce several undesired affects. These included slow transient decays, signal distortion (due to inherent 'averaging' effect) and a loss of signal bias.

During respiratory oxygen exchange, the concentration level of oxygen across the sensor drops from an ambient room level (usually 20.8%-20.9% O_2) to a lower concentration (typically 12%-20% O_2). This difference is caused by oxygen consumption which occurs in the lungs, converting oxygen gas into carbon dioxide. Under sensing conditions in which a patient has access to the ambient background air (e.g. is not re-breathing), the O_2 respiration profile has been shown to return to the background concentration between consecutive respiration cycles (expire, inspire). Therefore, assuming unimpeded access to the ambient room air, the concentration of oxygen at the start of each expired breath would be equal to the ambient O_2 concentration. This assumption is further supported by the open channel sensor design introduced in Chapter 6. Even in a small room without ventilation, the ambient background O_2 level remains relatively static compared to expired breath levels. This fundamental idea is the basis behind the post-processing algorithm.

5.2.2 Attenuating High Frequency Noise

To simplify the problem, the oxygen concentration during respiration can be approximated as a sinusoid where the period between consecutive peaks corresponds to one breath cycle. A breath cycle is defined as one full period of the sinusoid between consecutive peaks, staring at the beginning of each exhaled breath. The oxygen concentration of each peak is equal to the oxygen concentration of the background air. These concepts are illustrated in Figure 5.1.

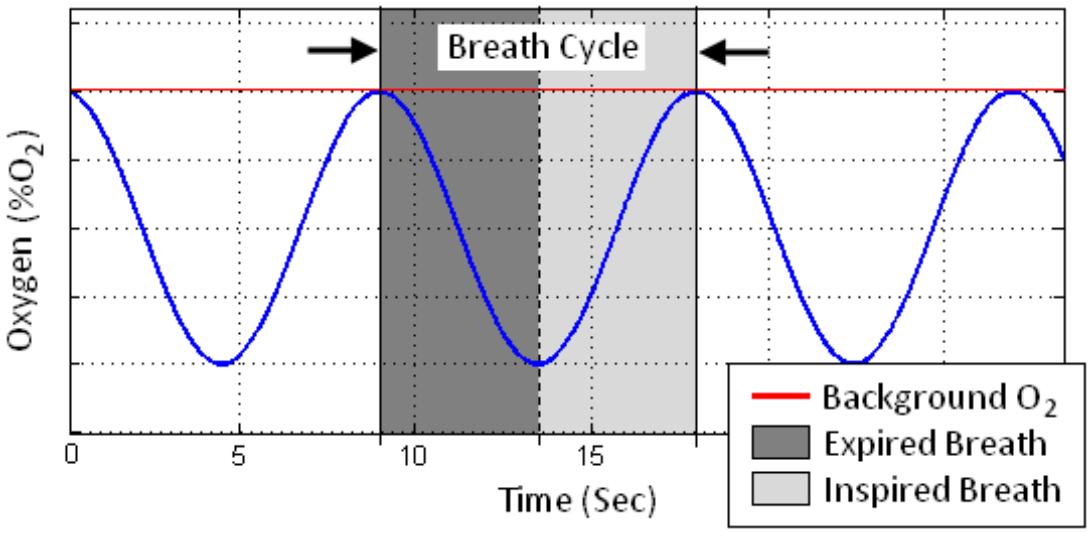

Figure 5.1: Sinusoidal model of respiration. Sinusoidal approximation of oxygen concentration during regular respiration, illustrating one complete breath cycle and the constant background oxygen assumption.

The addition of time varying humidity creates the low frequency drift in the measured signal. The measurement circuit results in the high frequency noise content. The resultant sinusoidal signal is shown in Figure 5.2.

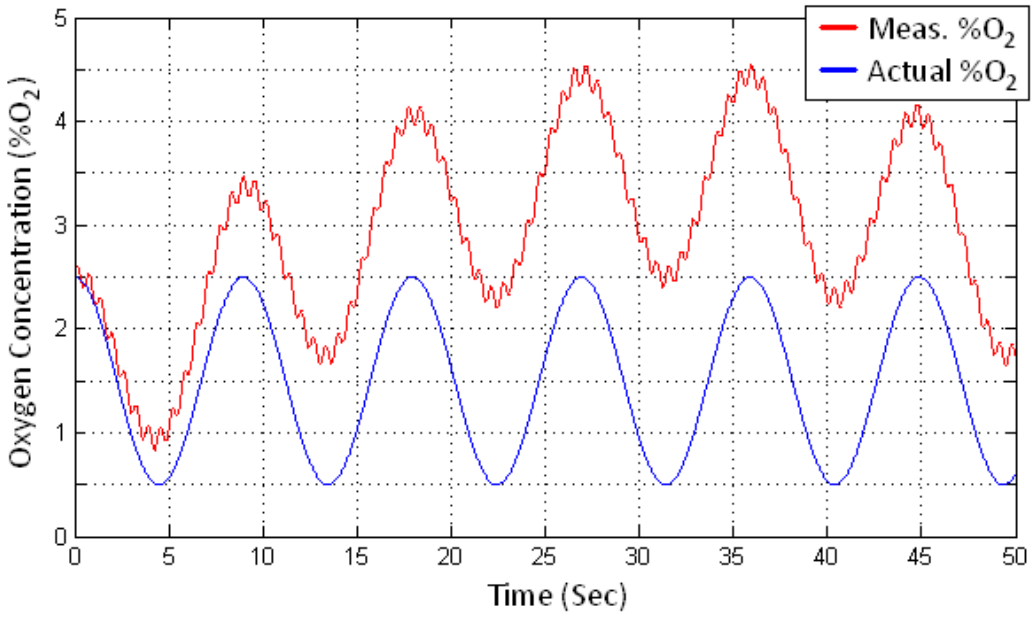

Figure 5.2: Example of typical signal noise. Simulation of oxygen concentration during respiration using a sinusoidal approximation. The measured signal was approximated as $y_m = Acos\ \omega t\ + bias + Bsin\ \omega_1 t\ + Csin\ \omega_2 t$, where ω_1 and ω_2 are the frequencies of the high and low frequency components. The actual signal was approximated as $y_a = Acos\ \omega t\ + bias$.

The data was first filtered to reduce noise and other unwanted high frequency content using a 2nd order lowpass digital Butterworth filter. The cutoff frequency of the filter was carefully selected to limit the attenuation of the desired response. The resulting filtered signal is illustrated in Figure 5.3.

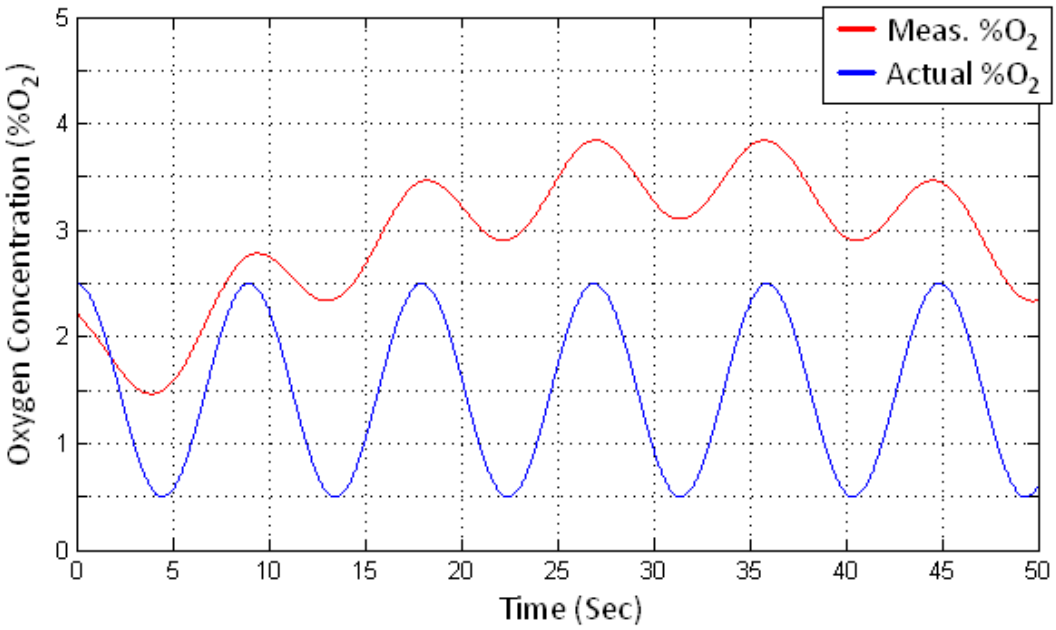

Figure 5.3: The measured sensor signal after lowpass filtering. As expected, the 2^{nd} order Butterworth filter resulted in some unwanted attenuation.

5.2.3 Breath Detection Algorithm

Once the unwanted noise is removed from the signal, the real challenge is to remove the low frequency drift without the distorting effects of highpass filtering. This first step to accomplishing this goal was to detect the breathing patterns in the signal. Specifically, the start and duration of each expired breath. Fortunately, the start of each breath corresponds with a peak in the raw sensor data and is therefore fairly easy to detect.

The start and duration of each breath are determined using a breath detection algorithm. The algorithm compares multiple consecutive data points to create the logic array shown in Figure 5.4. A 'Low' (0) signal indicates an inhale or no breath. A 'high' (1) signal corresponds to exhaling of breath onto the sensor. The algorithm simultaneously implements a counter to measure the length of each expired breath. A counted duration is then assigned to each detected breath and can be plotted for analysis as shown with real test data in Figure 5.4.

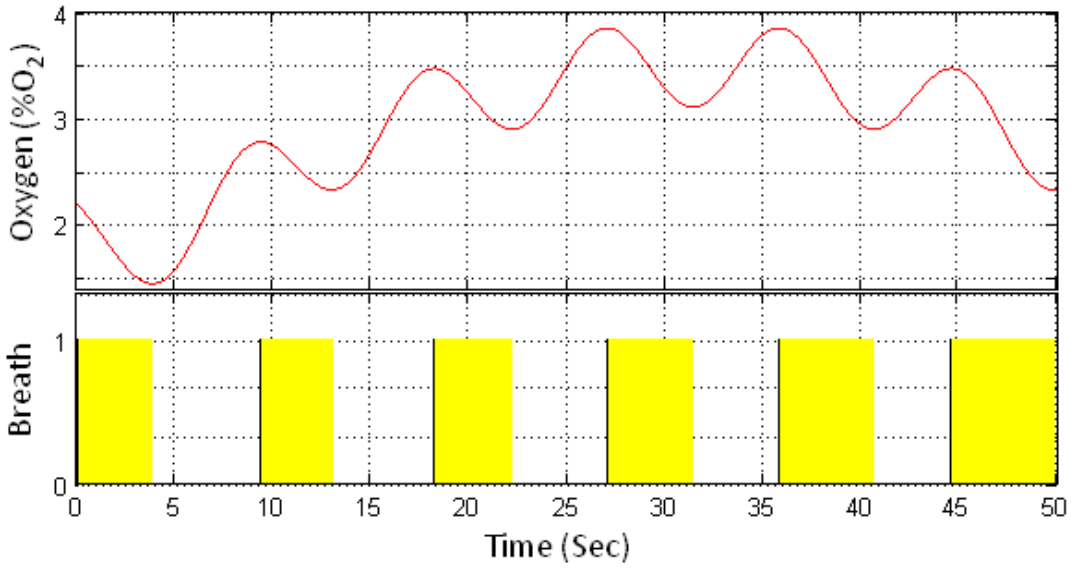

Figure 5.4: Output from the breath detection algorithm. ***Top).*** Sinusoidal approximation of typical sensor output. ***Bottom).*** The corresponding output from the breath detection algorithm.

The basic idea behind the breath detection algorithm works as follows:

$$\Delta = data\ i\ - data\ i-1$$

$$if\ \Delta \leq 0,\ \ set\ \boldsymbol{high}\ until\ \Delta > 0$$

$$(count\ exhale\ duration)$$

$$else\ \boldsymbol{low}$$

Included in the breath detection algorithm are a series of checks designed to distinguish expired breath from other fluctuations which may occur in the data - such as noise or drift. The first breath verification is a user defined threshold value for the minimum expiration time. This threshold time helps to prevent signal noise from being mistaken as respiration. A second verification observes the slope of the signal during an

anticipated expiration to distinguish typical breathing patterns from slow frequency drift. More advanced versions of the breath detection algorithm also include a correction check which takes into consideration data from the flow meter. The addition of a flow meter to the oxygen sensor is discussed in Chapter 6.

5.2.4 Slope Correction Algorithm

Once the start of each expired breath is precisely known, these data points can be adjusted to match the ambient background concentration according to the constant background assumption made in Section 5.2.1. The data between each starting peak is also adjusted using the slope between subsequent peaks. This method effectively removes unwanted low frequency drift while maintaining the shape of the original signal.

The start of the i^{th} breath cycle (P_i) corresponds to the i^{th} peak in the data and is determined from the breath detection algorithm. The slope correction algorithm first calculates the slope between the start of each sequential breath cycle or equivalently, the slope between each peak. The signal data between peaks is adjusted using this slope. The slope correction algorithm is illustrated below in Figure 5.5.

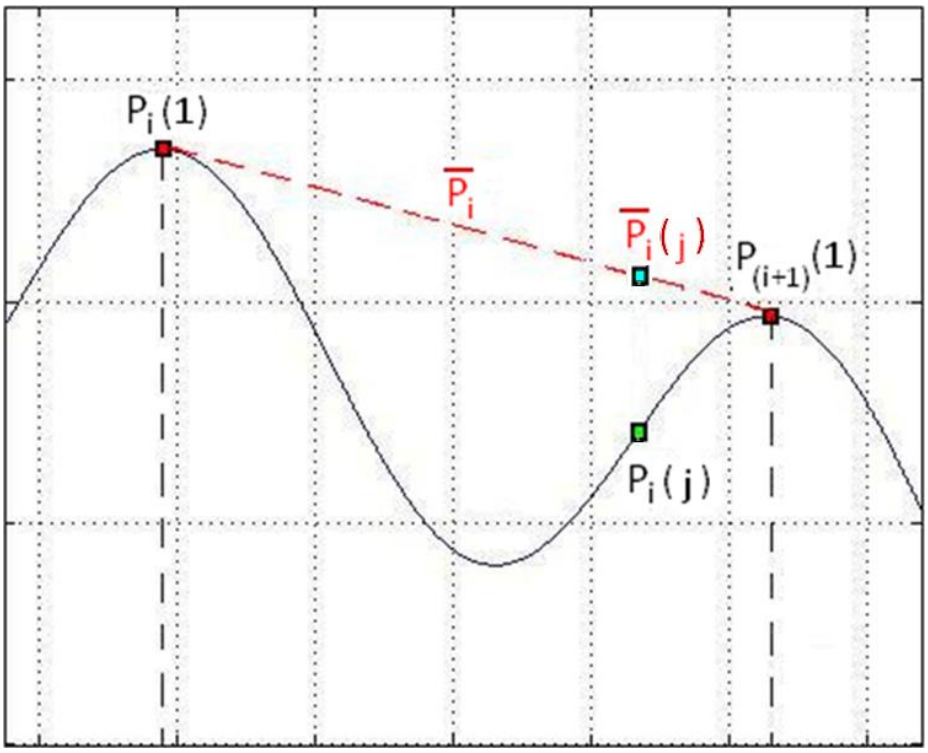

Figure 5.5: Illustration of the slope correction algorithm. Measured data point $P_{i(j)}$ is corrected using the corresponding value $P_{i(j)}$ on the line connecting the adjacent peaks in the breath profile.

The i^{th} breath cycle consists of n data points. The size of n is determined by the length of the breath cycle and the sample rate. The Cartesian coordinates of the first data point in the i^{th} breath cycle are denoted:

$$P_i(1) = \ t\ P_i(1)\ , y\ P_{\ i}\ (1)$$

Similarly, the coordinates of the j^{th} data point in the i^{th} breath cycle are denoted:

$$P_i\ j\ \ =\ \ t\ \ P_i(j)\ , y\ \ P_i(j)\quad\ for\ j = 2\,..\,n$$

In the slope correction algorithm, a slope value is assigned to each data point. The slope is the same for each of the n-data points that make up a single breath cycle. The slope is simply the ratio of the change in O_2 concentration and the duration of the breath cycle. The assigned slope of the j^{th} data point in the i^{th} breath cycle is denoted:

$$slope\ P_i(j) = \frac{y\ P_i(1) - y\ P_{i-1}(1)}{t\ P_i(1) - t\ P_{(i-1)}(1)} \quad for\ j = 1..n$$

The amplitude of the signal is then corrected using the lines that connect the start and end points of each breath cycle. The corrected data becomes:

$$P_i\ j = t\ P_i(j)\ , A\ P_i\ (j) \quad for\ j = 1..n$$

where

$$A\ P_i(j) = y\ P_i\ j - slope\ P_i\ j * t\ P_i\ j - t\ P_i\ 1 - y\ P_i\ 1$$

Since the correction for each data point requires signal information which occurs at a later instant in time, the slope correction cannot take place in real time. Either a significant lag time or post-processing is required to complete the algorithm.

A plot of the original data after lowpass filtering and slope correction is shown below in Figure 5.6. Note that the start of each breath cycle has been normalized to zero.

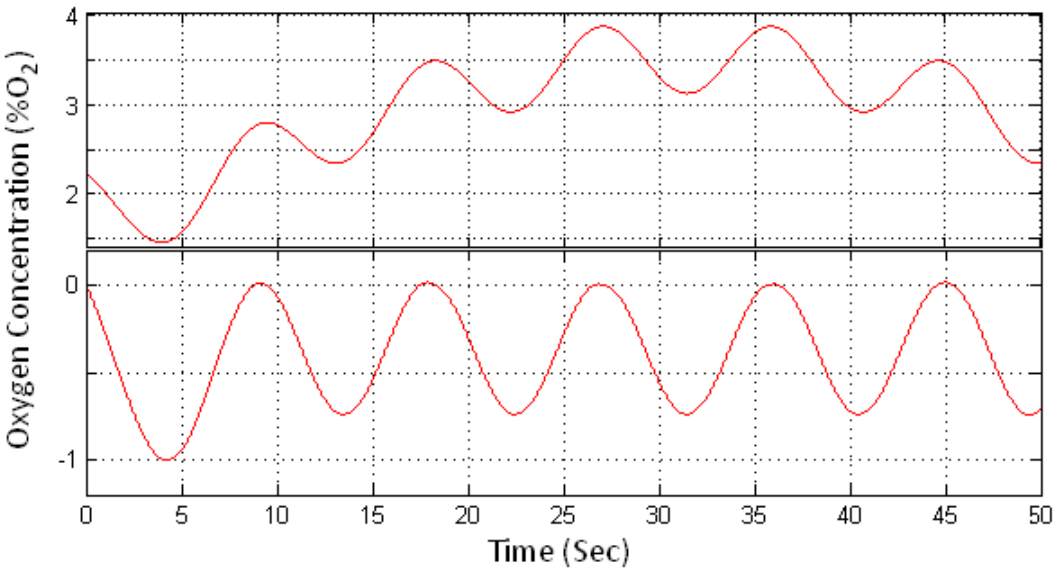

Figure 5.6: Sensor signal before and after drift correction. ***Top).*** Sinusoidal approximation of typical sensor output, ***Bottom).*** The sensor output after passing through the slope correction algorithm.

Once the drift has been removed, the signal from the oxygen sensor is readily calibrated to match to the true oxygen concentration. First, a gain value is applied to match the scale of the true oxygen signal. An offset value is then added to shift the signal to the desired concentration. Typically, the offset value is equal to the oxygen concentration of the background air. The calibration is applied to each data point as:

$$A\ \ P_i(j)\ \ = Gain * A\ \ P_i(j)\ \ + Offset$$

The resulting calibrated fit is shown in Figure 5.7 below.

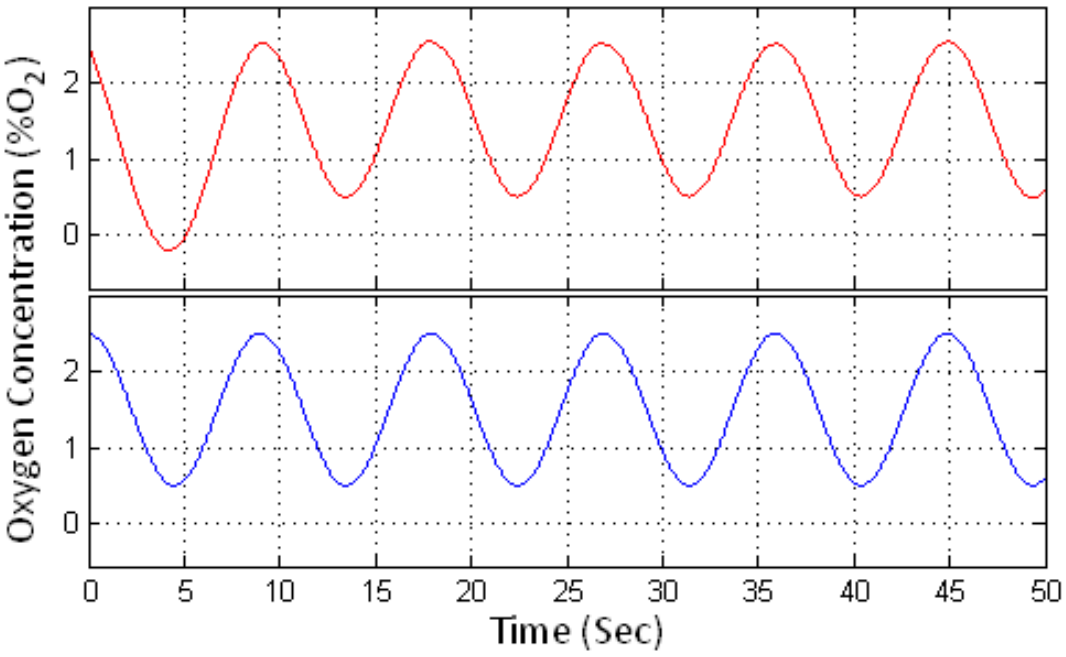

Figure 5.7: Drift corrected signal for sinusoidal respiration model. *Top).* The measured oxygen concentration after lowpass filtering, breath detection algorithm, slope correction algorithm and calibration, ***Bottom).*** Actual oxygen concentration.

5.2.5 Drift Correction Example

The individual steps of the signal processing for the oxygen sensor are shown below with real test data. The breath detection algorithm first identifies the respiration pattern in the raw signal. Each expired breath can then be presented as a function of its duration, as shown in Figure 5.8.

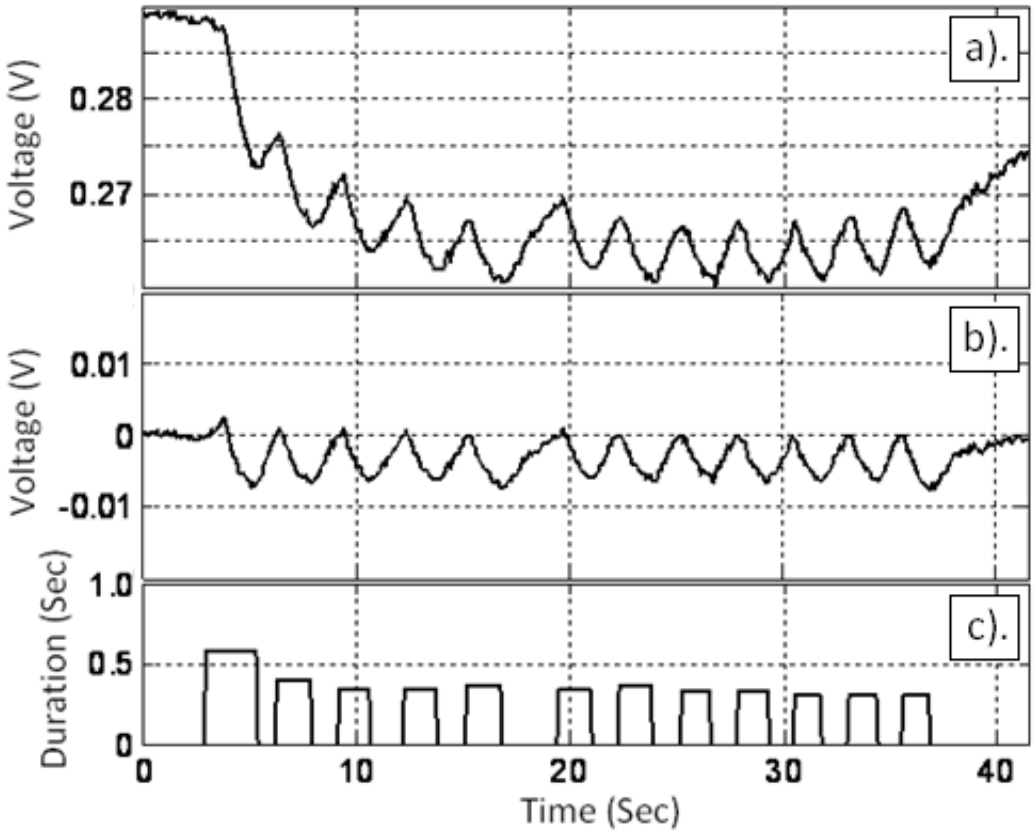

Figure 5.8: Breath detection and slope correction algorithm results. **a).** Typical raw signal from oxygen sensor, **b).** Output from slope correction algorithm, **c).** Output from breath detection algorithm.

5.3 Measuring Sensor Performance - Response Time and Accuracy

The performance of the sensor was quantified in terms of response time and accuracy.

Response times for exhaled breaths were measured from the baseline (start of exhaled breath) to 95% of the end tidal (minimum) O_2 value. Similarly, response times for inhaled breaths were measured from the start of inhaled breath (typically minimum O_2 value) to 95% of the baseline O_2 concentration. Thus, the 95% response times are reported throughout this paper.

The accuracy of the sensor was determined using the end tidal or minimum O_2 values obtained over each breath cycle. An error value (with units of $\%0_2$) was calculated over each breathing cycle. These error values were equal to the difference between the actual end tidal O_2 concentration (via the mass spectrometer) and the measured end tidal O_2 concentration (via the sensor). Accuracy of the sensor is thus reported in terms of the root mean square (RMS) and maximum end tidal error values over multiple tests (i.e. hundreds of breathing cycles).

5.4 Improving Sensor Response Time

5.4.1 Baseline Correction

The following data was collected with the untethered open-channel sensor discussed in the next chapter. Actual oxygen concentration was measured using a mass spectrometer. The mass spectrometer is reported to be accurate to ±0.1% O_2 concentration. A small pneumatic sampling tube was placed inside the new oxygen sensor during testing to draw sample air to the mass spectrometer.

Analysis of the test data indicates a slower than desired response for breath-by-breath measurement. However, with the unwanted drift removed from the signal, this slow response time can be addressed.

A baseline acceleration technique was used to decrease the response time of the sensor during inspiration. This is the time it takes for the sensor to return to the background concentration after reaching the end tidal O_2 concentration. According to our assumption, the concentration over each inspired breath is equal to the ambient background oxygen concentration. This was validated by the test data from the mass spectrometer, as shown in Figure 5.9.

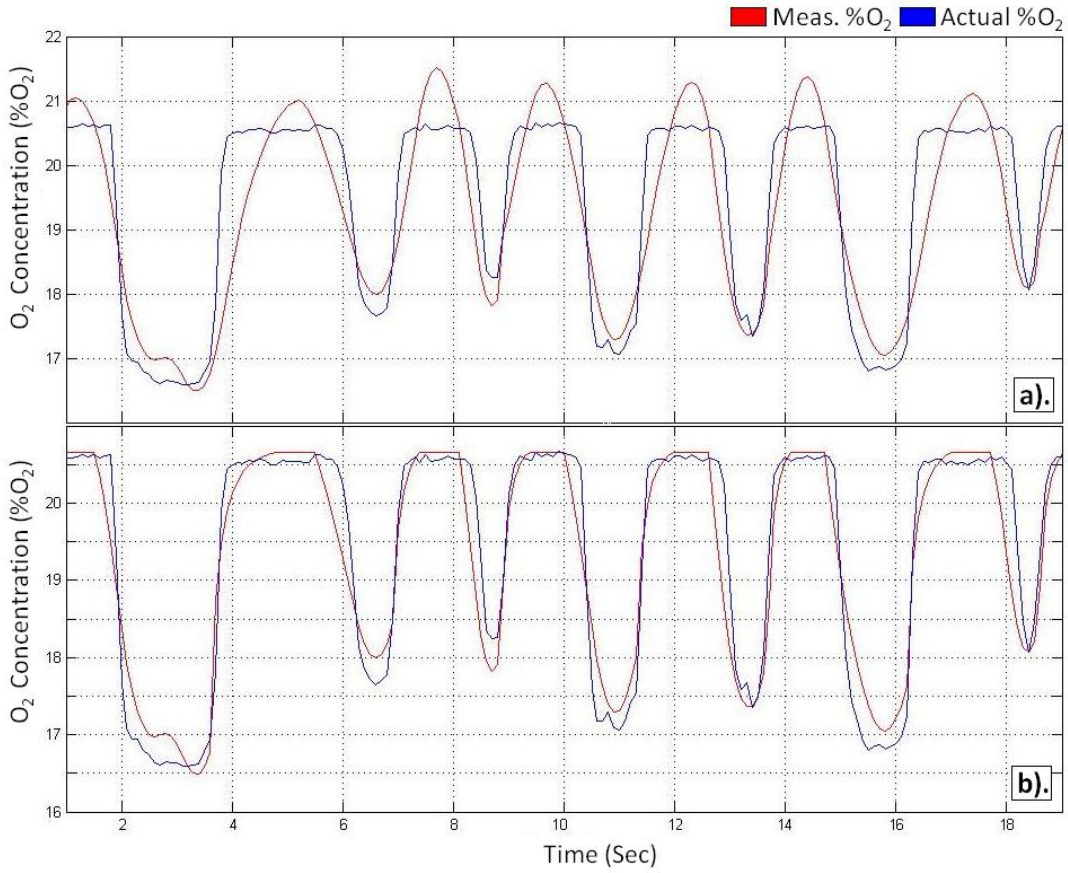

Figure 5.9: Test data illustrating the baseline correction algorithm. a). Data before baseline correction, **b).** Data after baseline correction algorithm.

During inspiration, the sensor response O_2 is first accelerated up to the background concentration using the exponential forcing function

$$O_2 = O_2 \cdot \ t_{insp}^{\ -\lambda}$$

where O_2 is the oxygen concentration and t_{insp} is an integer count from the start of the inspired breath.

The algorithm can be summarized as follows:

$$
\begin{aligned}
&if\ (breath = inhale)\\
&\qquad count++\\
&\qquad O_2 = O_2 \cdot\ count^{\ -\lambda}\\
&else\\
&\qquad count = 0
\end{aligned}
$$

To avoid overshooting the background concentration, a linear forcing function crops any values which exceed the concentration of the ambient air. This linear forcing function can be added to the above algorithm as follows:

$$
\begin{aligned}
&if\ (\%O_2 > \%\ ambient\ air)\\
&\qquad O_2 = O_2 \cdot \delta
\end{aligned}
$$

5.4.2 Model Inversion

The final issue to be addressed with signal processing is the response to high frequency respiration. With a time constant of roughly 1 to 2 seconds during expiration, the oxygen sensor is unable to keep up with rapid breathing patterns. This results in a mismatch between the reported O_2 concentration and actual O2 concentration, even after calibration.

Assuming a first order system model, the response of the oxygen sensor can be modeled as shown in Figure 5.10.

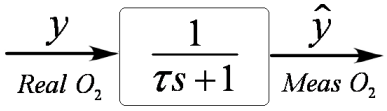

Figure 5.10: Oxygen sensor modeled as a first order linear system. The measured oxygen concentration is equal to the actual oxygen concentration multiplied by the system transfer function.

If the time constant of the sensor system is known or can be approximated, the actual oxygen concentration can be obtained by 'inverting' the system model. The actual concentration value, y, the measured concentration, y, and the time constant, τ, are thus related as follows:

$$y = y \cdot \frac{1}{\tau s + 1}$$

$$y = \tau s + 1 \cdot y$$

By solving the inverse Laplace transform and changing to discreet time, the expression for the actual oxygen concentration, based on a first order model of the sensor is as follows:

$$y\ t\ = y\ t\ + \tau \frac{dy(t)}{dt}$$

$$y\ n\ = y\ n\ + \tau\ \frac{y\ n\ - y(n-1)}{dt}$$

The model inversion technique was added to the other signal processing algorithms discussed in this chapter. The effectiveness of using model inversion on real data is shown in Figure 5.11. In Figure 5.11*a*, the oxygen sensor is accurate over the slower breathing pattern (0-10 seconds) but becomes less accurate during the faster breath pattern (15-25 seconds). In Figure 5.11b, the first order model inversion has been applied to the sensor with a time constant of 1.65 seconds. The result is a better correlation over the entire range of data which includes variable breathing rates.

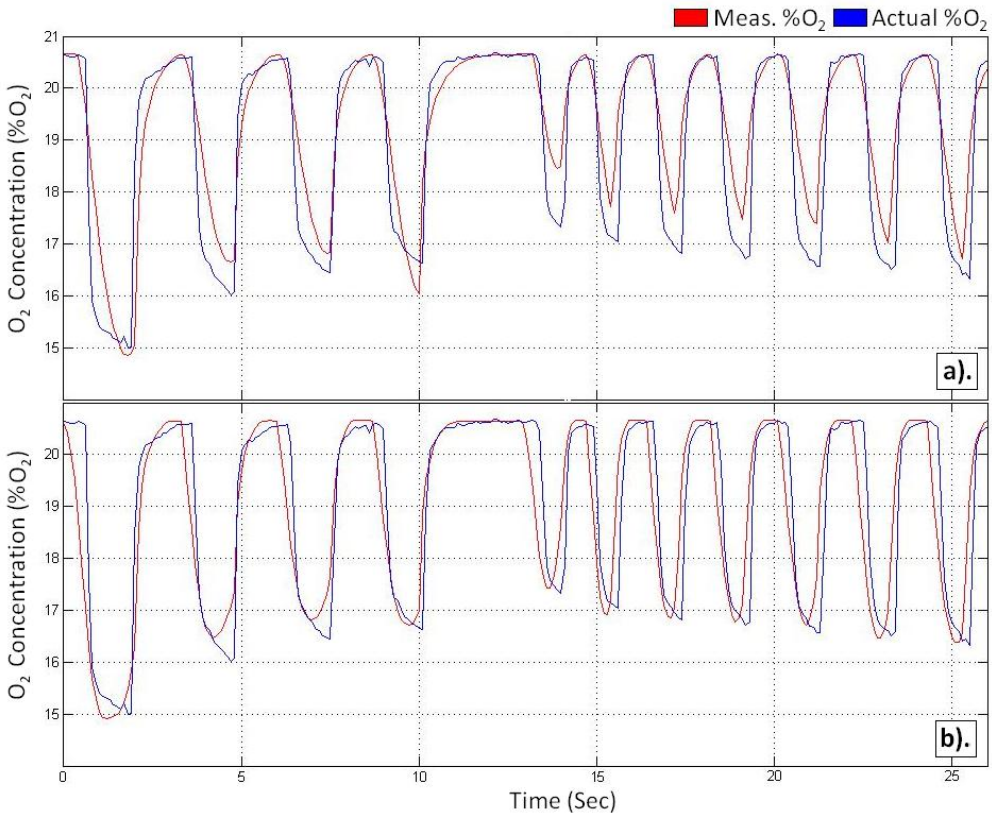

Figure 5.11: Test data implementing the model inversion technique. Example of model inversion technique to correct sensor response to rate-varying breathing patterns. Mass spectrometer used to present true oxygen concentration, **a).** before model inversion, **b).** after model inversion.

5.5 Conclusions

With the addition of the post processing techniques discussed in this chapter, the novel Nafion oxygen sensor performed very well. The low frequency drift was removed and the RMS error in end tidal oxygen concentration was measured to be ±0.2 $\%O_2$ over steady, resting respiration. During faster respiration (such as exercise) or varying respiration, the RMS error increased to roughly ±1 $\%O_2$. Similarly, the maximum sensor error increased from ±1 $\%O_2$ during steady respiration to approximately ±4% over largely varying breathing patterns. It was noted that during steady respiration, the concentration of respired O_2 varied from approximately 14-18 $\%O_2$. However, during largely varying and heavy, deep respiration this range increased, and concentrations from 9-19 $\%O_2$ were observed.

CHAPTER 6 PEMFC-Based Oxygen Sensor (2nd Generation)

6.1 Motivation for a New Design

While completing work on this project, a comparable electrochemical oxygen sensor was identified in the medical field and available from Teledyne Analytical Instruments, Inc. While no literature was found on this new OEM product, the Teledyne UFO-130 Oxygen Sensor was marketed as an "ultra fast oxygen sensor for respiratory analysis". Designed for side stream breath-by-breath monitoring applications, the sensor was also said to utilize signal processing techniques and micro-fuel cell technology. The Teledyne UFO-130 Ultra-Fast Oxygen Sensor is depicted below in Figure 6.1.

Figure 6.1: Teledyne UFO-130 Ultra-Fast Oxygen Sensor. **a).** Oxygen sensor, **b).** 2x2 inch PCB board.

Clearly, similar fabrication and control techniques to those described in this paper (so far) have been employed in the Teledyne sensor. To investigate this idea further, the Teledyne UFO sensor was purchased and tested in respiratory analysis. The sensor was available for $550, but still required a ±12 volt power supply, pneumatic sampling system, data acquisitions system and some additional wiring. It was shown to have a range of 1-100% O_2, an accuracy of ±1% O_2, and an impressive 10%-90% response time of around 150ms at a sufficient gas flow rate. However, this performance was contingent on conditions of constant temperature and pressure.

While the Teledyne sensor is much more convenient to use compared to bedside analyzers such as the mass spectrometer, it still requires a pneumatic sampling system, data acquisition system and +/- 12 volt power supply. These additional components attach directly to the sensor and therefore to the body of the patient. Hence, they are not ideal for use in ambulatory or home monitoring applications (such as sleep apnea). In these applications, a small untethered sensor unit that can be mounted at the mouth of the patient would be invaluable.

6.2 WIRELESS, UNTETHERED, OPEN-CHANNEL SENSOR

6.2.1 Open-Channel Design

The Nafion-based oxygen sensor was redesigned to improve its portability and offer some unique features to set it apart from the UFO-130 sensor from Teledyne. The main goal was to provide a breath-by-breath sensor which does not require a pneumatic sampling system. To the best of our knowledge, such a sensor does not exist on the market at this time.

In order to achieve untethered operation, the sensor structure (as discussed in Chapter 4) was completely redeveloped. The pneumatic sampling system was discarded and the multi-layered casing was replaced with a 1-inch open-channel design. The MEA was carefully rolled into a cylindrical shape and attached to the inside wall of the casing to

form the sensor. Non-conductive, water resistant tape was used to protect the exposed Nafion membrane and adhere the MEA to the casing. Copper tape was used to form the electrical connection between the measurement circuit and the MEA. The contoured MEA and open-channel sensor casing are shown below in Figure 6.2.

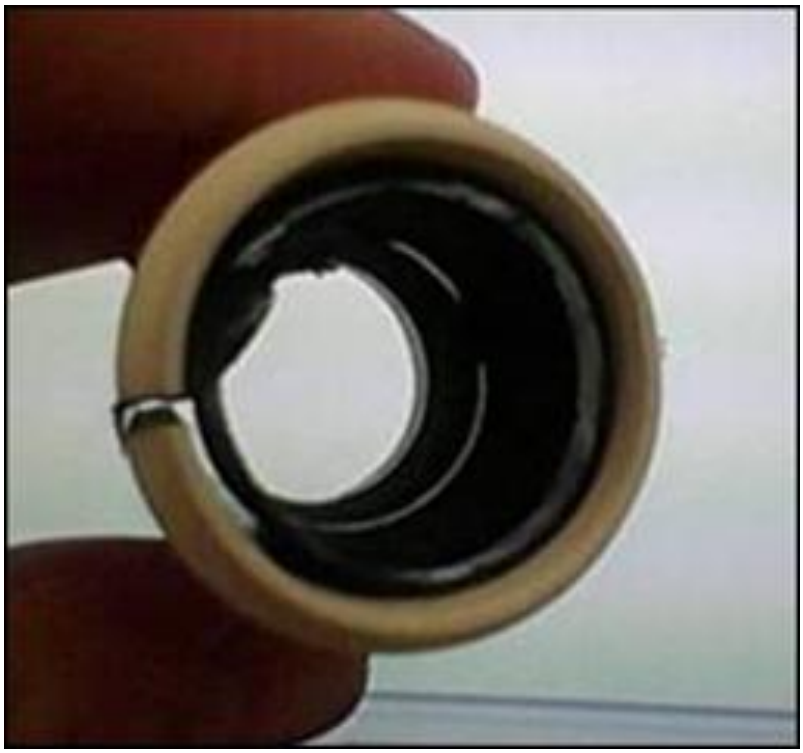

Figure 6.2: Open-channel sensor design. Membrane electrode assembly is rolled and then adhered inside the channel.

The new open-channel design offers several unique advantages over the previous design. First, the open channel allows for unobstructed, multi-directional flow across the sensing membrane. This is essential for the movement of breath and removal of stagnant air from the sensing membrane in the absence of a pneumatic sampling system. Second, the open-channel shape maximizes the area of the sensing membrane in contact with the sample gas.

In use, a mouthpiece is added to the front of the open-channel casing. The patient maintains a seal on the mouthpiece such that respiration is entirely through the sensor.

This set up effectively moves breath over the sensing membrane and removes the need for a pneumatic sampling system.

To increase sensitivity, a second membrane electrode assembly was added to the sensor in a series connection. This technique is commonly used in the fuel cell industry in which fuel cells are stacked together in series to increase electrical output. The output was shown to increase by 10-15% with two connected MEAs versus one large MEA of roughly the same size. The series MEA circuit required only a 0.25V input to reach the optimal sensitivity, resulting in very low power consumption compared to previous designs. The complete measurement circuit is shown in Figure 6.3.

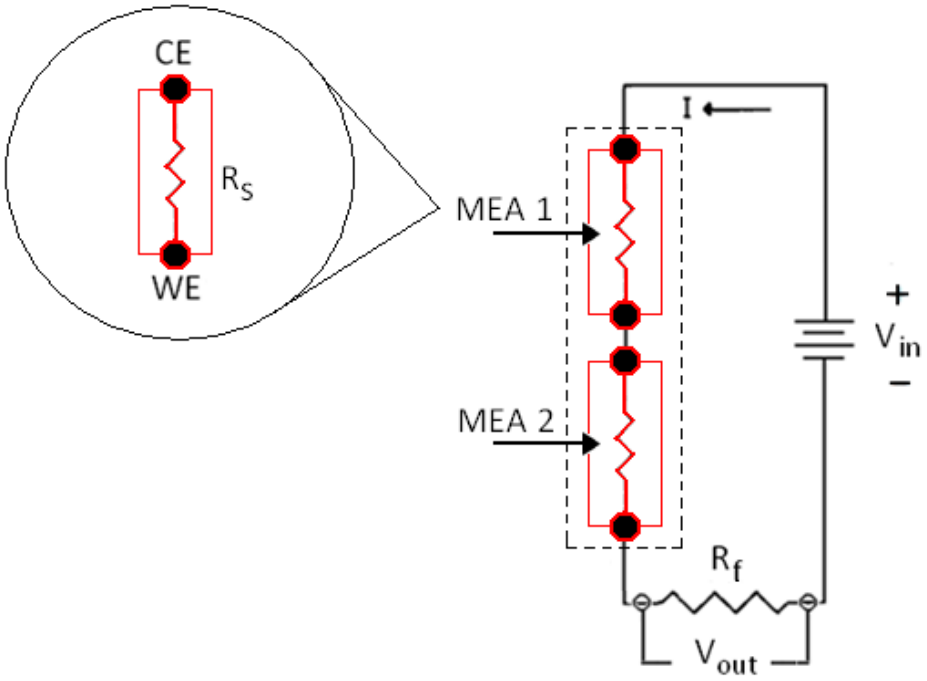

Figure 6.3: Second-generation sensing circuit. The two membrane electrode assemblies are connected in series.

6.2.2 Wireless Design

Wireless data transmission was achieved using an eZ430-RF2500 wireless development kit based on the ultra-low power MSP430 microcontroller from Texas Instruments. The development kit permitted acquisition of voltage signals from the sensor measurement circuit and wireless transfer to a receiving unit connected to a USB port of regular laptop. The wireless data transfer utilized the SimpliciTI protocol, operates at 2.4 GHz and provides telemetry distances up to 100 feet. The eZ430-RF2500 development kit is shown below in Figure 6.4.

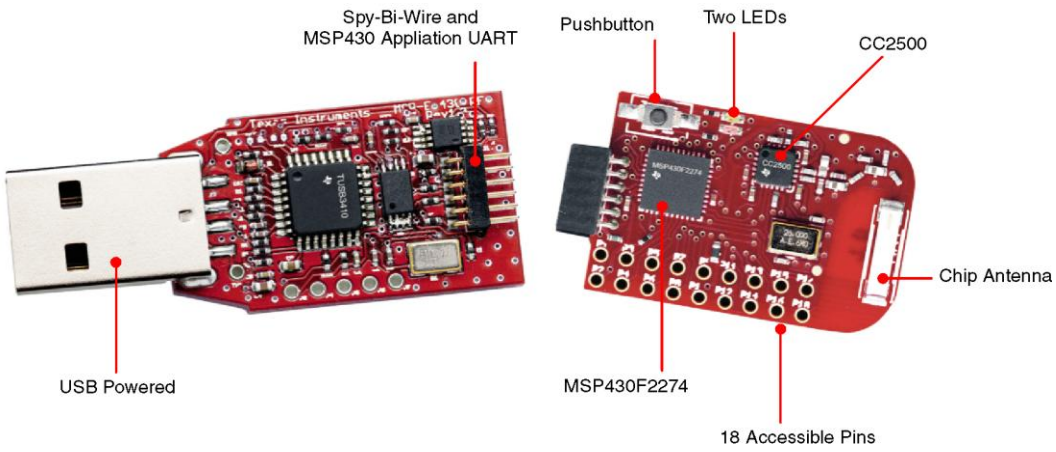

Figure 6.4: The eZ430-RF2500 wireless development tool kit.

A custom fabricated printed circuit board (PCB) was designed to achieve a smaller electronics package and to include the eZ430-RF2500 target board. The PCB circuit implemented a voltage divider and non-inverting amplifier in addition to the measurement circuit. A single 1.5 volt coin battery could supply enough power to the sensor for roughly one hour of wireless data transmission. The PCB, coin battery and RF target board are shown in Figure 6.5.

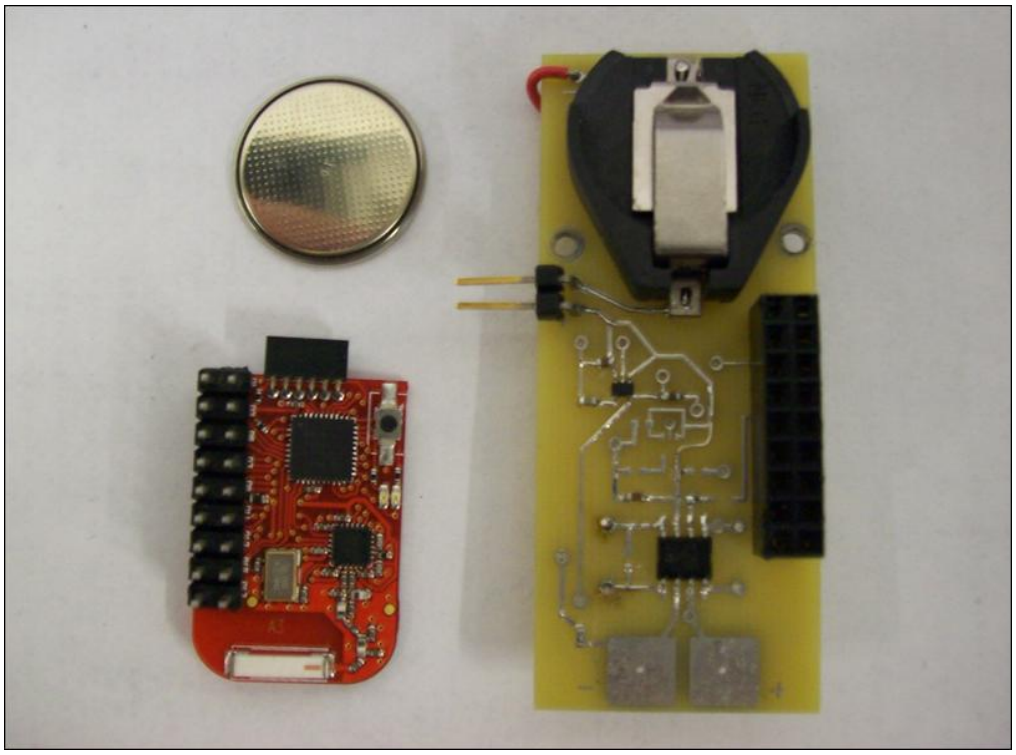

Figure 6.5: Electronic and wireless components. 1.5 volt coin battery, eZ430-RF2500 target board and printed circuit board (right).

The electronics package was mounted onto the open-channel sensor casing as shown in Figure 6.6. A small mouthpiece with a thin moisture barrier was later added to improve the interface between the sensor and the patient.

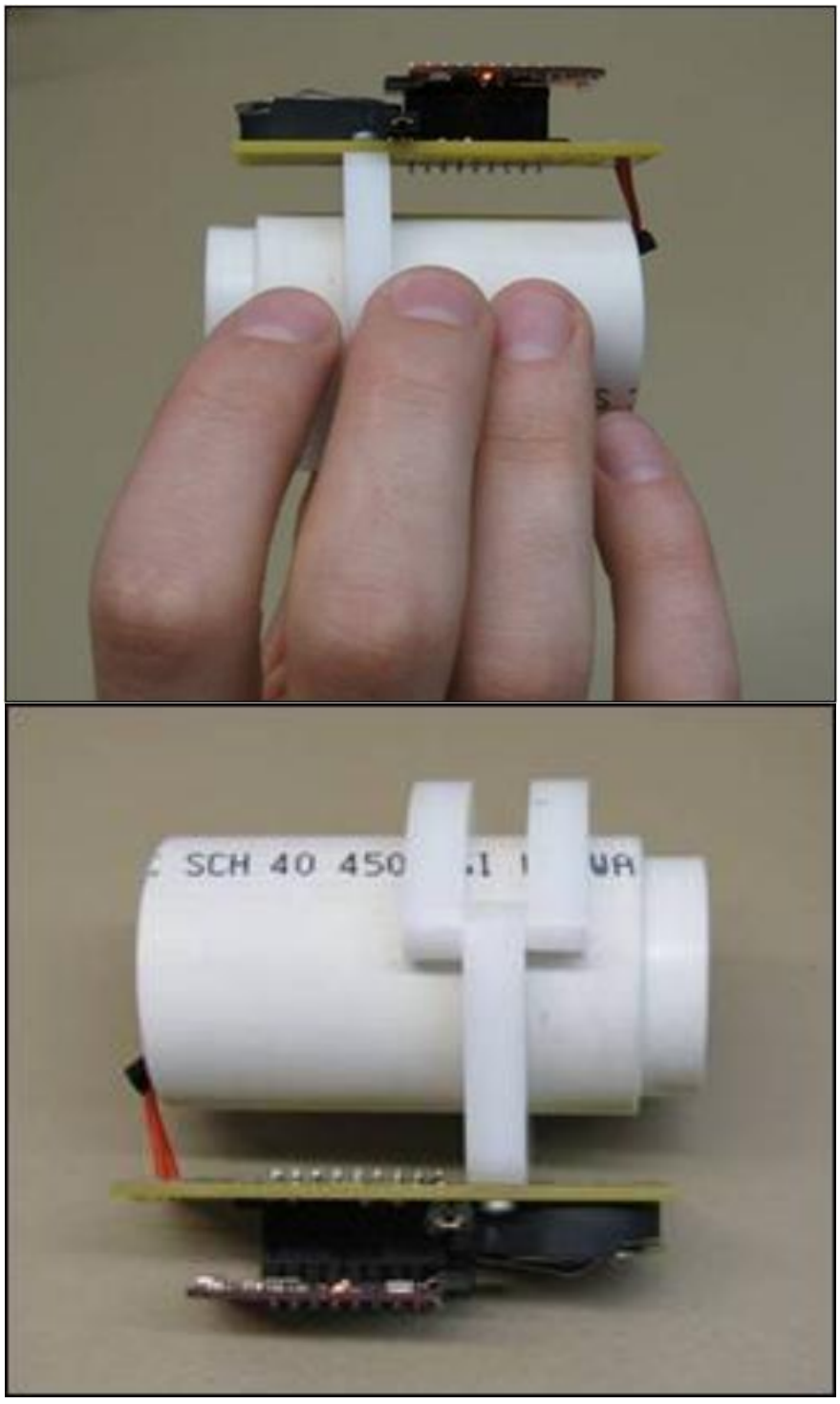

Figure 6.6: Second-generation oxygen sensor. Fully-assembled untethered, wireless sensor (mouthpiece not shown).

6.3 Results and Discussion

The oxygen response of the untethered open-channel oxygen sensor was once again tested at the Mayo Clinic in Rochester, MN. The actual (true) oxygen concentration was measured using a mass spectrometer in Dr. Bruce Johnson's research center. The mass spectrometer was reported to be accurate to ±0.1% O_2 concentration. A small pneumatic sampling tube was placed inside the new oxygen sensor during testing to draw sample air to the mass spectrometer.

Multiple data sets were collected during testing. The respiration rate, flow rate, and depth of breath (effectively the humidity and oxygen consumption) were varied to simulate each of the breathing patterns expected in sensing applications. For example, the sensor was tested in light, at-rest respiration as well as the fast, heavy breathing associated with hyperventilation. The patient's nose was plugged so that expiration and inspiration were entirely through the sensor channel.

A data set from the Mayo Clinic testing is presented below. A steady, at-rest breathing pattern was used. The data is presented as it passes through each step of post-processing.

Figure 6.7 shows the raw data taken from the sensor. Also plotted is the actual oxygen concentration as measured by the mass spectrometer.

Figure 6.8 depicts the crucial first step of the signal post-processing, the breath-detection algorithm. The breath-detection algorithm detects the start and duration of each breath cycle. This information is used to remove the unwanted drift in the signal.

Figure 6.9 shows the raw sensor data plotted with the same data after post processing. Post processing includes each of the techniques described in Chapter 5; breath detection, slope and baseline correction, model inversion and calibration.

Figure 6.10 illustrates a strong correlation between the processed sensor data and the true oxygen concentration. The oxygen concentration over steady breathing patterns was measured with an RMS error of ±0.2 $\%O_2$. It was observed that consistent breathing patterns yielded the most accurate results. Issues associated with largely varying test conditions are discussed in the following section.

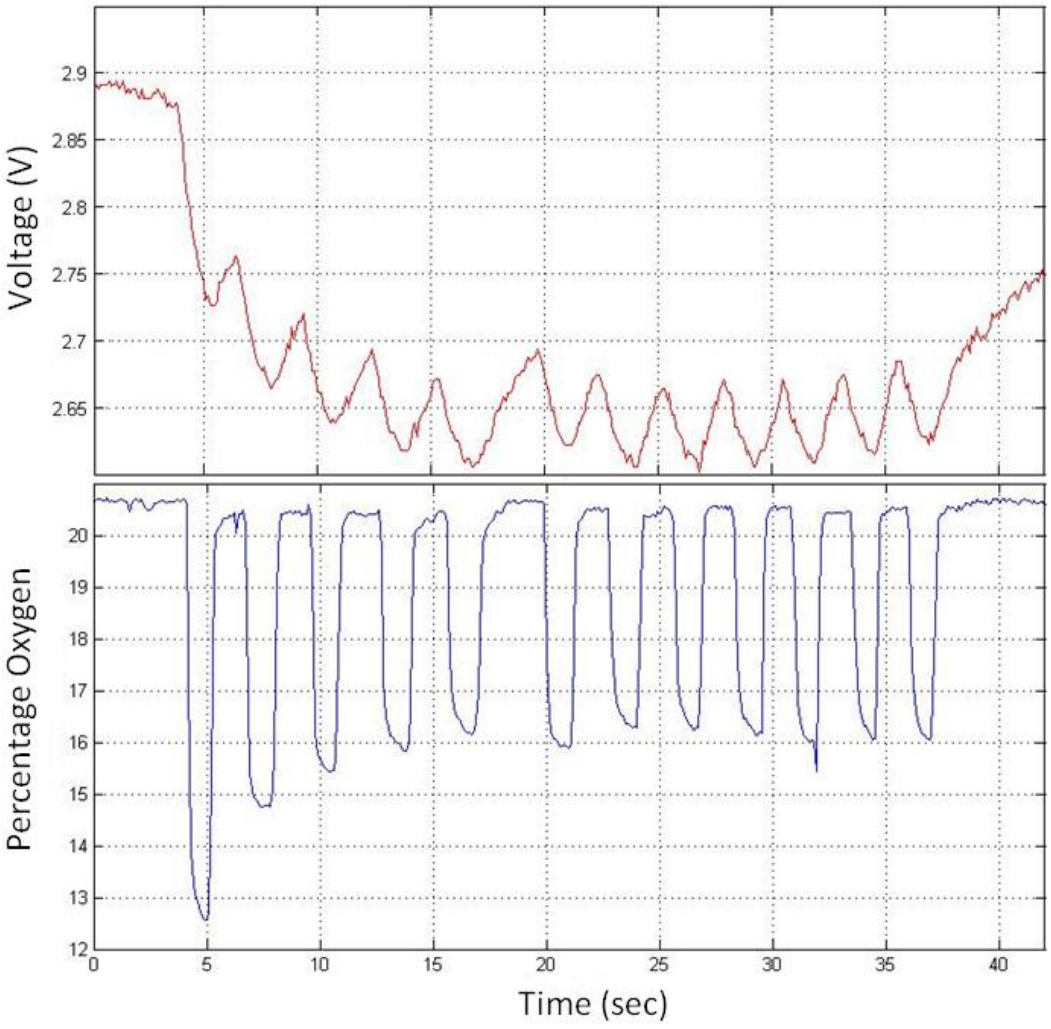

Figure 6.7: Oxygen sensor versus mass spectrometer. ***Top).*** Raw data from the untethered Nafion oxygen sensor, ***Bottom).*** Actual oxygen concentration as measured by the mass spectrometer.

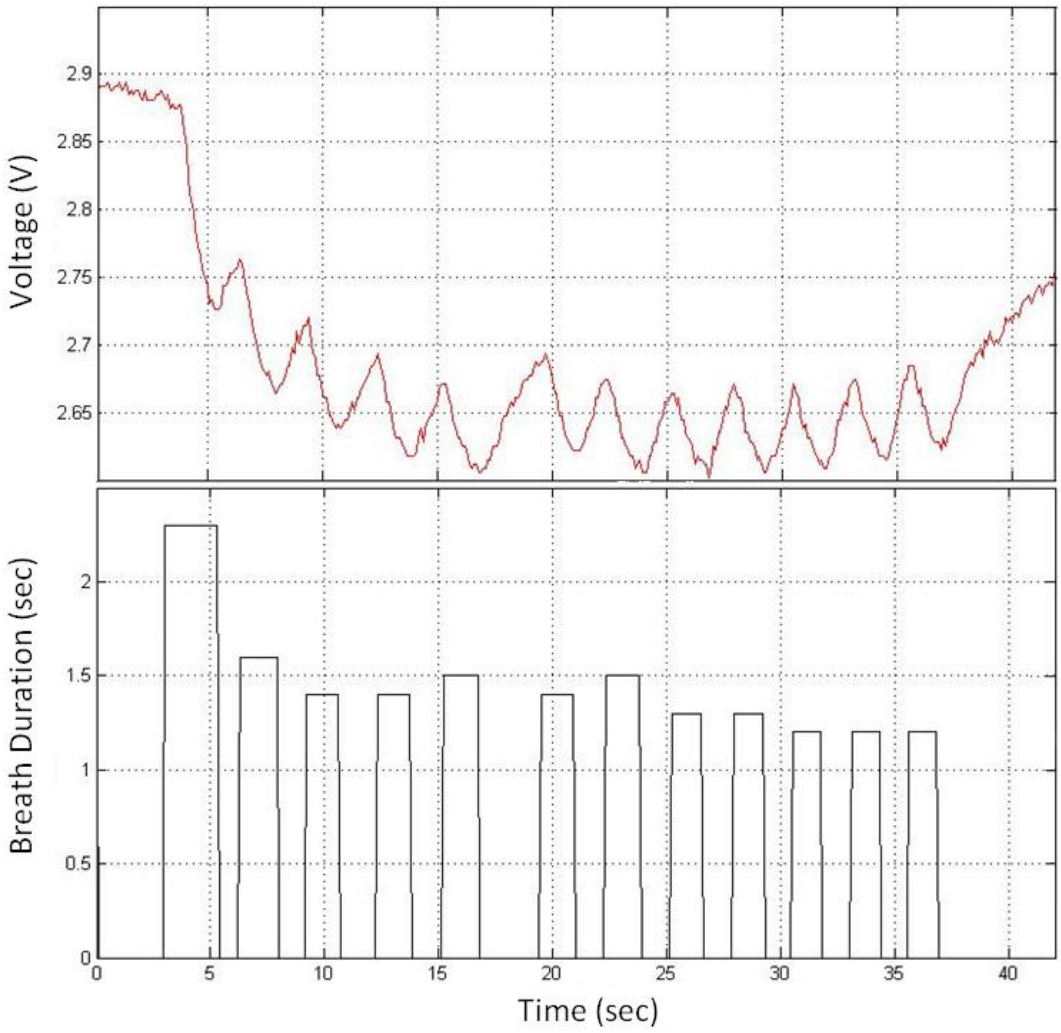

Figure 6.8: Raw data and output from breath detection algorithm. ***Top).*** Raw data from the untethered Nafion oxygen sensor. ***Bottom).*** Output from the breath detection algorithm. The breath detection is predominantly used with the slope correction to remove unwanted drift in the signal. However, it also provides a useful visual representation of the expired breathing pattern.

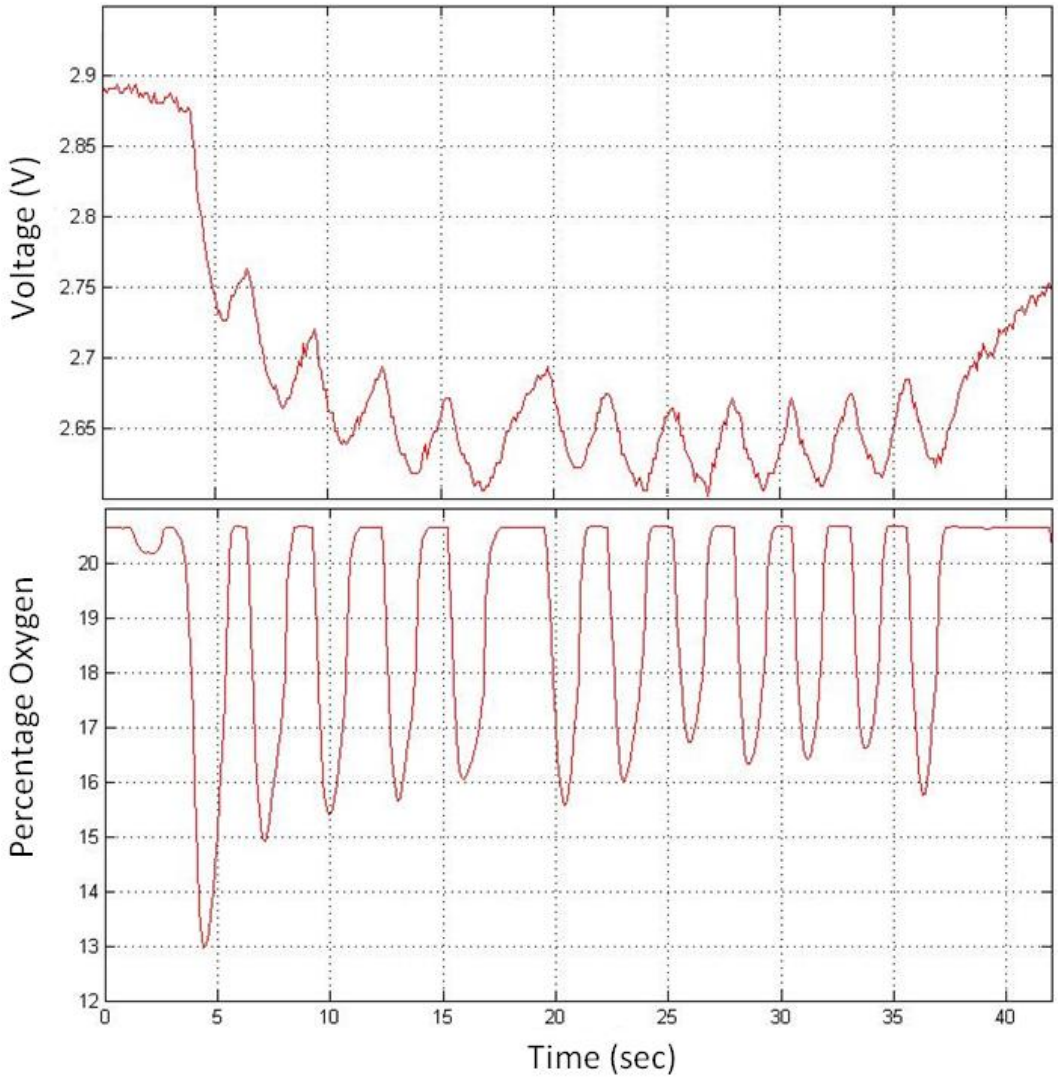

Figure 6.9: Raw sensor data versus post-processed data. ***Top).*** Raw data from the untethered Nafion oxygen sensor. ***Bottom).*** The same data set after post-processing is plotted for comparison.

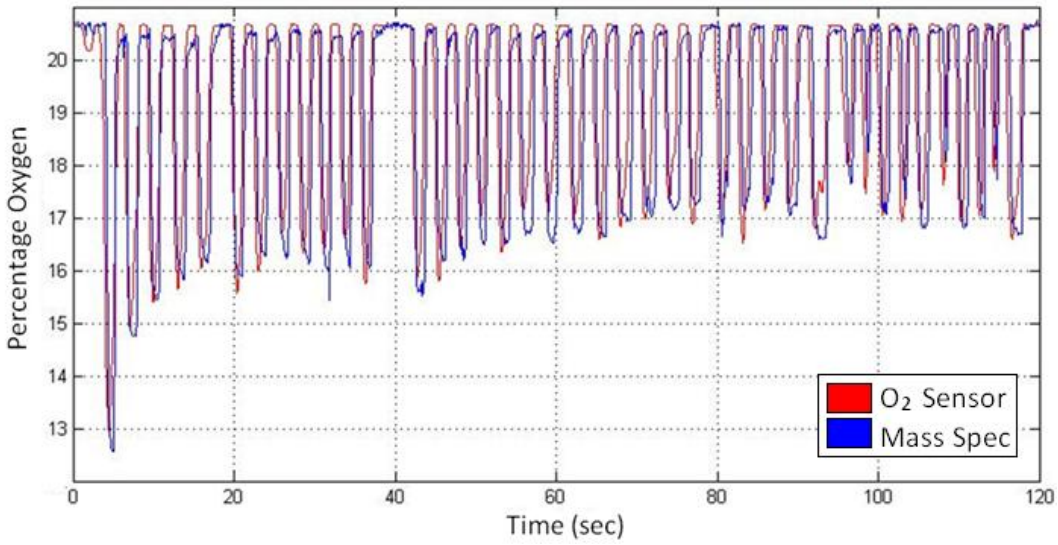

Figure 6.10: Test result with mass spectrometer. The sensor performance during a steady, at-rest breathing pattern. The sensor data is shown in red. The actual oxygen concentration is shown in blue. The two are plotted separately below.

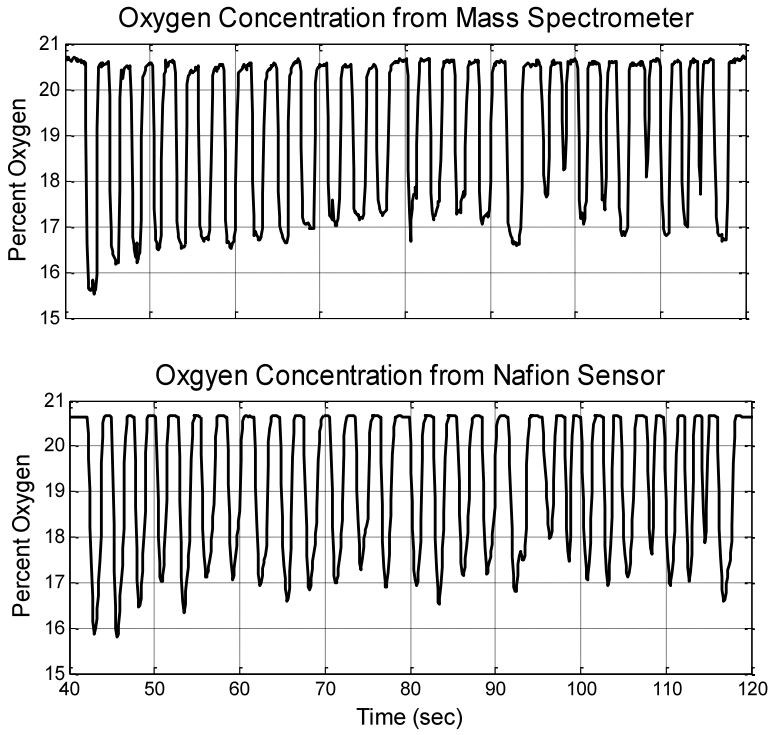

6.4 Flow Sensitivity and Flow Sensing

6.4.1 Flow Rate Dependence

While the sensor performed very well under steady breathing patterns, it demonstrated some flow dependence under extreme conditions. That is, under very low and high flow rates, the sensor performance deteriorated. In order to account for this apparent flow-dependence, the flow rate (or relative flow rate) through the sensor at any point in time was required. The typical range of flow rates during respiration varies from 0.1L/sec to 3L/sec.

A fan-flow meter was developed using a 12V DC CPU cooling fan available from Sunon Inc. The dimensions of the CPU cooling fan are 40X40X20mm which allowed for easy incorporation into the untethered, open-channel sensor design. The fan has a built in tachometer which provided a square output pulse. The frequency output was equal to twice the rotational frequency of the fan divided by the number of blades. A non-inverting amplifier and counter were incorporated into the measurement circuit to record the instantaneous angular frequency of the fan. The fan and the tachometer output of a 4-blade fan are shown in Figure 6.11.

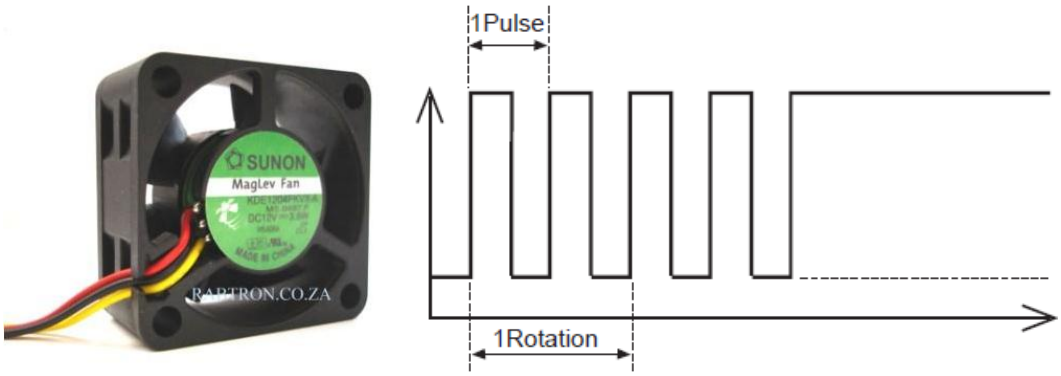

Figure 6.11: Sunon MagLev CPU cooling fan. Fan has 12V DC with 4 blades and sample tachometer output. Model KDE1204PKVX-A.

The fan was attached to the open end of the open-channel sensor so that the airflow through the channel was entirely directed through the fan. The fan was given a low constant voltage throughout the sensing operation and directed so that it (gently) pulled air through the sensor. Thus, inhaling into the sensor resulted in an opposing flow which caused the fan to slow down. This was recorded as a decrease in fan frequency. Similarly, exhaling through the sensor resulted in additional flow in the direction of the fan. Thus, exhaling through the sensor caused the fan to speed up which was observed as an increase in fan frequency.

The fan flow meter was tested against a flow meter at the mayo clinic. The steady fan frequency was set to 120Hz. At this fan rate, it was easy to slow the fan down via inspiration without any risk of stalling the blades. However, in order to increase the fan speed from 120Hz, it was shown that a significant hardness of expired breath was required. Lowering the fan speed to 60Hz resulted in a more balanced approached, and still allowed the fan to operate safely above the threshold frequency where heavy inhalation could stop the rotation.

Sample data from the flow fan meter testing is shown below in Figure 6.12. Positive flow direction was defined as the direction of expired respiration through the sensor channel. The fan demonstrated exceptional performance during inspired respiration in which the direction of breath caused the fan to slow down (i.e. fan frequencies below 120Hz). However, the high fan speed made it impossible to detect low expired flow rates. A lower frequency fan speed was later shown to solve this issue.

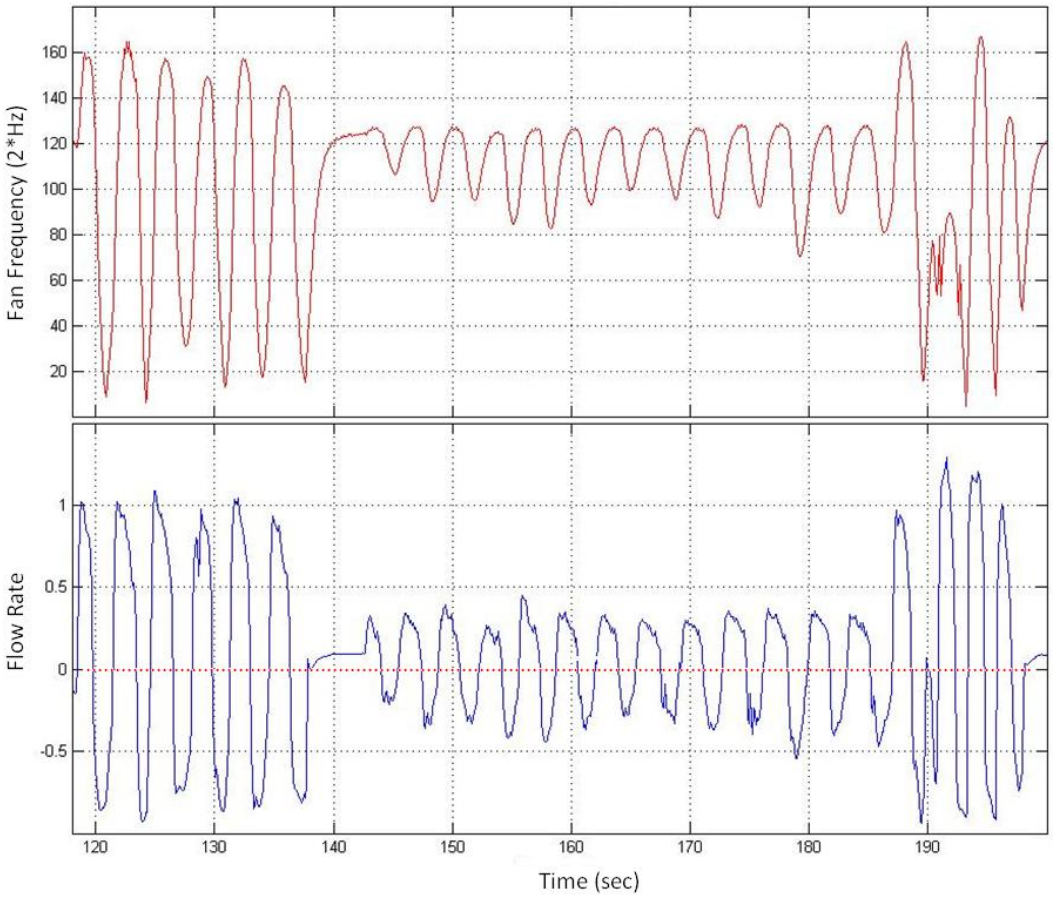

Figure 6.12: Flow rate from fan-flow meter versus Mayo flow meter. ***Top).*** Respiratory flow rate as interpreted by the frequency of the fan flow meter. The steady state frequency of the fan was 120Hz. Inspiration caused the fan to slow down, while expiration resulted in an increase in fan speed. ***Bottom).*** Actual flow rate in L/min as measured by flow meter.

6.4.2 Flow-Correction Algorithm

With an accurate measure of the relative flow rate through the channel (in addition to the oxygen measurement), the flow-dependence of the sensor can be addressed. A flow-correction algorithm was developed to correct for O_2 measurement inaccuracy occurring at relatively high and low flow rates.

The flow-correction algorithm worked in two simple steps. First, a “flow frequency” value was assigned to the expired and inspired portions of each breath cycle. These flow frequencies were equal to the maximum fan frequencies measured over each breath. The oxygen level of breaths which exceeded threshold frequencies were attenuated based on a series of gain values. The amount of attenuation for high flow rates was determined using empirical test data.

The performance of the flow-correction algorithm was evaluated using flow rate measurements from the flow meter at the Mayo clinic. Unfortunately this is the only accurate flow data captured during testing with both the developed oxygen sensor and the mass spectrometer. Figure 6.13 shows the flow rate data from the Mayo flow rate sensor and the output of the flow-correction algorithm which is used to account for flow dependence of the oxygen sensor. The result of applying the flow-correction algorithm is depicted in Figure 6.14.

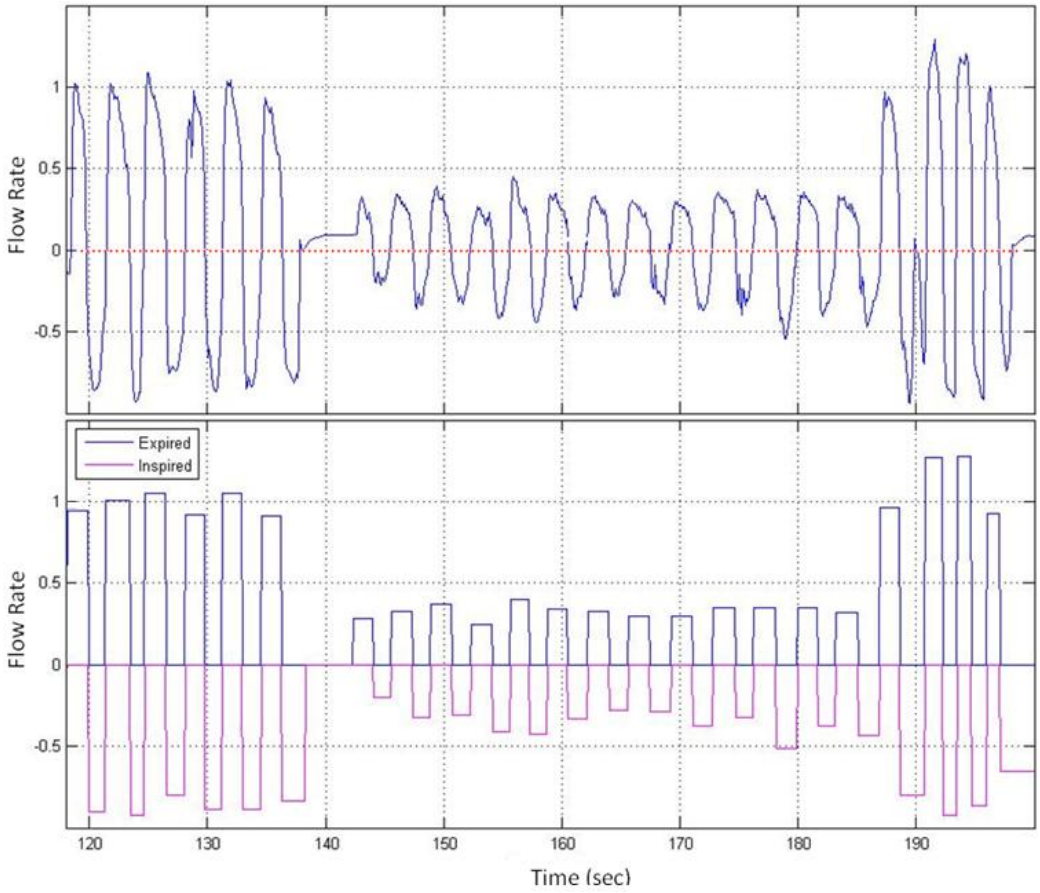

Figure 6.13: Output from fan-flow meter and flow-correction algorithm. ***Top).*** Flow rate in L/min as measured from the flow rate meter at the mayo clinic. Positive flow rate represents expired respiration. ***Bottom).*** Output from the flow-correction algorithm. A single flow rate value is assigned to each portion of the breath cycle.

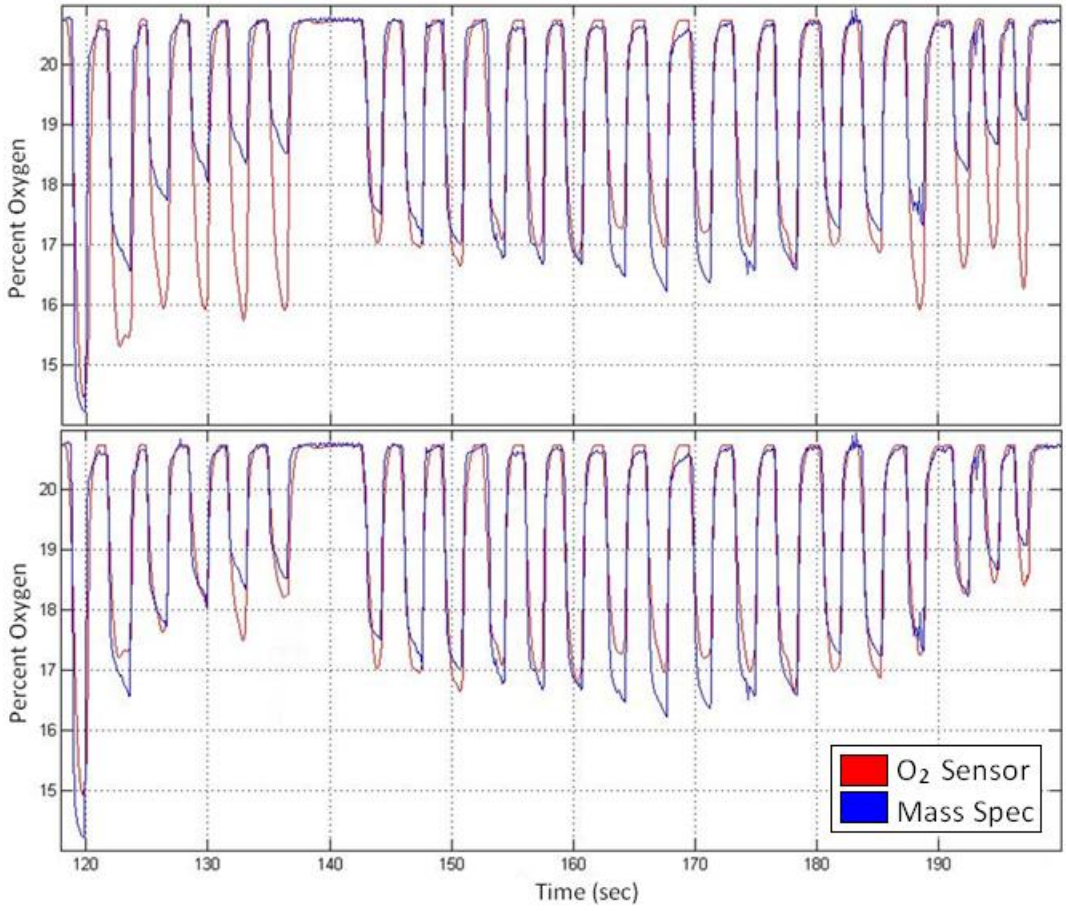

Figure 6.14: Test result with mass spectrometer and flow-correction. ***Top).*** Oxygen sensor response versus mass spectrometer without flow rate correction. ***Bottom).*** Oxygen sensor response versus mass spectrometer after flow rate correction for the same data set. Refer to Figure 6.13 to see corresponding flow rates.

6.5 Conclusions

The sensor was redesigned to be fully untethered. This included battery power and wireless data transmission. The pneumatic sampling system was removed and the casing was replaced with an open-channel design.

The new sensor was tested at the Mayo Clinic in Rochester, MN, with a mass spectrometer providing a measure of the true oxygen concentration. The signal processing techniques discussed in Chapter 5 were implemented, resulting in an RMS error ±0.2 $\%O_2$ and a maximum error of ±1 $\%O_2$ during steady respiration (constant volume).

A fan flow sensor was developed to account for sensing errors associated with heavy flow rates. With the fan flow sensor in place, the sensor was shown to be accurate to an RMS error of ±0.35 $\%O_2$ (±1.2 $\%O_2$ maximum error), for erratic breathing patterns, including varying flow rates. The fan flow meter also enables the oxygen sensor to measure volume of flow which is useful for many clinical diagnostic applications.

CHAPTER 7 CONCLUSIONS

7.1 Conclusions

An extensive literature survey and consultation with leading medical researchers revealed a significant need for portable respiratory gas sensors capable of measuring CO_2 and O_2 concentrations. Specifically, there is a demand for a small, untethered sensor that can be attached to the patient and used for ambulatory clinical applications. The untethered, wireless sensor discussed in this research paper would allow for a continual ambulatory measure of respired oxygen gas.

Three different configurations of membrane electrode assemblies were developed for oxygen gas sensing using both sputtered platinum electrodes and platinum electrode composites mixed with CNTs and Nafion solution. Control and measurement circuits were developed to detect changes in the rate of the redox reaction caused by varying oxygen gas concentration.

The responses of each of sensors to varying oxygen concentration were compared. The addition of CNTs to the membrane electrode assembly proved to be a difficult and time consuming procedure. Furthermore, CNT-based electrodes showed no improvement over pure platinum electrodes.

Overall, the 2-electrode sensor had the most consistent and repeatable results. In addition, the simplicity of fabricating, controlling, and measuring the 2-electrode sensor made it the preferred design choice for the project. Membrane electrode assemblies were fabricated in the Nanofabrication Center at the University of Minnesota. These sensors responded to oxygen but did not perform well enough to be used for breath-by-breath respiratory analysis.

The fabrication of the membrane electrode assemblies was outsourced to the Fuel Cell industry. This resulted in both cost savings and an improved and more consistent product. First generation casing was designed to facilitate respiratory gas exchange analysis by incorporating a unique pneumatic sampling system.

The response of the PEMFC-based sensor to changes in oxygen concentration was observed and the effect of humidity was studied. High, low, and widely fluctuating relative humidities resulted in a slow frequency drift in the sensor signal. In contrast, there was no drift under consistent and moderate humidity conditions.

The response of the 1st generation PEMFC-based sensor to expired breath was compared to test data taken with a MedGraphics Cardiopulmonary Exercise System. The response did not deteriorate over multiple tests as was seen with the sputtered MEAs. The magnitude of oxygen response was on the order of 10-20mV per percent change in oxygen concentration. The 95% response time of the sensor was approximately 1-3 seconds. It was shown that signal processing techniques were required to measure respired oxygen concentration with sufficient accuracy for medical research.

The sensor was redesigned to be fully untethered. This 2nd-generation design included switching to battery power and wireless data transmission. The pneumatic sampling system was removed and the sensor casing was replaced with an open-channel design.

The new sensor was tested at the Mayo Clinic in Rochester, MN, with a mass spectrometer providing a measure of the true oxygen concentration. With the addition of several post processing techniques, the 2nd-generation Nafion oxygen sensor performed very well. Post processing techniques included algorithms for breath-detection, slope-correction, baseline-correction, model inversion and calibration. The low frequency drift was removed and oxygen concentration was measured with an RMS error of ±0.2 $\%O_2$ (maximum error ±1 $\%O_2$) over steady, resting-rate respiration. During faster respiration (such as exercise) or largely-varying respiration, the accuracy of the sensor deteriorated to an RMS error of approximately ±1 $\%O_2$ (maximum error ±4 $\%O_2$).

A fan flow sensor was developed to account for sensing errors associated with heavy and widely-varying flow rates. A flow-correction algorithm was added to the other signal processing techniques to achieve more consistently accurate results. With the fan flow sensor in place, the sensor was shown to be accurate to within an RMS value of ±0.35 $\%O_2$ (max error 1.2 $\%O_2$) for erratic breathing patterns, including widely-varying flow

rates. The fan flow meter also enables the oxygen sensor to measure volume of flow which is useful for many clinical diagnostic applications.

7.2 Future Work

The sensor was tested on three separate visits to the Mayo clinic in Rochester, MN. The result was approximately 3 hours of data with the mass spectrometer. Additional testing of the sensor and fine-tuning of the calibration must be completed before it can be used in a medical setting. Future work on the sensor could also include:

1. Further testing and calibration of the fan flow meter.
2. Integration of the pulse counter and power supply (for the fan) into the existing measurement circuit.
3. Include a screen in the mouthpiece to wick moisture from the user.
4. Improve the sensor durability. The sensor is currently fabricated almost entirely with electrical tape.
5. Improve the electrical connections to electrodes. Connections are currently made using copper tape.
6. Reprogram the wireless components for lower power consumption.
7. Redesign the PCB for smaller electronics component size.
8. Decrease the overall size.
9. Improve the flow pattern to increase the flow of breath over the sensing membrane (I.e. airfoil, etc.).

References

[1] R.L. Johnson, Jr. Gas exchange efficiency in congestive heart failure ii. *Circulation*, 103, 2001.

[2] P. Ponikowski, D.P. Francis, M.F. Piepoli, and et. al. Enhanced ventilatory response to exercise in patients with chronic heart failure and preserved exercise tolerance: marker of abnormal cardiorespiratory reflex control and predictor of poor prognosis. *Circulation*, 103, 2001.

[3] P. Agostoni, R. Pellegrino, C. Conca, J.R. Rodarte, and V. Brusasco. Exercise hyperpnea in chronic heart failure: Relationships to lung stiffness and expiratory flow limitation. *J Appl Physiol*, 92:1409-1416, 2002.

[4] J.A. Franciosa, C.L. Leddy, M. Wilen, and D.E. Schwartz. Relation between hemodynamic and ventilatory responses in determining exercise capacity in severe congestive heart failure. *Am J Cardiol*, 53:127-134, 1984.

[5] American Society of Anesthesiologists. *ASA Guidelines for Patient Care in Anesthesiology*, 2006.

[6] J.G. Jones, D.J. Sapsford, and R.G. Wheatley. Postoperative hypoxaemia: mechanisms and time course. *Anaesthesia*, 45:566-573, 1990.

[7] D.M. Coventry. Anaesthesia for laparoscopic surgery. *J R Coll Surg Edinb*, 40:151-160, 1995.

[8] M.S. Takrouri. Anesthesia for laparoscopic general surgery: A special review. *Middle East J Anesthesiology*, 15:39-62, 1999.

[9] K. Zwerneman. End-tidal carbon dioxide monitoring: A vital sign worth watching. *Crit Care Nurs Clin North Am,* 18:217-225, 2006. xi.

[10] C. Larsson, L. Davidsson, P. Lundin, G. Gustafsson, and M. Vegfors. Respiratory monitoring during MR imaging: The clinical value of a new fibre-optical monitor. *Acta Radiologica*, 40:33-36, 1999.

[11] B.D. Johnson, B. Whipp, R.J. Zeballos, I.M. Weisman, K.C. Beck, D. Mahler, J. Cotes, K. Sietsema, and K. Killian. Conceptual and physiological basis of cardiopulmonary exercise testing measurement. *Am. J. Respir. Crit. Care Med.*, 167, 2003.

[12] M.M. Hoeper, R. Maier, J. Tongers, J. Niedermeyer, J.M. Hohlfeld, M. Hamm, and H. Fabel. Determination of cardiac output by the Fick method, thermodilution, and acetylene rebreathing in pulmonary hypertension. *Am. J. Respir. Crit. Care Med.*, 160(2):535-541, 1999.

[13] M. Folke, L. Cernerud, M. Ekstrom, and B Hok. Critical review of non-invasive respiratory monitoring in medical care. *Medical and Biological Engineering and Computing*, 41, 2003.

[14] Oridion Inc. Standards mandating capnography monitoring, 2007. Retrieved 2011-04-10.
Available online at
www.smartcapnography.net/assets/standards_and_capnography.pdf.

[15] A.L.Jr. Chesson, R.B. Berry, and Pack. A. Practice parameters for the use of portable monitoring devices in the investigation of suspected obstructive sleep apnea in adults. *Sleep*, 26(7):907-913, 2003.

[16] M.I. Levene, D.I. Tudehope, and M.J. Thearle. *Essentials of Neonatal Medicine: Respiratory Physiology, Respiratory Failure and Mechanical Ventilation*. Blackwell Science Ltd., Oxford, 2000.

[17] W. Cao and Y. Duan. Breath analysis: Potential for clinical diagnosis and exposure assessment. *Clinical Chemistry*, 52, 2006.

[18] P. Gauthama and E.A. Morris. Checking the capnograph before anaesthesia: a survey of national practice in the UK. *Eur. J. Anaesthesiol.*, 23(2):160-164, 2006.

[19] K. Laarmann. The future of mass spectrometry in laboratory medicine. *European Hospital*, 12/29/2010.

[20] J.B. Riker and B. Haberman. Expired gas monitoring by mass spectrometry in a respiratory intensive care unit. *Crit. Care Med.,* 4(5):223-229, 1796.

[21] P. Burdett-Smith. A patient who changed my practice: always check the respiratory rate. *Br. Med. J.*, 314:1549, 1997.

[22] P.B. Lovett, J.M. Buchwald, K. Stürmann and P. Bijur. The vexatious vital: neither clinical measurements by nurses nor an electronic monitor provides accurate measurements of respiratory rate in triage. *Annals of Emergency Medicine*, 45(1):68-76, 2005.

[23] J. Butler, S. Hanumanthu, D. Chomsky and J.R. Wilson. Frequency of low-risk hospital admissions for heart failure. *Am. J. Cardiol.*, 81(1):41-44, 1998.

[24] J.B. O'Connell and M.R. Bristow. Economic impact of heart failure in the United States: time for a different approach. *J. Heart Lung Transplant*. 13(4):107-112, 1994.

[25] D. Dodds, J. Purdy and C. Moulton. The PEP transducer: a new way of measuring respiratory rate in the non-intubated patient. *J. Accid. Emerg. Med.* 16(1):26-28, 1999.

[26] D. Sankar and K.J. Kini. Respiratory monitoring of non-intubated patients using the 'PIPPA' breathing monitor. British Journal of Anaesthesia, 89:677, 2002.

[27] L.C. Clark, R. Wolf, D. Granger and Z. Taylor. Continuous recording of blood oxygen tensions by polarography. *J. Appl. Physiol.*, 6:189-193, 1953.

[28] L.C. Clark. Electrochemical device for chemical analysis. *US Patent 2,913,386*, 1959.

[29] J.W. Severinghaus. The invention and development of blood gas analysis apparatus. *Anesthesiology*, 97(1):253-256, 2002.

[30] Alpha Omega Instruments. Oxygen Sensor Types. *Additional product information*, retrieved 2010-09-22.
Available online at http://www.aoi-corp.com/additional_information/oxygen_sensor_types.

[31] S. Sotiropoulos and K. Wallgren. Solid-state microelectrode oxygen sensors. *Analytica Chimica Acta*, 388:51-62, 1999.

[32] J.A. Von Fraunhofer and C.H. Banks. *Potentiostat And Its Applications*. London, Butterworths, 1972.

[33] M. Acosta. Designing with electo-chemical sensors. *Analog Edge: The Online Technical Publication*, 2008.

[34] J.C. Fidler, W.R. Penrose, and J.P. Bobis. A potentiostat based on a voltage-controlled current source for use with amperometric gas sensors. *IEEE Transaction on Instrumentation and Measurement*, 41(2):308-310, 1992.

[35] C. Damian, C. Zet, I. Enculescu and R. Spohr. Virtual potentiostat. Proceedings of 15th IMEKo TC4 Symposium on Novelties in Electrical Measurements and Instrumentation, 1:596-600, 2007.

[36] H. Yan and J. Lu. Solid polymer electrolyte-based electrochemical oxygen sensor, *Sensors and Actuators*, 19:33-40, 1989.

[37] H. Yan and C. Liu. Humidity effects on the stability of a solid polymer electrolyte oxygen sensor. *Sensors and Actuators B*, 10:133-136, 1993.

[38] H. Yan and J. Lu. A solid polymer electrolyte-based oxygen sensor for portable oxygen meters. *Field Analytical Chemistry and Technology*, 1997.

[39] J. Gopalakrishna, W. Wlodarski, and P. Iles. Performance of solid polymer electrolyte based oxygen sensor without external humidification. *IEEE Xplore*, 1999.

[40] Clean Fuel Cell Energy. About fuel cell membrane electrode assemblies. *Clean Fuel Cell Energy fuel cell booklet,* retrieved 2010-01-05. Available online at www.cleanfuelcellenergy.com.

[41] Clean Fuel Cell Energy. A brief synopsis of fuel cells. *Clean Fuel Cell Energy fuel cell booklet,* retrieved 2010-01-05. Available online at www.cleanfuelcellenergy.com.

[42] J.S. Lee, N.D. Quan, J.M. Hwang, S.D. Lee, H. Kim, H. Lee and H.S. Kim. Polymer electrolyte membranes for fuel cells. *J. Ind. Eng. Chem.*, 12(2):175-183, 2006.

[43] J. Larminie and A. Dicks. *Fuel Cell Systems Explained (Second Edition)*. John Wiley & Sons, 2003. Available online at http://www.knovel.com/web/portal/browse/display?_EXT_KNOVEL_DISPLAY_bookid=1109&VerticalID=0

[44] Ballard Power Systems. Commercially viable fuel cell stack technology ready by 2010. *FuelCellWorks.com*, 2005.

[45] W. Li, C. Liang, J. Qiu, W. Zhou, H. Han, Z. Wei, G. Sun and Q. Xin. Carbon nanotubes as support for cathode catalyst of a direct methanol fuel cell. *Letters to the Editor / Carbon*, 40: 787-803, 2002.

[46] C. Wang, M. Waje, X. Wang, J.M. Tang, R.C. Haddon and Y. Yan. Proton exchange membrane fuel cells with carbon nanotube based electrodes. Nano Letters, 4(2): 345-348, 2004.

[47] Y.H. Liu, B. Yi, Z. Shao, L. Wang, D. Xing and H. Zhang. Pt/CNTs-Nafion reinforced and self-humidifying composite membrane for PEMFC applications. *J.of Power Sources*, 163: 807-381, 2007.

[48] A. VanBruinessen. *Development of pt/cnt catalyst and transport-kinetic characterization of pemfc catalyst layer* (Master's Thesis). Retrieved June 2009 from http://www.collectionscanada.gc.ca/obj/thesescanada/vol2/OKQ/TC-OKQ-1664.pdf

[49] S. Wang, D. Yu and L. Dai. Polyelectrolyte functionalized carbon nanotubes as efficient metal-free electrocatalysts for oxygen reduction. *J. of Amer. Chem. Soc.*, 133(14):5182-5185, 2011.

[50] R. O'Hayre, D.M. Barnett, and F.B. Prinz. The pt/nafion/air triple phase boundary: Model, experiment, and implications for PEM fuel cells. *The Electrochem. Soc. Digital Lib.*, 2004.
Available online at http://www.electrochem.org/dl/ma/206/pdfs/1849.pdf.

[51] R. O'Hayre, D.M. Barnett and F.B. Prinz. The triple phase boundary: a mathematical model and experimental investigations for fuel cells. *J. Electrochem. Soc.*, 152:A439-A444, 2005.

[52] C. Heitner-Wirguin. Recent advances in perfluorinated ionomer membranes: structure, properties and applications. *J. Membrane Sci.*, 120(1):1-33, 1996.

[53] Perma Pure LLC. Nafion - the perfect drying and humidifying material. *Technical notes and articles*, retrieved 05-05-2011. Available online at http://www.permapure.com/industry/fuelcell/technology/?ind=fuelcell.

[54] T. Smith. Boffin's breakthrough boosts fuel cell output by 50%. *Hardware Magazine*, 05/20/2008.

[55] A. Dyck, D. Fritsch and S.P. Nunes. Proton-conductive membranes of sulfonated polyphenylsulfone. *J. for Appl. Polymer Sci.*, 86(11):2820-2827, 2002.

[56] K.A. Mauritz and R.B. Moore. State of understanding Nafion. *Chem. Rev*., 104:4535-4585, 2004.

[57] Y. Takamura, E. Nakashima, H. Yamada, A. Tasaka and M. Inaba. Effects of temperature and relative humidity on oxygen permeation in Nafion and sulfonated poly(arylene ether sulfone). ECS Trans, 16(2):881-889, 2008.

[58] T. Fabian, R. O'Hayre, S. Litster, F.B. Prinz and J.G. Santiago. Active water management at the cathode of a planar air-breathing polymer electrolyte membrane fuel cell using an electroosmotic pump. *J. of Power Sources*, 195(11):3640-3644, 2010.

[59] S. Sheppard, S.A. Campbell, J.R. Smith, G.W. Lloyd, T.R. Ralph and F.C. Walsh. Electrochemical and microscopic characterization of platinum-coated perfluorosulfonic acid (Nafion 117) materials. *Analyst*, 123: 1923-1929, 1998.

[60] Y. Gao, H. Kita, Y. Watanabe, and K. Sima. An electrochemical Nafion matrix oxygen sensor and the evaluation of oxygen permeation in coated films. *Journal of Applied Chemistry*, 23:1102-1106, 1993.

[61] R. O'Hayre, S. Lee, S. Cha and F. Prinz. A sharp peak in the performance of sputtered platinum fuel cells at ultra-low platinum loading. *J. of Power Source*. 109: 483-493, 2002.

[62] Fuel Cells 2000. The online fuel cell information resource. Information Resources – Developers, retrieved 06-10-2011. Available online at http://www.fuelcells.org/info/fcdev.html.

[63] Shyam Sivaramakrishnan, "Carbon Nanotube Based Carbon Dioxide Gas Sensors for Respiratory Monitoring," PhD thesis, Department of Mechanical Engineering, University of Minnesota, 2009.

Appendix

Additional results, collected at St. Mary's Hospital, Feb 10th, 2011.

Data Set 1

Comparison of O_2 concentration measurement from new Nafion sensor and mass spectrometer.

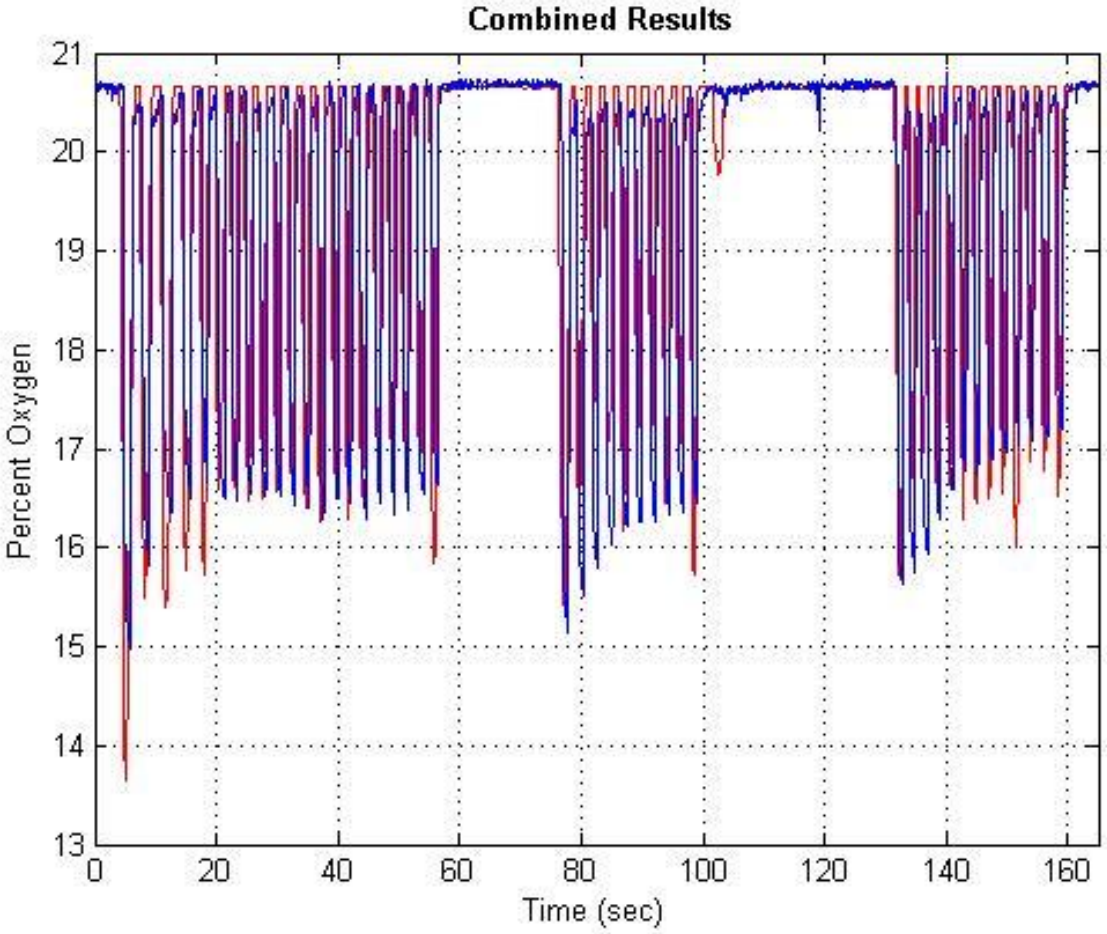

Data Set 1 Continued

Raw data from Nafion sensor before signal processing. Breath detection algorithm from raw data is plotted below. This is the first step in signal post processing.

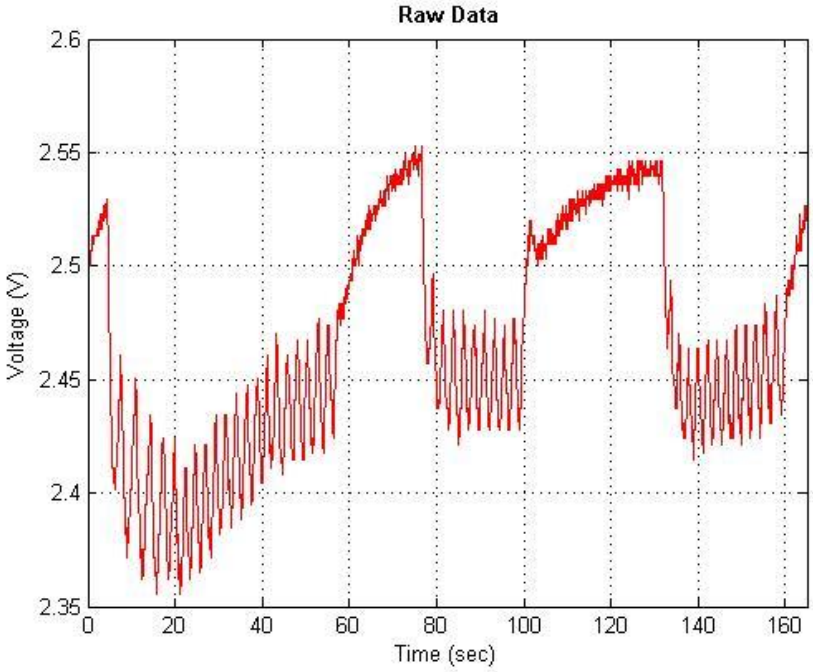

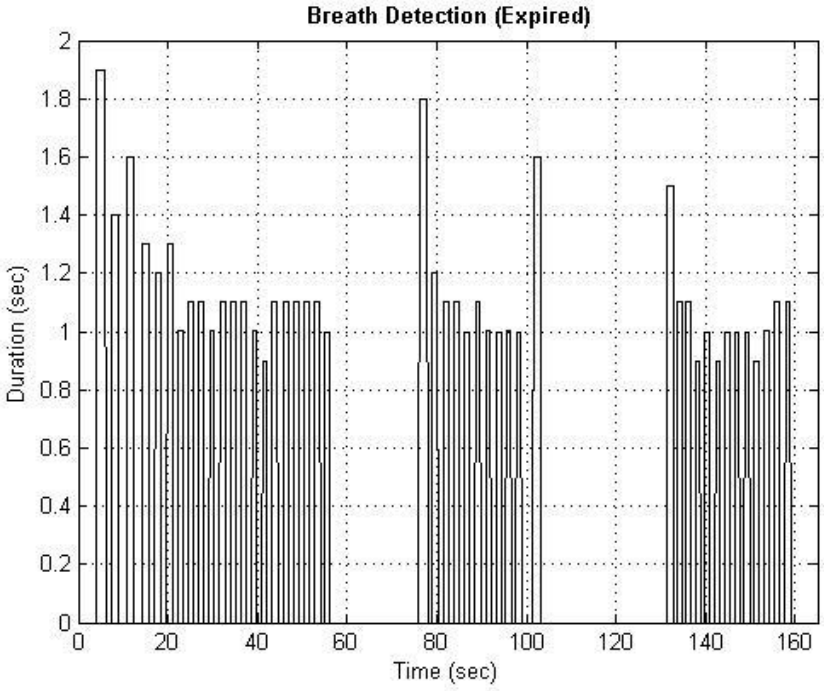

Data Set 1 Continued

Approximation of inspired flow rate over each inspired breath from fan flow sensor. Scaling is relative.

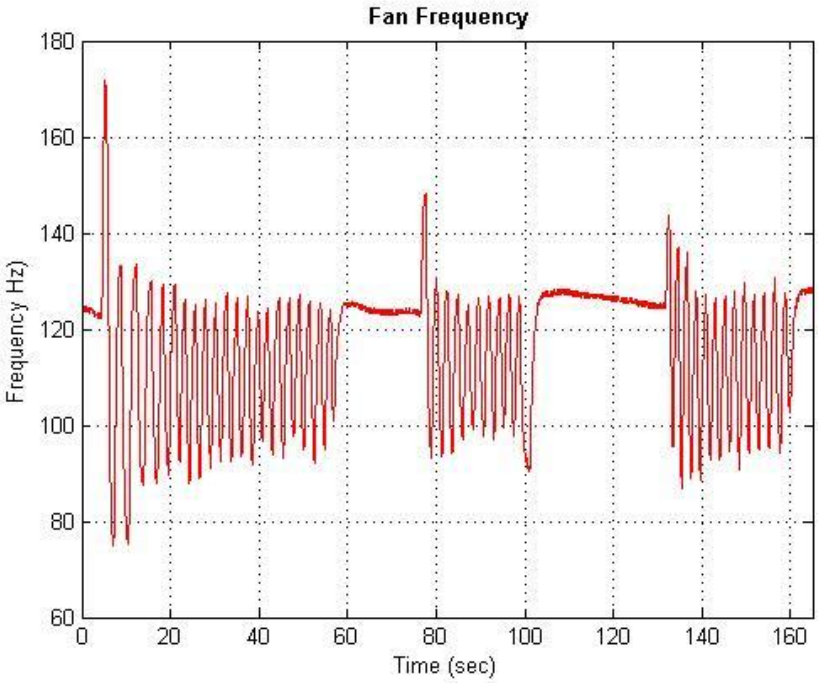

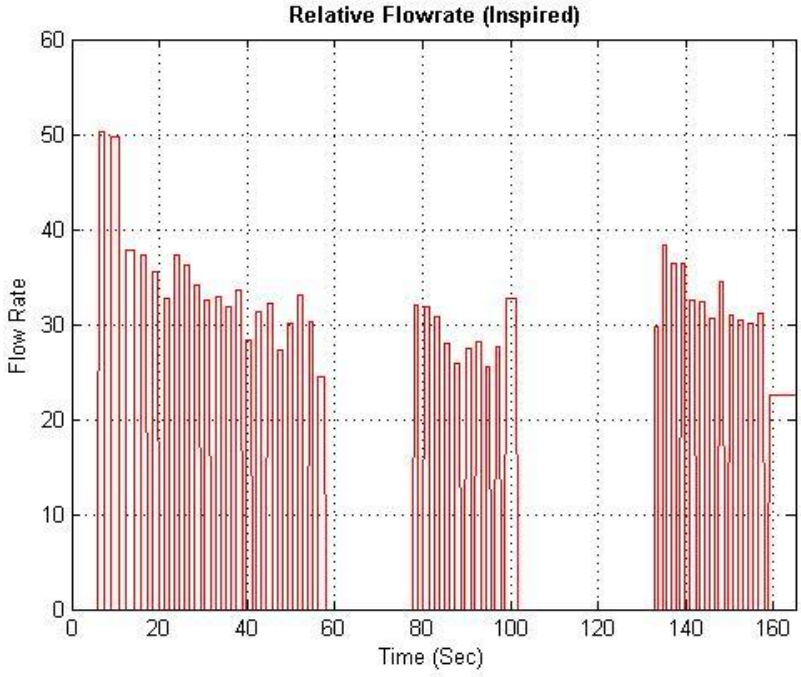

Data Set 2

Another sample data set showing good correlation with mass spectrometer during steady breathing and steady flow rate.

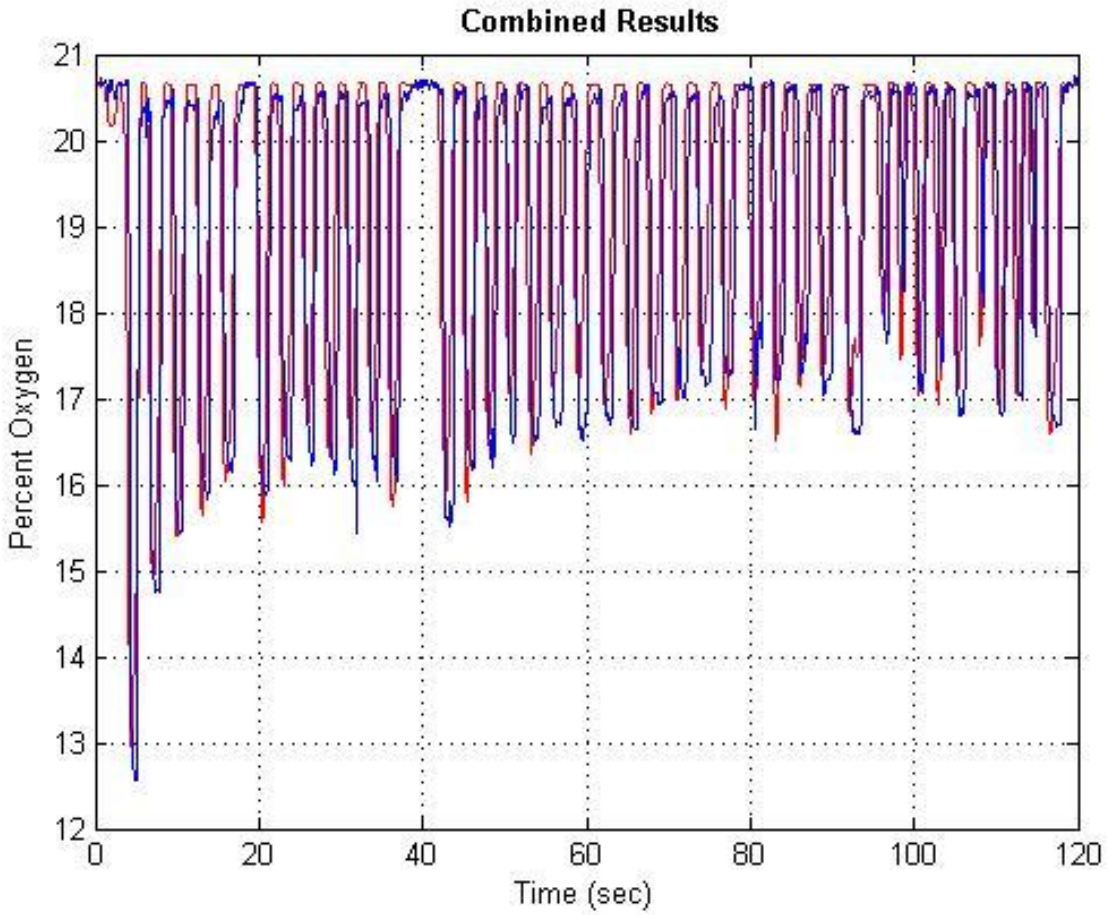

Data Set 3

Flow rate dependence of O_2 sensor occurs when variation in flow rate is large.

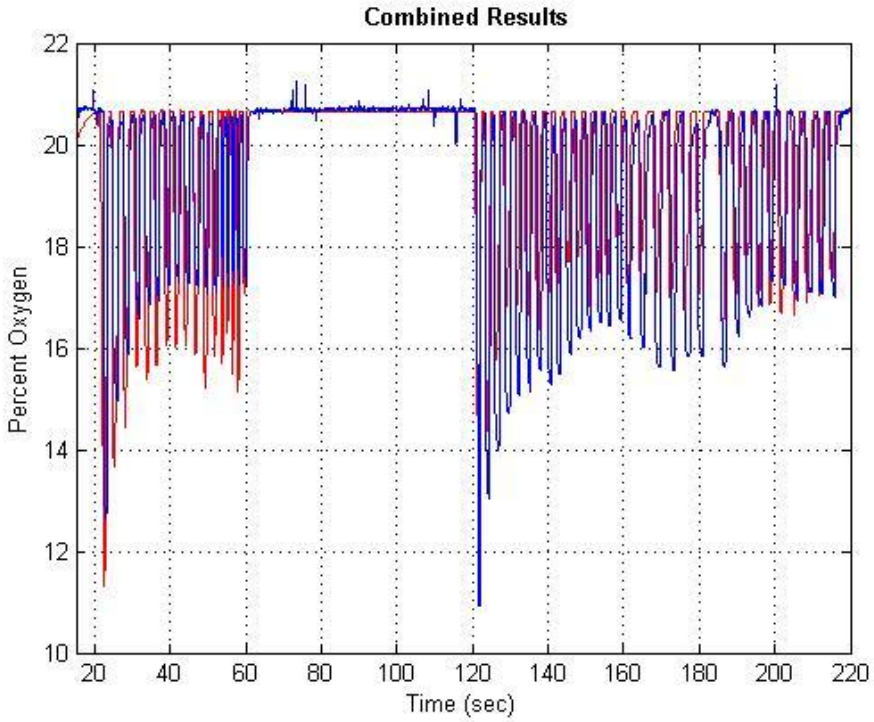

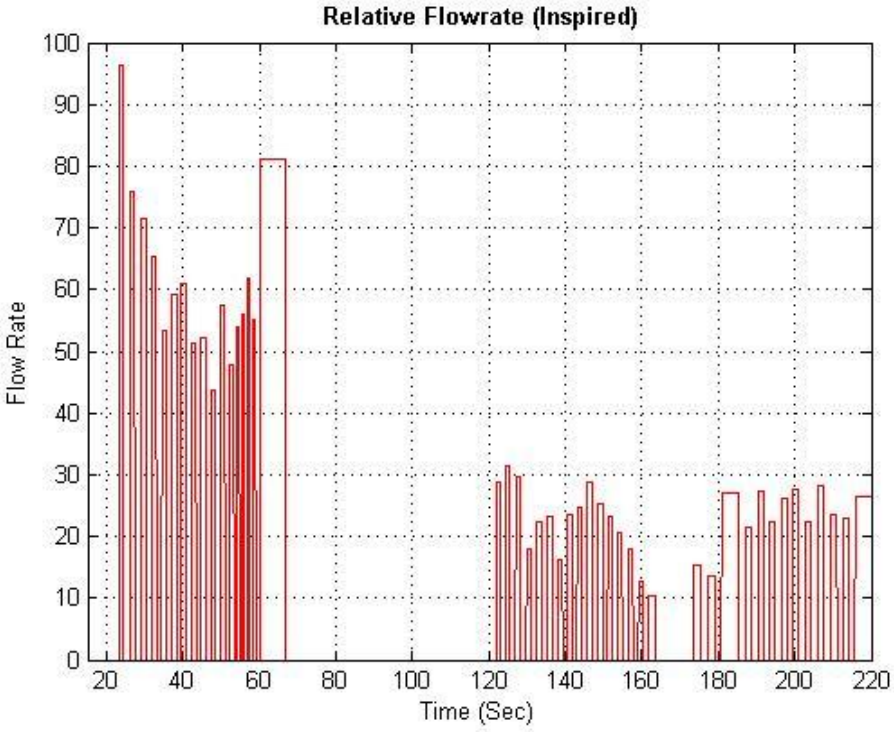

Data Set 4

Another example of flow rate dependence under highly varying breath levels.

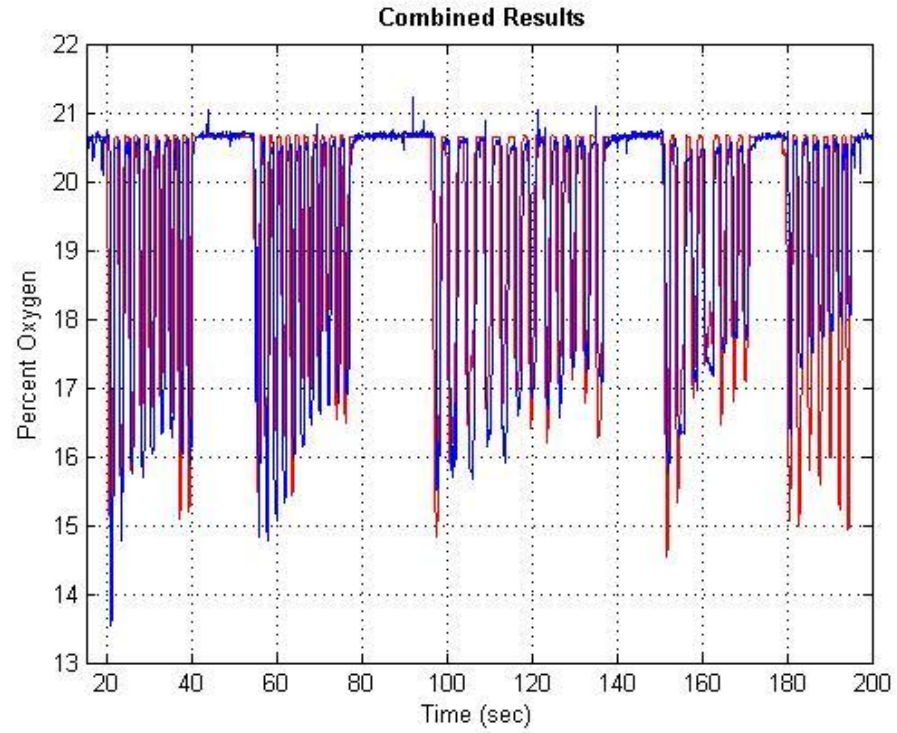

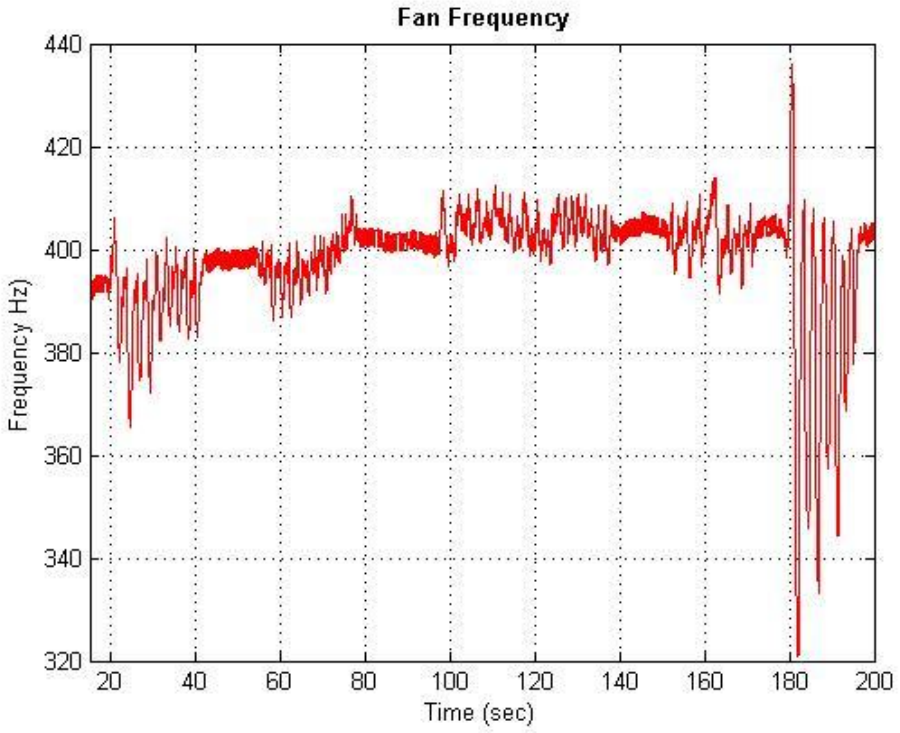

Data Set 5 – Without flow rate adjustment

Results before & after flow rate correction**.**

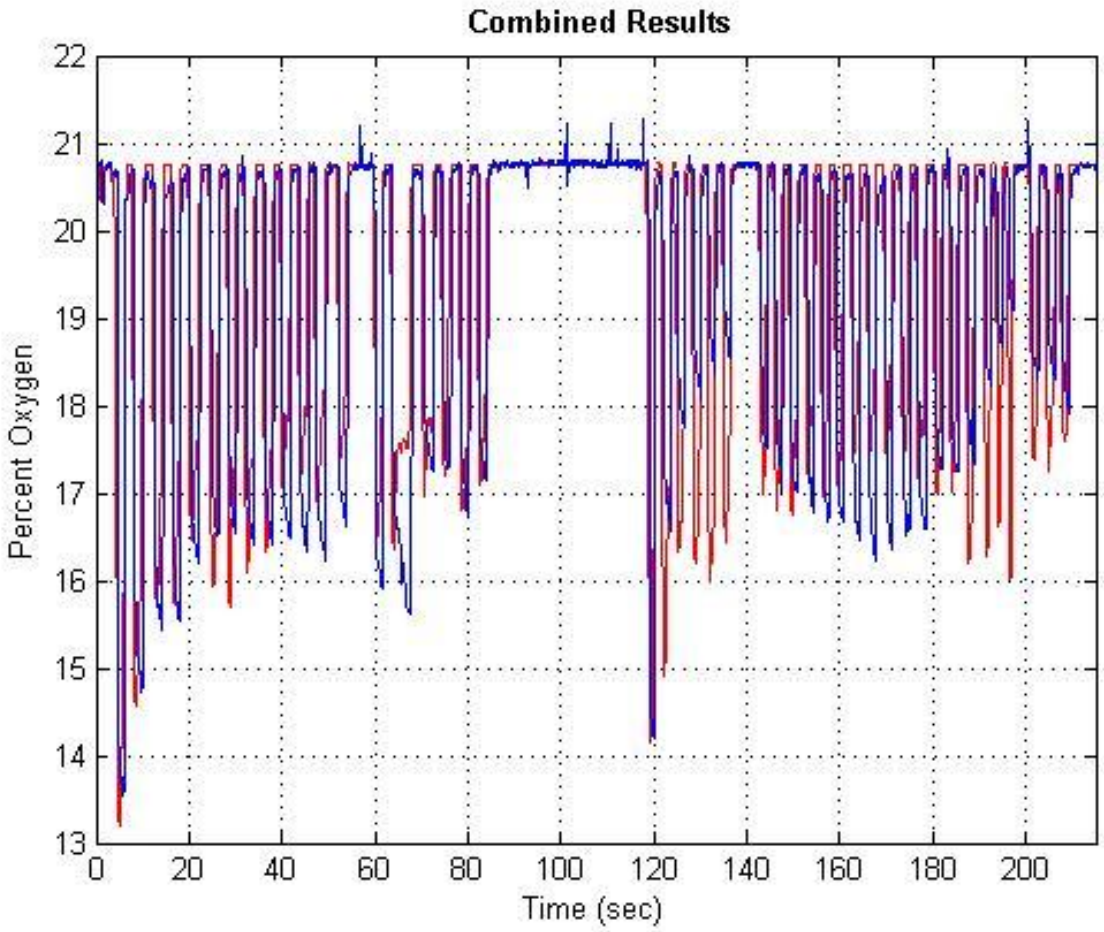

Data Set 5 – With flow rate adjustment

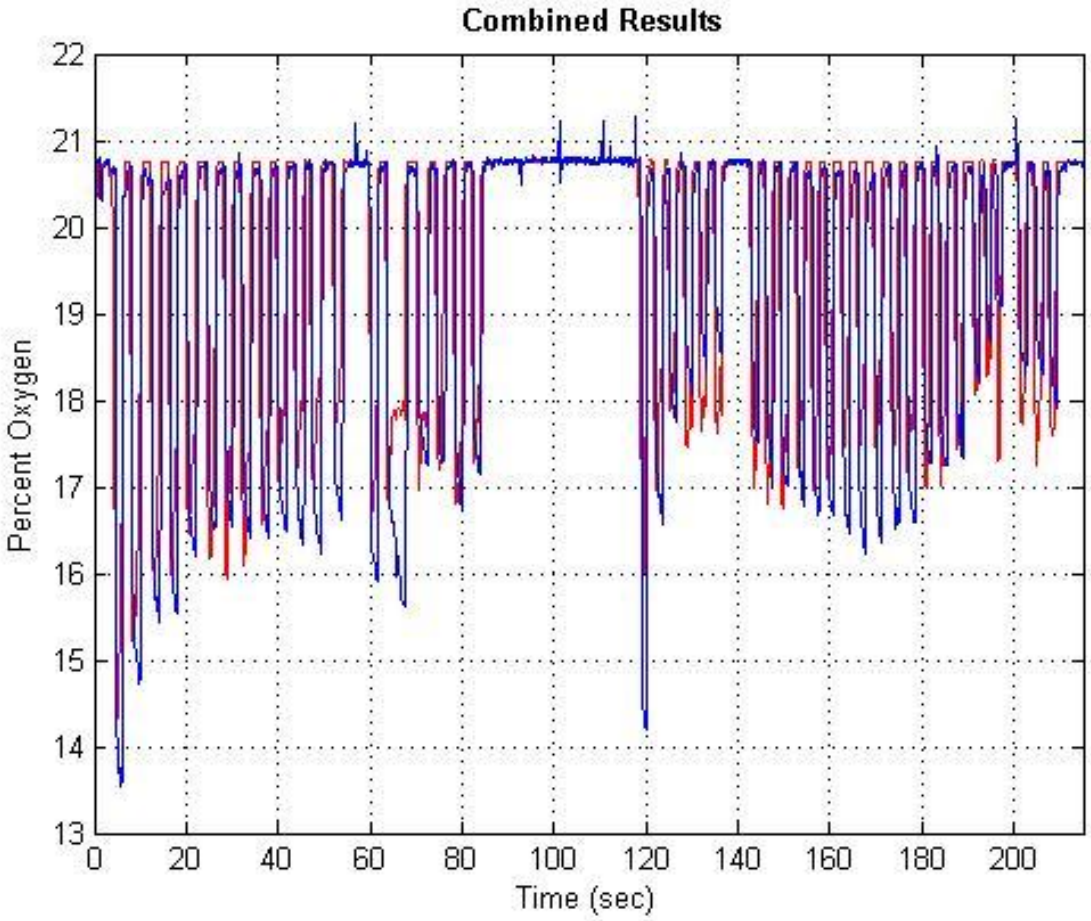

Data Set 5 Continued – Flow Rate Sensors

Comparison of our fan flow rate sensor versus the sensor accompanying the mass spectrometer**.**

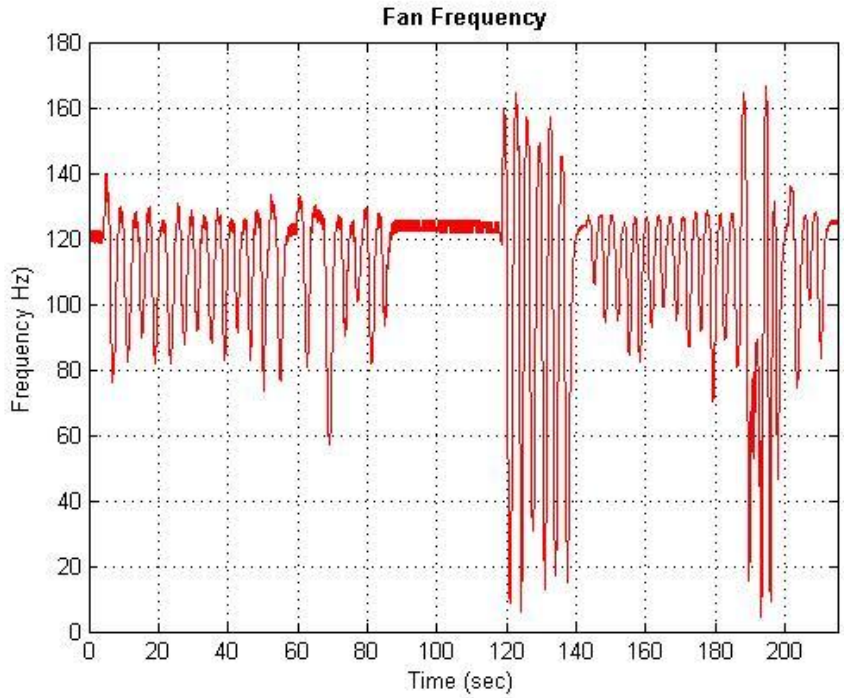

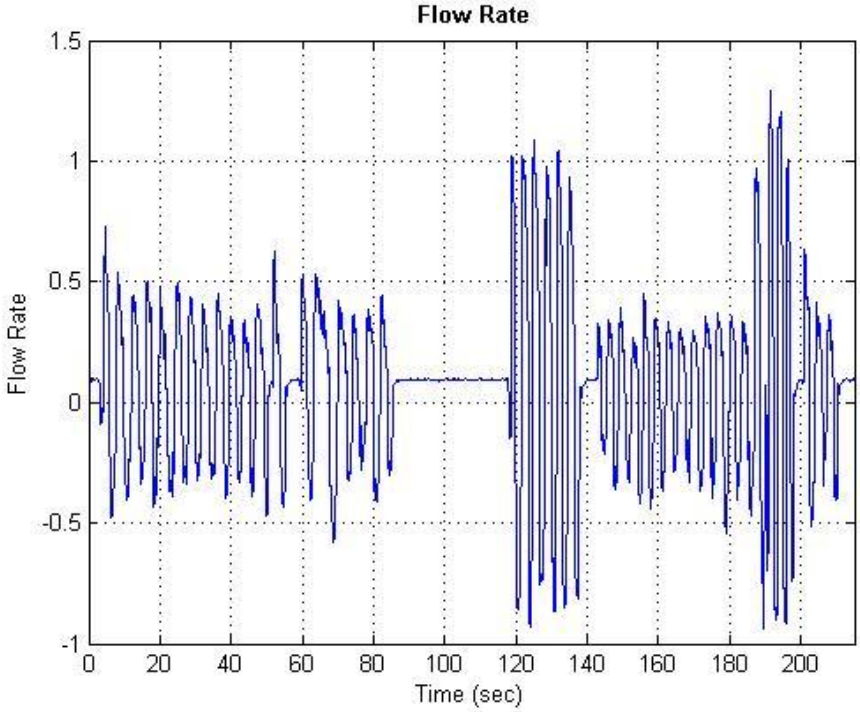

Data Set 5 Continued

Approximation of flow rate over each breath (Expired/Inspired).

The approximated expired flow rate is used to demonstrate flow correction in data sets 17 & 20.

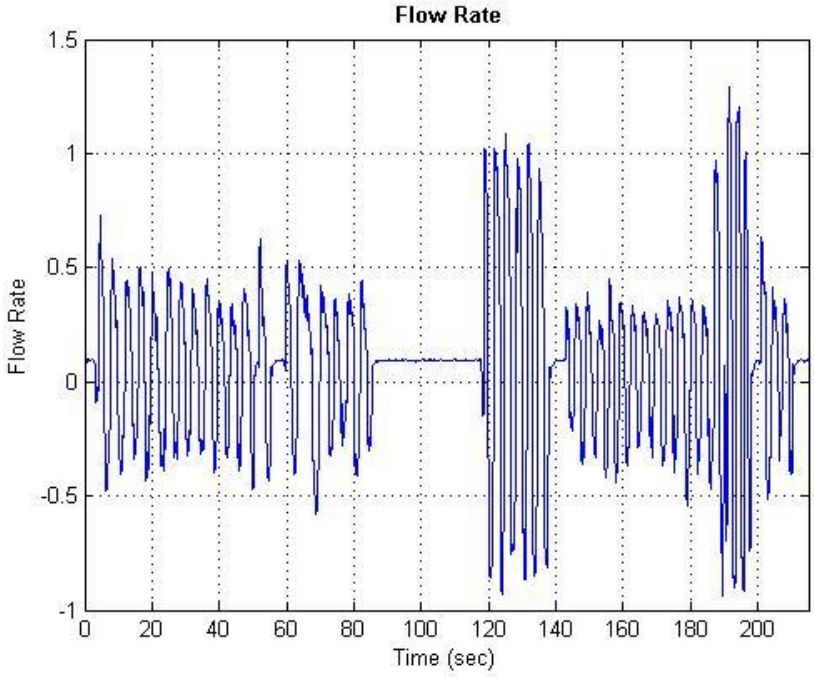

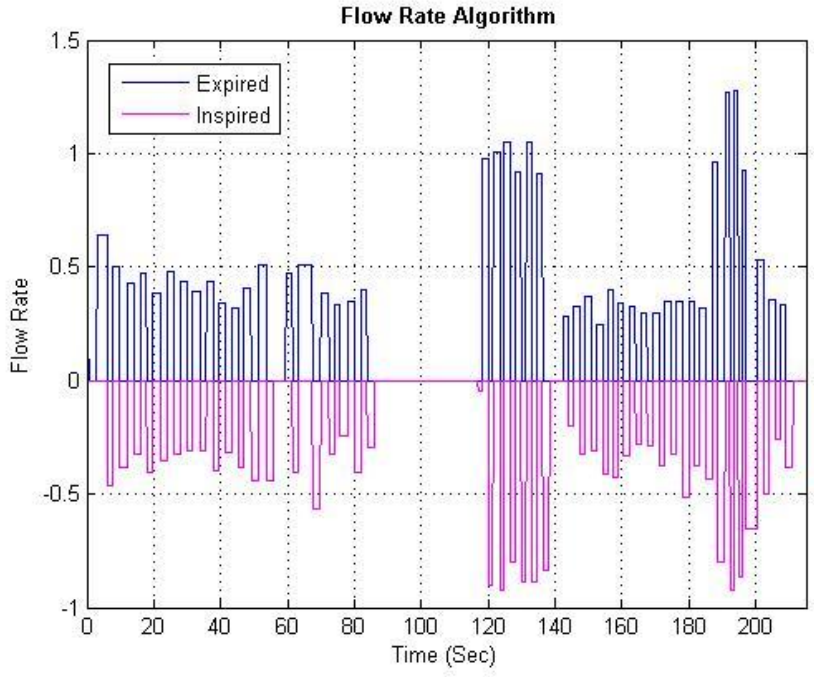

Data Set 6 – Without flow rate adjustment

Another example of sensor data before and after flow rate correction.

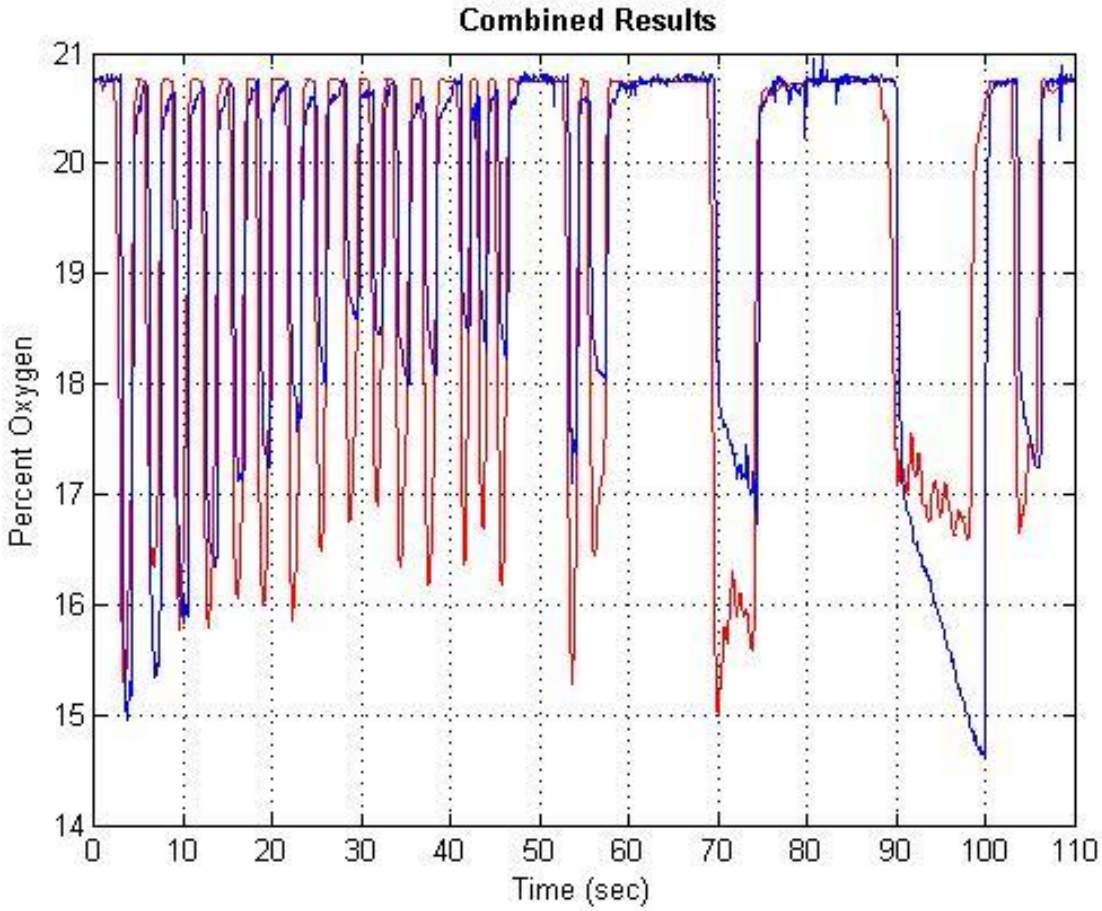

Data Set 6 – With flow rate adjustment